Fiber Tracking and Tractography with Magnetic Resonance Diffusion Tensor Imaging for Quantitative Evaluation of Schizophrenia

Utako Yamamoto

Graduate School of Engineering, Kyoto University

Acknowledgments

First of all, it is a great pleasure to express my gratitude to my supervisor Professor Tetsuo Kobayashi for his encouragement, guidance and support.

I acknowledge greatly the guidance and encouragement by Professor Shinji Doi and Professor Hiroshi Yamakawa. I sincerely thank Professor Yoshihiko Koga and Dr. Shinsuke Kito for providing the imaging data and their kindly supports. It is a pleasure to thank Professor Susumu Mori, Dr. Shoko Yoshida, and all members in Johns Hopkins University for the guidance, fruitful discussions, and kindness when I visited their group in USA. I acknowledge the useful comments and supports by Associate Professor Shoji Hamada, Dr. Takenori Oida, Dr. Yosuke Ito, and Dr. Shiho Okuhata. I also acknowledge the technical, spiritual supports, and friendly atmosphere by all members of the Kobayashi group, in particular Ms. Shizue Nagahara and Mr. Akifumi Hisada.

This work was financially supported by a Grant-in-Aid for Japan Society for the Promotion of Science (JSPS) Fellows (23-5832).

Finally I greatly thank my family for their spiritual support, encouragement, and warm atmosphere.

Abstract

Higher brain functions of a human are realized by comprehensive activities of multiple tissues in the brain. In the brain tissues, nerve fibers forming nerve tracts transmit information between regions of the cerebral cortex. When nerve fibers have some abnormalities, information is not conveyed successfully in the brain, and the higher brain functions do not work accordingly. In particular the schizophrenia, a representative psychiatric disorder as a higher brain dysfunction, is involved in the abnormalities in nerve fibers. It is important to evaluate the degree of the abnormalities in nerve fibers for diagnosis of the disease. This dissertation is devoted to the development of several methods for measuring the values characterizing the nerve fibers efficiently by use of the magnetic resonance diffusion tensor images in order to evaluate the degree of the abnormalities quantitatively.

We study on the fiber tracking and tractography for the quantitative evaluation of schizophrenia. We characterize nerve tracts numerically by the fiber tracking technique with the magnetic resonance diffusion tensor images. The superior longitudinal, inferior longitudinal, and inferior fronto-occipital fasciculi are targeted. We demonstrate the feasibility that several indices obtained through the fiber tracking evaluate the abnormality in nerve tracts of schizophrenic patients.

In addition we propose an improved method to perform the fiber tracking. Usually the regions of interest are constructed in a manual way. In the improved method, the regions of interest can be constructed automatically by use of the segmented image based on the anatomical locations of tracts corresponding to the standard brain. We implement the fiber tracking by the improved method. We focus on the sagittal stratum and the superior longitudinal fasciculus. We show that the abnormalities of nerve tracts are characterized by more informative indices, which are available as the indicators of evaluation.

We propose a novel method for the interpolation of a trajectory during the fiber tracking in the area where multiple tracts are crossing, in order to perform the fiber tracking in the crossing area with reduction of the tracking errors. The method is examined by the simulation data sets corresponding to the actual nerve tract from the center of the corpus callosum to the fifth visual cortex. We establish a certain progress of robustness to track the targeted bundle in comparison to the previous methods.

In this dissertation we propose several methods to characterize the nerve fibers in order to evaluate the degree of the abnormalities in the nerve fibers. We demonstrate the effectiveness of our proposed methods for the evaluation of the nerve fibers. We expect that the application of the proposed methods to evaluate the abnormalities of schizophrenia supports the diagnosis and treatment in early stage of the disease.

Contents

List of Figures

List of Tables

Chapter 1

Introduction

How do human beings think over things in their daily life and their brains deal with information? The brain is roughly divided into the cerebrum, the cerebellum, and the brain stem [1]. We recognize the gray matter and the white matter in a cross section of the cerebrum. The gray matter existing around the surface of the cerebrum is called the cerebral cortex in general. It manages cerebral functions, processing information obtained from the outside and controlling physical activities and biological functions [2]. The white matter indicates the mass of the nerve fibers composed of myelinated axons. It occupies more than 40 % of the adult cerebral volume, and transmits information between multiple regions of the cerebral cortex [3]. The information obtained from the outside of the brain is transfered through the nerve fibers and processed in the multiple regions. The information processing realizes the intelligence of human beings [4].

When a region of the cerebral cortex has a disorder, a brain function treated by the region is spoiled. The information normally processed in a part of the cerebral cortex is not conveyed to the other part when a nerve fiber transmitting the information has a lesion. Even if the cerebral cortex does not have any troubles, an impairment is capable of occurring in a higher brain function by an abnormality of a nerve fiber. Since a nerve bundle formed with a multitude of nerve fibers connects manifold regions in the cerebral cortex, an abnormality of the nerve bundle affect higher brain functions widely. Therefore, it is important to detect the abnormality in the nerve bundle for the evaluation of the deficit of the higher brain function.

The white matter abnormality is advocated in the brain of the schizophrenic patients [5]. Schizophrenia is one of the psychiatric disorder, which is a higher brain dysfunction. It is the most debilitating of all adult psychiatric illnesses and has high prevalence [6]. It is desired that we evaluate conditions of the nerve fibers quantitatively and detect abnormalities caused by the disease in the nerve fibers. The quantitative evaluation of nerve fibers and the detection of abnormalities are important to diagnose and treat the disorder in the early stage. How do we measure the degree of the abnormality? Any

techniques with invasive measurement inside of the brain are very risky since the biological tissues are delicate in the central nervous system.

Several noninvasive methods for the measuring and imaging of the in vivo structures have become popular in clinical diagnosis. In particular, magnetic resonance imaging (MRI) is a representative noninvasive method to obtain images of the intravital tissues [7]. It measures the signals from protons; the nuclei of water molecules which exist in large quantities in vivo, with the magnetic resonance phenomena of nuclei. The magnetic resonance diffusion weighted imaging (MR-DWI) with the MRI technique images and measures the diffusion which occurs as a result of the micromovement of water molecules [8]. The magnetic resonance diffusion tensor imaging (MR-DTI), which plays a central role in our study, is a noninvasive method with the MR-DWI technique [9]. The technique investigates the three-dimensional diffusion of water molecules in vivo by use of at least six different images with MR-DWI [10]. The magnitude of the diffusion can be approximately described as a symmetric three-dimensional ellipsoid, namely the diffusion ellipsoid, whose shape and orientation are derived as a tensor in each voxel [11].

A nerve bundle which connects multiple cortical areas within the white matter consists of a large collection of axons [12]. Water molecules cannot pass through the walls of the axons, but they are capable to move around them. In the cerebral white matter, since the diffusion of water molecules parallel to nerve fibers in a nerve bundle is unrestricted, they exhibit fast behavior. On the other hand, since the diffusion perpendicular to nerve fibers is restricted, the behavior of molecules becomes significantly tardy [13]. Hence, it is possible to obtain structural information about the nerve fiber by quantifying the magnitude and direction of the water diffusion in the white matter with MR-DTI [14]. The orientation of the nerve fibers is estimated by the obtained diffusional information. We can reconstruct the three-dimensional image of the nerve fibers along the direction based on the diffusional information of water molecules [15, 16, 17]. The technique of reconstruction is called a fiber tracking, and the reconstructed image is called a tractography. We can measure the microstructural and structural abnormality in the nerve fibers by use of the fiber tracking and the tractography.

Studies on the detection of the abnormalities of nerve fibers with MR-DTI for analyzing the brains of patients suffering from psychiatric disorders have increased. A research on the cerebral white matter of schizophrenic patients using MR-DTI was first reported in 1998 [18]. This study reported that schizophrenic patients showed diminished anisotropy in the frontal white matter, including the internal capsule and the white matter of the temporal lobe. It was found in the next year that a volume of the cerebral white matter did not decrease but a diffusional anisotropy declined in the patients compared to the healthy subjects in the multiple white matter areas [19]. Later, a widespread reduction in anisotropy was suggested in studies with larger numbers of participants [20, 21, 22].

The evidence of the reduced anisotropy of the diffusion in specific neuronal tracts such as the uncinate fasciculus [23], arcuate fasciculus [24], and cingulate fasciculus [25] has been discovered. It was also found that there is greater progressive loss in white matter integrity for schizophrenic patients as they age [26]. It was reported that the fractional anisotropy (FA) of the inferior longitudinal fasciculus was reduced [21]. This research also found that the reduction in the right hemisphere had a negative correlation with measures of thinking disorder, with reductions in the volume and the FA value of the arcuate fasciculus found in schizophrenic patients using fiber tractography. The FA value is an index of the anisotropy strength in each voxel [11]. Its definition is given in the following chapter. The facts of reduction in the FA value and increase in the mean diffusivity (MD) of the thalamo-frontal white matter have also been discovered via fiber tractography [27]. The MD value indicates the volume of the diffusion [28]. Negative correlations of FA values and positive symptom scores in PANSS (positive and negative syndrome scale) were also found in the left uncinate and left superior longitudinal fasciculi, and the right sagittal stratum (including the inferior longitudinal and fronto-occipital fasciculi) [29]. It was also shown that the FA value in the right hemisphere of the superior longitudinal fasciculus had a reduced value in a schizophrenic patient [30]. Since FA reduction and MD increase in the corpus callosum of patients and unaffected relatives have been observed in comparison to healthy controls, schizophrenia is believed to be an endophenotype [31]. The diagnosis in the early stage of the disease leads to the effective treatment.

The objective of our present study is to measure and evaluate microstructural and structural abnormalities based on FA and MD values and shapes of certain nerve bundles in the white matter of schizophrenic patients by use of the fiber tracking and tractography techniques. The FA reduction and the negative correlations of the FA value with the disease symptoms were reported [21, 29, 30]. In our study, we then target the superior longitudinal, the inferior longitudinal, and the inferior fronto-occipital fasciculi, and the sagittal stratum. We also investigate feasible indices for the quantitative evaluation of the abnormalities in the cerebral white matter in schizophrenic patients. It is considered that the findings in our study contribute to the diagnosis of schizophrenia. In Chapter 3, the performing of the fiber tracking and the statistical analysis for schizophrenia with manual ROI (region of interest) construction are described. Subsequently, we show the analysis by automatic ROI construction during the fiber tracking in Chapter 4.

The fiber tracking using MR-DTI gives us the three-dimensional information of nerve bundles on the basis of the diffusional anisotropy in the white matter. The issue associated with the fiber tracking is limitation of the MR-DTI resolution. The order of an imaging voxel size by MR-DTI is a millimeter, which is much larger than the diameter of a nerve fiber as $0.2 \sim 20$ μm [32]. We can obtain high degree of diffusional anisotropy only in the area where less than a single nerve bundle is in a unit voxel. On the other hand,

the degree goes down in the area where multiple nerve bundles cross each other in a unit voxel [33]. This phenomenon is called the Partial Volume Effect (PVE) [34].

In the event that the diffusional anisotropy decreases partially, the fiber-tracking process may be terminated or suffer from tracking errors, even if the bundle continues to the opposite side over the low anisotropy area. In order to address this issue, several methods have been proposed [35, 36, 37, 38, 39]. None of these methods, however, has proven sufficient, and they also come with disadvantages. For instance, regional manual operations have to be performed, a two-dimensional diffusion model must be used, and it takes a long analysis time to obtain the precise results, etc.

In Chapter 5, we propose a fiber tracking method that tracks fibers in crossing areas of multiple nerve bundles, in order to improve the precision of tracking in the fibers crossing area with a low degree of diffusion anisotropy. It is established by searching the relevant streamline of fibers based on the curvature and torsion of interpolated streamline in the crossing areas. The streamline is interpolated with three-dimensional B-spline curve around the fiber crossing area. We demonstrate efficiency of this method using three-dimensional simulation models. By the proposed method, more number of fibers could be tracked continuously in the crossing area in several cases for the simulation compared with conventional methods. In addition, we can obtain more information characterizing the fibers when more fibers are tracked.

Chapter 2

Background

In this chapter, we describe preliminary explanation about imaging techniques and explain a psychiatric disorder targeted in this study. We perform the fiber tracking that is a three-dimensional reconstruction of white matter tracts in the human brain using diffusion tensor imaging (DTI), which describes three-dimensional diffusion anisotropy of water molecules in vivo using multiple diffusion weighted images (DWI). The image by DWI has signal contrast derived from the magnitude of water molecule diffusion with magnetic resonance imaging (MRI) technique. We focus on one of the most representative psychiatric disorder, namely schizophrenia. We provide the principles of MRI, DWI, DTI, and the fiber tracking, and the symptoms of schizophrenia.

2.1 Magnetic resonance imaging (MRI)

The technique of MRI is based on a chemical analytical technique called nuclear magnetic resonance (NMR). This section describes the principle of NMR phenomenon and MRI [40, 41].

2.1.1 Nuclear magnetic resonance (NMR) phenomenon

The tissues in vivo contain an abundance of the hydrogen nuclei, which consist of positively charged protons. The approximate 60 % of a human body is composed of water, which has the hydrogen nucleus. Since each tissue has individual density and condition of the hydrogen, a signal intensity from each tissue in vivo can be measured and constructs an image.

A spinning charged particle creates an electromagnetic field. All of nuclei with an odd number of protons, neutrons or both particles have specific energy levels. The energy level is related to a property of the nucleus called spin quantum number **I**. A spin quantum

number of the hydrogen nucleus is

$$\mathbf{I}(\mathrm{H}) = \frac{1}{2}. \tag{2.1}$$

The number of energy states of the hydrogen nucleus is calculated from this quantum number as

$$\text{The number of energy states} = 2\mathbf{I} + 1 = 2. \tag{2.2}$$

We express two energy states of the hydrogen proton represented as -1/2 and +1/2. This means that some hydrogen protons spinning about a certain axis and the other protons spinning in the opposite way. The spinning protons in two different states create magnetic fields pointing the axes of rotation toward the directly opposite orientations according to the spinning way. When the nucleus contains an even number of protons, every proton is paired in two directions of magnetic fields, then the magnetic fields cancel each other out. In contrast, when an odd number of protons exists, an unpaired single proton always exists. The magnetic field of this unpaired proton yields a magnetic dipole moment of the nucleus. Since the hydrogen nucleus has a single proton, its magnetic dipole moment is equivalent to that of a single proton.

In the case without any external magnetic fields, the axes of the magnetic dipole moments of a number of protons point at random ways. The total magnetic dipole moments of the protons vanishes. On the other hand, the presence of an external large magnetic field B_0 makes the proton spins align in the direction along the axis of B_0. Although an approximately half of the numbers of protons point at the same direction as B_0 and the others point in the opposite direction. The number of protons along the same orientation as B_0 is slightly larger than that along the opposite direction. An external magnetic field B_0 increases the number of protons in the same direction as its orientation. The net magnetization created by spins increases exponentially in the time constant T_1 described by the expression $1 - \exp(-t/T_1)$.

In addition, a proton begins to precess about the axis of the applied external magnetic field. This precession is called the Larmor precession. The angular precession frequency ω_0 depends on the nucleus's inherent proportionality factor called the gyromagnetic ratio γ and the strength of the external static magnetic field B_0 [42].

$$\omega_0 = \gamma B_0. \tag{2.3}$$

This is called the Larmor equation [43]. The gyromagnetic ratio γ is

$$\frac{\gamma}{2\pi} = 42.58\,(\mathrm{MHz/T}), \tag{2.4}$$

for hydrogen protons [44].

Since all individually precessing spins are all out of phase with each other in a large static magnetic field, the net magnetization vector $\boldsymbol{M}$ does not precess and aligns along the direction of the magnetic field. The external static magnetic field always points toward the direction of the z axis in a three-dimensional (x, y, z) coordinate system. Therefore the direction of the net magnetization vector $\boldsymbol{M}$ is also in the z orientation. The net magnetization does not have components along axes perpendicular to the z axis in this situation.

Under the external large magnetic field B_0, we transmit an electromagnetic wave called RF (Radio Frequency) pulse, which has a frequency matching the frequency of the precession of protons along the x axis perpendicular to the direction of B_0. The resonance then occurs, and the protons can obtain more energy from the RF pulse. The protons lined up with the static magnetic field B_0 are in the lower-energy state. In contrast, the protons aligned in the opposite direction are in the higher-energy state. When the states of protons are in balance in the presence only of the external static magnetic field, the number of protons in the lower-energy state is greater than that in the higher-energy state. Some protons from the lower-energy state are boosted to the higher-energy state by the resonance with the RF pulse.

After an application of the RF pulse with a strength B_1, the net magnetization vector $\boldsymbol{M}$ begins to precess about the x axis in the yz plane at a frequency $\omega_1 = \gamma B_1$. The strength B_1 of the magnetic field for the RF pulse is much weaker than B_0, which is that of the external static magnetic field. Therefore, the frequency of precession ω_1 is much slower than the precessional frequency ω_0 by the static magnetic field. The RF pulse is added for the duration time τ. The flip angle θ of the net magnetization vector $\boldsymbol{M}$ from the z axis into the xy plane can be determined by [45]

$$\theta = \gamma B_1 \tau. \tag{2.5}$$

In addition, the axes of protons' spins begin precessing about the z axis in phase with each other by induction of the RF pulse. Since each proton precesses at the frequency ω_0, the summation of magnetization vector $\boldsymbol{M}$ is also precessing at the frequency ω_0. The protons precess about the z axis at the frequency ω_0 and about the x axis at the frequency ω_1 simultaneously. These two precessional motions lead to a rapid precession around the z axis, which slowly spiral down into the xy plane. If we observe this motion within the frame of reference, which rotates on the z axis at the Larmor frequency ω_0, we only notice the slow precession of the protons' spins from the z axis into the xy plane. In this rotating coordinate system, the net magnetization $\boldsymbol{M}$ can be described by M_{xy} which is the component of $\boldsymbol{M}$ in the xy plane, and M_z which is the component of $\boldsymbol{M}$ along the z axis (Figure 2.1). Since we are capable to measure the oscillations only in the xy plane, we receive signals based on the component of M_{xy}.

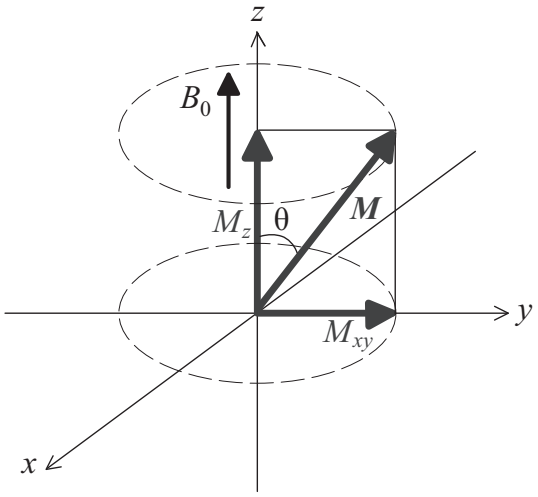

Figure 2.1: The net magnetization $\boldsymbol{M}$ can be divided to two components M_{xy} in the xy plane and M_z along the z axis in the rotating coordinate system.

When the RF pulse causes the entire vector flipping into the xy plane, the magnitude of M_{xy} equals to the magnitude of M_0, which is the maximum value along the z axis before the flip. This type of RF pulse is called the 90° RF pulse. If the RF pulse has twice the power of the 90° RF pulse, the net magnetization vector $\boldsymbol{M}$ is inverted by the RF pulse. We call this the 180° RF pulse.

Once the RF pulse is turned off, the protons release their energy given by the RF pulse and the axes of spins are relaxing toward the equilibrium state. Although all protons rotate in phase immediately after the induction of the 90° RF pulse, the spins get out of phase with each other after the RF pulse is turned off. This dephasing is caused by two phenomena; interactions between spins and inhomogeneities of the external field. The spinning proton creates its own small magnetic field. The direction of the small magnetic field depends on the direction of the axis of the spin; aligning in or against the orientation of B_0. The created magnetic field by protons changes magnitude of the magnetic field, which the adjacent spinning protons are exposed. This interaction causes the inherent dephasing. In addition, notice that the homogeneity of the static magnetic field cannot always hold due to the limitation of the experimental equipment even if we employ a magnetic field as stable as possible.

The component M_{xy} of the net magnetization vector decays rapidly and the component M_z recovers slowly along the z axis. These decrease and recovery occur in the result of two events; the spinning protons go back to the lower-energy state and get out of phase.

The longitudinal component M_z after the RF pulse is turned off saturates as

$$M_z(t) = M_0 \left\{ 1 - \exp\left(-\frac{t}{T_1} \right) \right\}, \tag{2.6}$$

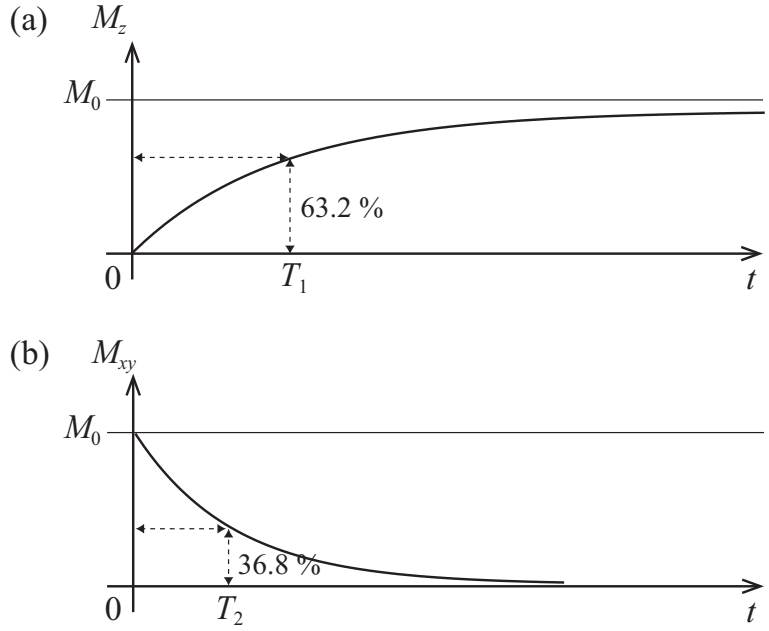

Figure 2.2: (a) The recovering of the longitudinal component (relaxation time T_1) and (b) the decay of the transverse component (relaxation time T_2) after the RF pulse is turned off.

where the rate of the M_z recovering until the M_0 is expressed by the longitudinal relaxation time T_1 (Figure 2.2 (a)). This behavior is called the T_1 relaxation. The length of T_1 depends on the tissue in vivo. For instance, the gray matter has $T_1 \simeq 1124$ (ms), T_1 of the white matter is about 884 (ms) and that of the cerebrospinal fluid is about 2650 (ms) when $B_0 = 1.5$ (T).

The transverse component M_{xy} decays at a rate characterized by the time constant T_2 (Figure 2.2 (b)).

$$M_{xy}(t) = M_0 \exp\left(-\frac{t}{T_2}\right). \tag{2.7}$$

This decaying behavior depends on the interactions between spins. Thus, the recovery of magnetization along the z axis and the decay of magnetization within the xy plane are caused by two independent processes in two different rates. The component M_{xy} decreased to about 36.8 % of the M_0 in T_2. In the 1.5 (T) magnetic field, T_2 of the gray matter, the white matter and the cerebrospinal fluid are about 95 (ms), 72 (ms) and 180 (ms), respectively.

In actual situation, due to inhomogeneities in the external magnetic field, the actual T_2 relaxation time is always less than the ideal T_2 relaxation time. The actual time constant T_2 is given by ${T_2}^*$. ${T_2}^*$ decay is always faster than T_2 decay. The relation between T_2 and ${T_2}^*$ is described by the following equation, when the magnetic field inhomogeneity of the

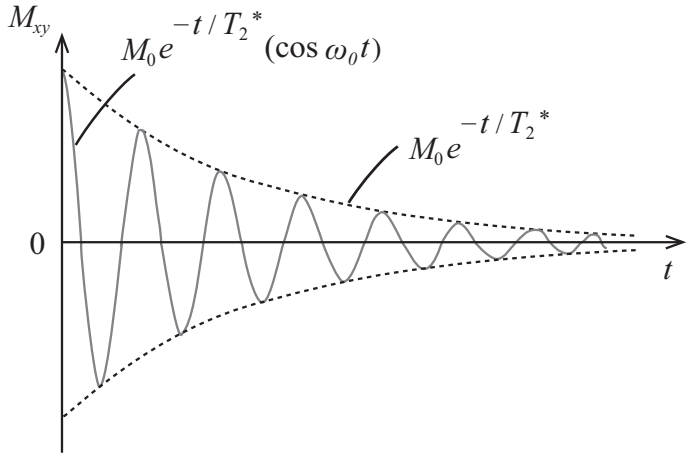

Figure 2.3: The behavior of decay and oscillation of the transverse magnetization according to a free induction decay (FID).

external magnet is ΔB,

$$\frac{1}{T_2^*} = \frac{1}{T_2} + \gamma \Delta B. \tag{2.8}$$

Since the protons are precessing about the z axis at the frequency ω_0, the transverse component also precesses at the frequency ω_0. The transverse component creates an oscillation, and decay of the magnitude signal (Figure 2.3).

$$M_{xy}(t) = M_0 \exp\left(-\frac{t}{T_2^*}\right)(\cos\omega_0 t). \tag{2.9}$$

This is called a free induction decay (FID). In MRI we measure the induced current derived from this transverse component M_{xy} as a received signal.

2.1.2 Principle of MRI

In order to obtain the necessary information to create an image using the procedures described in the previous section, we must repeat the procedures in many times. The gradients of the magnetic fields, which have different magnitude depending on the location in vivo, are used to encode the signal spatially. We collect multiple signals while applying the RF pulse in many times with various gradients.

The net magnetization precesses around the z axis, and only the rotation of the magnetization can create a signal. The transverse magnetization rotates in the xy plane and creates a oscillating signal. The recovering longitudinal magnetization along the z axis does not rotate and does not creates a signal. The RF transmitter and receiver coil exists in the direction of the x axis from a location of the observed proton. Since we can

detect only the oscillating signal, only the oscillating signal created by the rotation of the transverse magnetization along the x axis can be measured. Nevertheless the changes of the longitudinal component affect the received signal due to applying RF pulse multiple times. The magnitude of the longitudinal component before the second RF pulse is induced leads to the smaller value of the transverse magnetization immediately after the second RF pulse, when the second RF pulse is induced before the longitudinal magnetization does not recover completely. We can also measure the signal derived from the longitudinal component indirectly.

If we apply the RF pulse at intervals of TR (Repetition time), the longitudinal component M_z of the net magnetization vector just before the second RF pulse is applied is given as follows derived from Equation (2.6).

$$M_z(TR) = M_0 \left\{ 1 - \exp\left(-\frac{TR}{T_1} \right) \right\}. \tag{2.10}$$

In the second excitation the maximum value of the longitudinal component $M_z(TR)$ is less than the original magnitude of the magnetization vector M_0 because the second 90° RF pulse is induced before M_z recovers completely.

The delay cannot be avoided during a transmission, which the signal arisen from the tissue to the receiver coil. Then we perform measurement in a short period of time TE (Echo delay time or Time to echo) after the second RF pulse. The net magnetization just before the second RF pulse is applied has the longitudinal component described as Equation (2.10). Therefore, the transverse component M_{xy} of the net magnetization vector in TE after the second excitation by the RF pulse is given by combination of Equations (2.7) and (2.10)

$$\begin{aligned} M_{xy}(TR+TE) &= M_z(TR) \exp\left(-\frac{TE}{T_2^*} \right) \\ &= M_0 \left\{ 1 - \exp\left(-\frac{TR}{T_1} \right) \right\} \exp\left(-\frac{TE}{T_2^*} \right). \end{aligned} \tag{2.11}$$

The magnitude of the net magnetization M_0 is proportional to the number of mobile protons because mobile protons create a signal. The signal intensity S_0 which we measure is also proportional to the number of protons $N(\mathrm{H})$.

$$S_0 \propto N(\mathrm{H}) \left\{ 1 - \exp\left(-\frac{TR}{T_1} \right) \right\} \exp\left(-\frac{TE}{T_2^*} \right). \tag{2.12}$$

Since the different tissues have the different values of T_1 and $T_2{}^*$, we can obtain the tissue contrast by setting the appropriate TR time and TE time. In brain tissues, both of the values of T_1 and $T_2{}^*$ in the white matter are smaller than those in the gray matter, and those values in the gray matter are smaller than those in the cerebrospinal

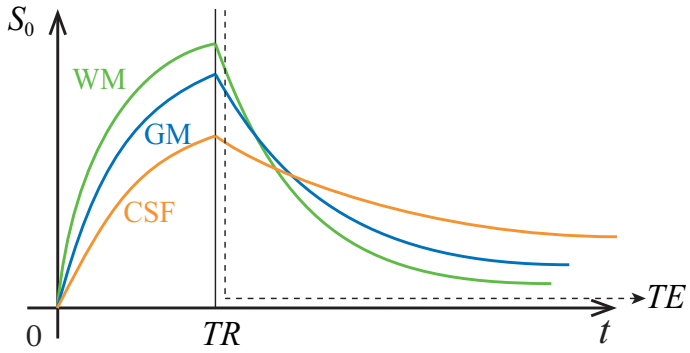

Figure 2.4: A T_1 recovery curve after the first RF pulse and a T_2 decay curve after the second RF pulse for the white matter (WM), the gray matter (GM) and the cerebrospinal fluid (CSF).

fluid. Accordingly the net magnetization of the white matter turn into the xy plane most quickly in comparison to that of the gray matter and the cerebrospinal fluid, and the transverse magnetization of the white matter increases most rapidly after the first RF pulse. The signal intensity of the white matter is always the largest in the T_1 recovery curve after the first RF pulse. The longitudinal component of the net magnetization vector of the white matter recovers most quickly among these three kinds of tissues, when we apply the second RF pulse. After the second RF pulse is induced, the decay of the transverse component of the white matter exhibits the rapidest behavior. Therefore the signal intensity of the white matter is reduced more quickly than that of the gray matter and the cerebrospinal fluid after a certain time (Figure 2.4).

If TR goes to infinity $1 - \exp(-TR/T_1) \to 1$ in Equation (2.11). We can get rid of the T_1 component when TR is very long. Actually the long TR reduces the T_1 effect. We can minimize the T_1 effect with a certain value of TR, which is about 4 to 5 times T_1.

In contrast, we can get a tissue contrast derived from T_1 with short TR as the following equation because the values of T_1 of the tissue A and B are different.

$$\frac{S_{0(\text{tissue A})}}{S_{0(\text{tissue B})}} = \left\{1 - \exp\left(-\frac{TR}{T_{1(\text{tissue A})}}\right)\right\} / \left\{1 - \exp\left(-\frac{TR}{T_{1(\text{tissue B})}}\right)\right\}. \tag{2.13}$$

Although short TR enhances the tissue contrast related to T_1, we end up with no signal, namely, $1 - \exp(-TR/T_1) \to 0$, if TR is close to zero. Therefore, a certain value of TR, which is not so different from the T_1 of the tissue under study, suits to the measurement of the T_1 contrast.

If TE is close to zero, $\exp(-TE/T_2^*) \to 1$ in Equation (2.11). The short TE reduces the $T_2{}^*$ effect. When we have a long TE, $T_2{}^*$ contrast between tissues is enhanced. However the signal noise ratio (SNR) is low because of the greater signal decay for a long TE. We end up with no signal, i.e. $\exp(-TE/T_2^*) \to 0$, if TE is too long.

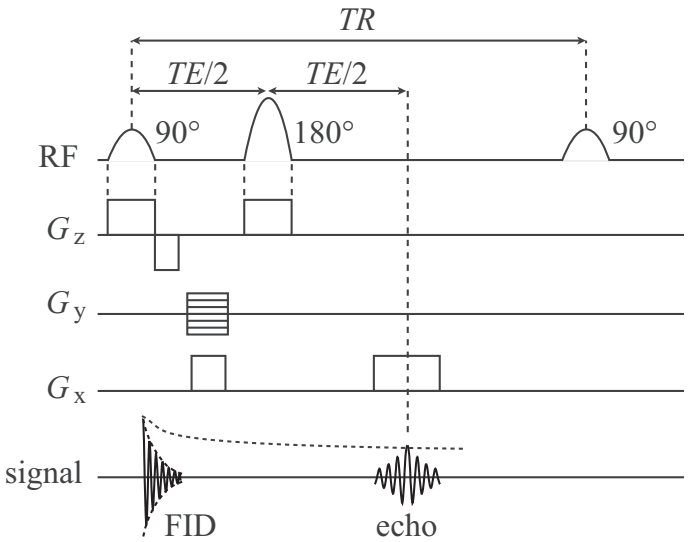

Figure 2.5: The spin echo pulse sequence.

Summarizing the property of TR and TE length, properly short TR and short TE enhance the T_1 contrast. This enhanced image is called T_1-weighted image. The adequately long TR and long TE enhance the $T_2{}^*$ contrast. We call this enhanced image a T_2-weighted image.

2.1.3 Imaging sequence

When we measure the signal represented by Equation (2.12), we can employ various methods called pulse sequence. What kind of RF pulse or gradient magnetic field we apply are selected. We can choose a pulse sequence that suits the purpose, on which we focus. Three representative pulse sequences are introduced below.

Spin echo pulse sequence (SE)

In the spin echo pulse sequence, we use the RF pulse two times in one excitation set. After applying the first 90° RF pulse we apply an additional rephasing 180° RF pulse in the $TE/2$ second. The signal is received in TE second after the first 90° RF pulse (Figure 2.5). The next 90° RF pulse is added at TR. Although the spin echo pulse sequence takes relatively long time, this method can eliminate the dephasing effect caused by the inhomogeneity of the external static magnetic field.

Gradient echo pulse sequence (GRE)

The bi-lobed gradient, which has a negative lobe as well as a positive lobe that has twice as the duration time as a negative lobe, is used instead of using 180° RF pulse in a

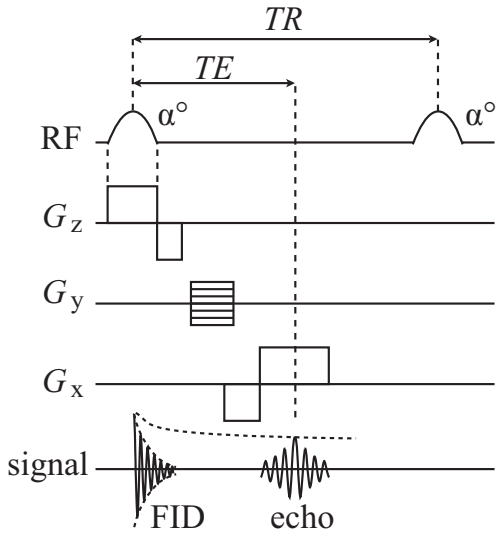

Figure 2.6: The gradient echo pulse sequence.

gradient echo pulse sequence (Figure 2.6). In this method, the spins in the transverse plane are intentionally dephased by a phase-encoding gradient after the RF pulse for a small flip angle. After that the positive lobe gradient is applied to rephase the spins, and the refocusing occurs at the midpoint of the positive lobe, then we acquire the signal at this point. Although we can reduce the scan time significantly allowing a very short TR value owing to a small flip angle by the RF pulse, the method has some disadvantages, for instance increase in the sensitivity to magnetic field inhomogeneity, intra-voxel dephasing and magnetic susceptibility artifact because of absence of the rephasing 180° RF pulse.

Echo planar imaging (EPI)

Single-shot EPI requires only a single excitation to obtain whole signal of a single slice. Newer EPI use a blipped phase-encode gradient (Figure 2.7). Enough information is constructed to create an image of a single slice by multiple gradient reversals, producing multiple gradient echoes in a single acquisition after a single RF pulse. Then, extremely high computational power is demanded. Although it takes approximately only 100 milliseconds to scan a single slice, the fat suppression with presaturation techniques is required because fat-water chemical shift artifacts can be problematic with the short TEs.

2.2 Principle of Diffusion weighted imaging (DWI)

In order to establish the diffusion tensor imaging, some images obtained with the diffusion weighted imaging (DWI) are required. The technique of DWI reflects the molecular motion within a voxel in the signal intensity. The water molecule moves around following

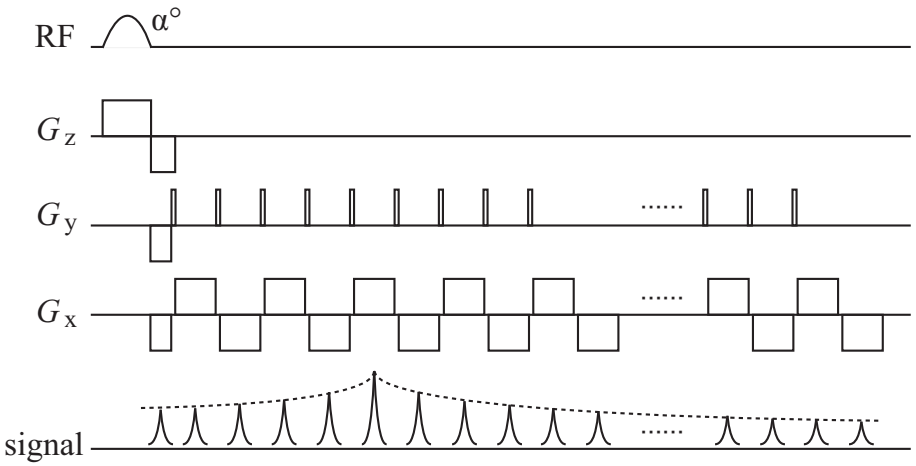

Figure 2.7: The pulse sequence of the echo planar imaging.

thermal Brownian motion unless it is frozen. This movement is called 'diffusion'. In this section, we describe the principle of DWI with mathematics.

2.2.1 Basics of diffusion measurement

When a pair of dephasing and rephasing gradients with the opposite direction each other are applied, the signal in MRI is sensitized to the diffusion of water molecules [46]. These dephasing and rephasing gradients pulse are called the motion probing gradient (MPG). Seeing Figure 2.8, we recognize the signal loss exists when molecules move. Each circle indicates a single molecule with an arrow representing a phase of the transverse vector of the precessing magnetization. We assume each mass of nine molecules exists in a single voxel, signifying the original position of each molecule by the coloring.

After all molecules precess in phase, the dephasing gradient is applied This is shown in the second column in Figure 2.8. The direction of MPG is left; i.e. the strength of the magnetic field is large in the left side and small in the right side. The magnetization vector precesses more rapidly in the left side and more slowly in the right side. A color of an arrow represents the rapidity of precession; the blue, light blue, and green colors indicate the fastest, medium, and the slowest precession, respectively. The phase of the left molecule precedes counterclockwise that of the right molecule. The dephasing gradient is induced in order to determine locations of molecules along the direction of MPG. The signal reduces after the dephasing gradient is applied, since the molecules precess out of phase.

During the diffusion time the magnetic field does not have gradient any more. This is shown in the third column in Figure 2.8. In this situation, all molecules precess in the same frequency with different phases, and the signal keeps small value. In the condition

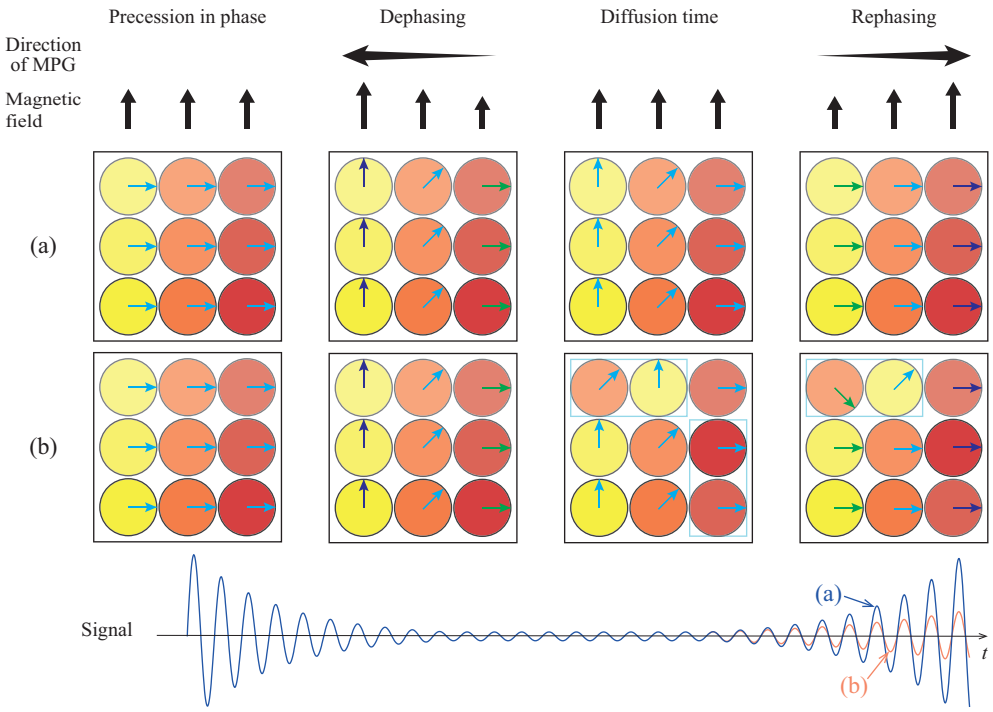

Figure 2.8: The effects of molecular motions in an application of a pair of gradients, which have the opposite directions.

(a) any molecules do not move. Some molecules surrounded by light blue frames exchange their locations in the condition (b). Two molecules (yellow and orange) moves along the direction of MPG, and the other two molecules (deep and light red) moves perpendicular to the orientation of MPG.

The rephasing gradient, which has the opposite direction from the dephasing gradient, is applied after the diffusion time. This is the situation in the most right column in Figure 2.8. In the condition (a) all phases of molecules align, since the weak magnetic field is applied to the molecules with the advanced phase in the left side, and the strong magnetic field is induced to the molecules with the behind phase in the right side. Then the signal recovered as large as that before the dephasing gradient. In the condition (b) the phases of the two molecules, which exchange their locations along the direction of MPG during the diffusion time, do not align the phases of the other molecules. The phases of the two molecules, which move perpendicular to the orientation of MPG are not affected. Then the summation of signals caused by all molecules reduces in the condition (b). Therefore, we can detect the diffusional motion of water molecules by an application of MPG two times in the opposite directions.

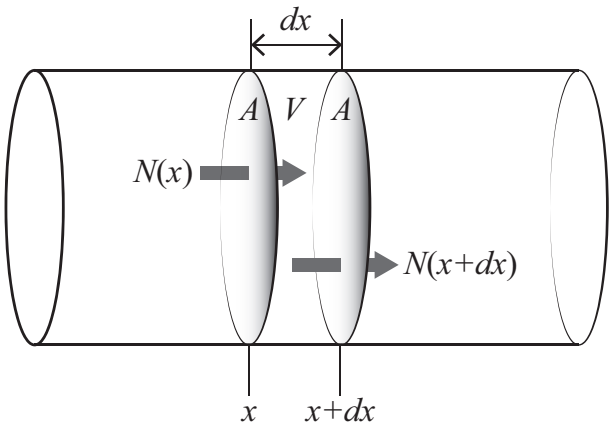

Figure 2.9: The amount of changing for the number of molecules in a thin column with a volume V is expressed in the difference between the number of molecules that flow into this column $N(x)$ and the number of molecules drained from this column $N(x + dx)$.

2.2.2 Diffusion equation

The diffusion equation is derived from Fick's laws of diffusion [47]. The diffusion equation describes the diffusion phenomenon of molecules quantitatively. Fick's first law postulates that the flux of molecules goes from regions of high concentration to regions of low concentration, with a magnitude that is proportional to the concentration gradient at the location. Being considered only the diffusion along the x axis, the number of molecules $N(x, t)$ moving through the plane at a location x per unit area at a time point t is expressed as

$$N(x,t) = -D\frac{\partial c(x,t)}{\partial x}, \tag{2.14}$$

where $c(x, t)$ is a concentration at x. The proportional constant D indicates a diffusion coefficient, which unit is (m^2/s), where the unit of $N(x, t)$ is the number per m^2s.

Now we assume a thin column of an infinitesimal width dx with a base area of A adjacent to a location x (Figure 2.9). The amount of molecules dN increasing in an infinitesimal time dt is expressed in the difference between the number of molecules that flow into this column and the number of molecules drained from this column.

$$dN = A[N(x) - N(x + dx)]dt. \tag{2.15}$$

Since the volume V of this column is described in Adx, Equation (2.15) is transcribed as the following equation, when we divide both members of Equation (2.15) by dx and dt.

$$\frac{1}{V}\left(\frac{dN}{dt}\right) = \frac{N(x) - N(x + dx)}{dx}. \tag{2.16}$$

The number of molecules per unit volume N/V represents the concentration c. The concentration c depends of both of a location x and a time point t. The left side of Equation (2.16) is described in a partial differentiation as

$$\frac{\partial c}{\partial t} = \frac{N(x) - N(x+dx)}{dx}. \tag{2.17}$$

A function that derived function is continuous has the following relation in general.

$$\frac{df(x)}{dx} = \frac{f(x+dx) - f(x)}{dx}. \tag{2.18}$$

This relation becomes in this case as

$$\frac{\partial N}{\partial x} = \frac{N(x+dx) - N(x)}{dx}. \tag{2.19}$$

From Equations (2.17) and (2.19), the relational expression is derived as

$$\frac{\partial c}{\partial t} = -\frac{\partial N}{\partial x}. \tag{2.20}$$

We calculate the partial differentiation for x to the both side of Equation (2.14).

$$\frac{\partial N}{\partial x} = -D\frac{\partial^2 c}{\partial x^2}. \tag{2.21}$$

Then, the diffusion equation expressed in a partial differential equation of second order is derived from Equations (2.20) and (2.21) as

$$\frac{\partial c}{\partial t} = D\frac{\partial^2 c}{\partial x^2}. \tag{2.22}$$

The diffusion equation is solved for c under two boundary conditions; $c(x,t) = 0$ in all location x except for $x = 0$ at $t = 0$, and $\int c(x,t)dx = 1$.

$$c(x,t) = \frac{1}{\sqrt{4\pi Dt}} \exp\left(\frac{-x^2}{4Dt}\right). \tag{2.23}$$

This equation indicates Gaussian distribution with the mean square displacement $\sigma^2 = \langle x^2 \rangle = 2Dt$ with respect to the origin of the coordinate axes.

2.2.3 Signal intensity of DWI

The amount of phase difference ϕ at a location x is introduced by a gradient pulse with a strength of G and a duration time of δ [46].

$$\phi(x) = \exp\left(i\gamma G\delta x\right), \tag{2.24}$$

where γ is the gyromagnetic ratio introduced in Equation (2.4). In this situation the phase of the net magnetization change $\phi(x)$ at the location x with respect to the origin of

the defined coordinate, after the magnetic field with the strength of Gx for the time of δ The MRI signal is determined by a phase of a molecule and a concentration of molecules at the location. The total signal is calculated by summing up the product of concentration and signal phase along location x from Equations (2.23) and (2.24).

$$\text{Signal} = \int_x c(x,t)\phi(x)dx = \frac{1}{\sqrt{4\pi Dt}} \int_x \exp\left(\frac{-x^2}{4Dt}\right) \exp\left(i\gamma G\delta x\right) dx. \tag{2.25}$$

When we do not apply the gradient ($G = 0$), the signal becomes

$$\text{Signal} = \int_x c(x,t)dx = \frac{1}{\sqrt{4\pi Dt}} \int_x \exp\left(\frac{-x^2}{4Dt}\right) dx = 1, \tag{2.26}$$

which satisfies the boundary condition of the diffusion equation (2.22).

We can calculate Equation (2.25) as follows;

$$\text{Signal} = \exp\left(-\gamma^2 G^2 \delta^2 Dt\right), \tag{2.27}$$

where the signal intensity is normalized, so that its maximum value is 1 when we do not apply the gradient ($G = 0$). In an actual measurement in a MRI scanner, we have a certain number for the signal intensity. The relation between the signal intensity with diffusion weighting S and without diffusion weighting S_0 is derived from Equations (2.26) and (2.27).

$$S = S_0 \exp\left(-\gamma^2 G^2 \delta^2 Dt\right). \tag{2.28}$$

This equation is realized only when the gradient pulses are applied instantaneously and the diffusion of water molecules starts after the application of the gradient is completed.

In the practical situation, molecules move during the application of the gradient, since the gradient time δ is usually long. The phase difference of net magnetization depends on the magnitude of the magnetic field at the time point. The magnitude of the gradient magnetic field is time variant, the maximum value of the magnitude is $G\delta$ mentioned above, which represents the total of applied gradient magnetic field. Figure 2.10 represents the simplified sequence for DWI and the magnitude of the applied magnetic field. We assume that a pair of gradient pulses with the opposite direction (Figure 2.10 (a) and (b)) is applied at an interval. The introduced phase difference in Equation (2.24) is a function of both location x and time t.

$$\phi(x,t) = \exp\left(i\gamma G(t)tx\right). \tag{2.29}$$

In this situation Equation (2.25) becomes

$$\text{Signal} = \int_x c(x,t)\phi(x,t)dx = \frac{1}{\sqrt{4\pi Dt}} \int_x \exp\left(\frac{-x^2}{4Dt}\right) \exp\left(i\gamma G(t)tx\right) dx. \tag{2.30}$$

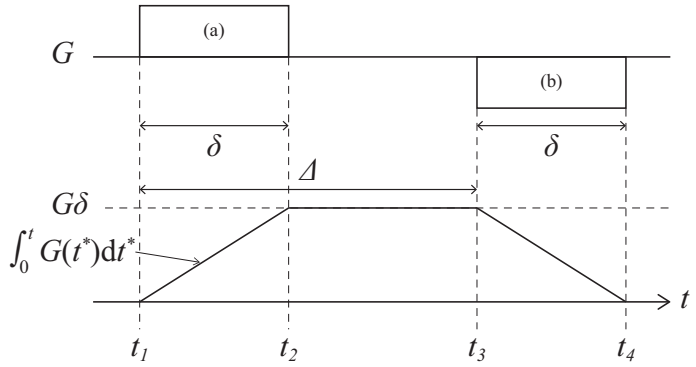

Figure 2.10: The simplified sequence for DWI and the magnitude of the applied magnetic field.

After we integrate not only location x but also time t, the relation between the signal intensity with diffusion weighting S and without diffusion weighting S_0 is

$$S = S_0 \exp\left(-D\gamma^2 \int_{t_1}^{t_4} \left(\int_0^t G(t^*)dt^*\right)^2 dt\right). \tag{2.31}$$

The first integral integrates over t^*, which starts from the application of the first gradient (Figure 2.10 (a)). In order to integrate this function over time period $t_1 - t_4$, we divide the time into three segments. Since the strength of the gradient magnetic field increase linearly (Gt), constant ($G\delta$), and decrease linearly ($G\delta - G(t-t_3)$) (Figure 2.10), Equation (2.31) becomes

$$\ln\frac{S}{S_0} = -D\gamma^2\left(\int_{t_1}^{t_2} G^2t^2dt + \int_{t_2}^{t_3} G^2\delta^2dt + \int_{t_3}^{t_4} \left(G\delta - G(t-t_3)\right)^2 dt\right). \tag{2.32}$$

We define time t_1 as the origin of time axis ($t_1 = 0$), and time $t_2 = \delta$ in order to simplify this equation. In addition, we define the time interval $t_3 - t_1 = \Delta$ (Figure 2.10). Then time $t_4 = \Delta + \delta$, and the previous equation is

$$\begin{aligned}
\ln\frac{S}{S_0} &= -D\gamma^2\left(\int_0^{\delta} G^2t^2dt + \int_{\delta}^{\Delta} G^2\delta^2dt + \int_{\Delta}^{\Delta+\delta} \left(G\delta - G(t-\Delta)\right)^2 dt\right) \qquad (2.33)\\
&= -D\gamma^2\left(\frac{1}{3}G^2\delta^3 + G^2\delta^2(\Delta-\delta) + \frac{1}{3}G^2\delta^3\right)\\
&= -\gamma^2G^2\delta^2\left(\Delta - \frac{\delta}{3}\right)D.
\end{aligned}$$

Therefore, the ratio of the signal intensities of S and S_0 is controlled by some parameters G, δ, and Δ. These parameters are often abbreviated to a single parameter b.

$$b = \gamma^2G^2\delta^2\left(\Delta - \frac{\delta}{3}\right). \tag{2.34}$$

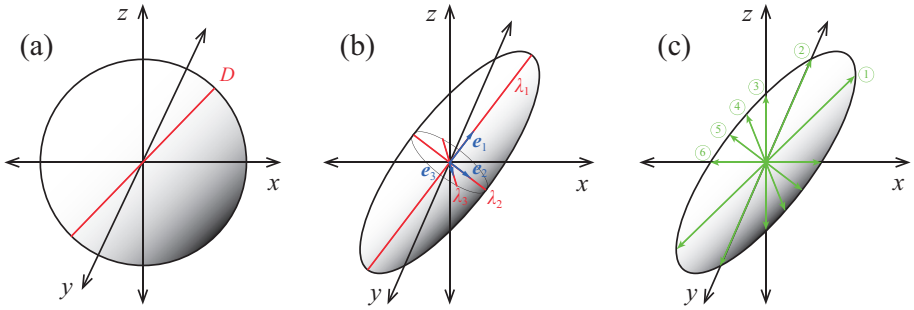

Figure 2.11: The diffusion ellipsoid. (a) The sphere in the case of isotropic diffusion. (b) The ellipsoid in the case of anisotropic diffusion. The shape and orientation of this ellipsoid is characterized by six parameters; λ_1, λ_2, and λ_3 for the shape, and $\boldsymbol{e}_1$, $\boldsymbol{e}_2$, and $\boldsymbol{e}_3$ for the orientation. (c) The measurements are performed six times with six independent axes in order to uniquely determine the ellipsoid.

Then the preceding equation is simplified to

$$\ln \frac{S}{S_0} = -bD. \tag{2.35}$$

Finally, the diffusion coefficient is obtained from the amount of the signal loss of the diffusion weighted image in comparison to the image without MPG.

[46, 11, 48]

2.3 Principle of Diffusion tensor imaging (DTI)

In the previous section, we provided the principle of the diffusion weighted imaging, which measured a diffusion along only a single predetermined axis. Although the measurement with DWI is enough to detect the magnitude of the diffusion, if we measure free water diffusion, the diffusion process has directionality when we measure water diffusion inside a living system. Therefore, we also need to detect the orientation of water diffusion and need more elaborate diffusion measurement and data processing. The representative method of such measurement is the diffusion tensor imaging (DTI) [46].

In the case of the isotropic diffusion (Figure 2.11 (a)), water molecules diffuse in all directions with the same amount like a sphere, and the diffusion can be described only a single parameter, the diffusion constant D in the previous section, which relates to the diameter of the sphere. When water molecules diffuse anisotropy (Figure 2.11 (b)), the shape representing the diffusion becomes an ellipsoid. We assume that water molecules diffuse following the Gaussian distribution and the diffusion property is elliptic. This type of diffusion is called anisotropic diffusion, and the ellipsoid is called a diffusion ellipsoid. In the biological tissues, water molecules tend to diffuse along the ordered structures such

as axonal tracts in nervous tissues. In the case of the anisotropic diffusion, the shape of the ellipsoid is characterized by three lengths for the longest, meddle, and shortest axes perpendicular to each other. These three lengths are called eigenvalues; λ_1, λ_2, and λ_3 in Figure 2.11 (b). In addition, the orientation of the ellipsoid is defined by three independent vectors $\boldsymbol{e}_1$, $\boldsymbol{e}_2$, and $\boldsymbol{e}_3$ coincide with three eigenvalues. Therefore we need to perform at least six measurements along six independent axes in order to determine the ellipsoid uniquely, since six parameters are needed to characterize the diffusion ellipsoid Figure 2.11 (c).

2.3.1 Measurement of DTI

In order to define the shape and orientation of the diffusion ellipsoid, we would like to measure six parameters; three eigenvalues λ_1, λ_2, and λ_3, and three eigenvectors $\boldsymbol{e}_1$, $\boldsymbol{e}_2$, and $\boldsymbol{e}_3$. However we cannot measure these parameters directly, since we cannot determine the directions of the principal axes of the ellipsoid before the measurements are performed. Then we introduce a symmetric 3×3 tensor called diffusion tensor $\overline{\mathbf{D}}$.

$$\overline{\mathbf{D}} = \begin{bmatrix} D_{xx} & D_{xy} & D_{zx} \\ D_{xy} & D_{yy} & D_{yz} \\ D_{zx} & D_{yz} & D_{zz} \end{bmatrix} \tag{2.36}$$

The six parameters are calculated by diagonalization of this tensor. The off-diagonal terms are 0 when the principal axes (eigenvectors) of the diffusion ellipsoid align to the x, y, and z coordinate system. The terms D_{xy}, D_{zx}, and D_{yz} carry information related to a rotation about the z, y, and x axes, respectively. The eigenvalues, which provide information about the shape of the ellipsoid, are independent of the rotation of the ellipsoid.

We measure the six diffusion constants described in Equation (2.36), obtaining at least seven images of six diffusion weighted images with MPG along six independent axes and a least diffusion weighted image called a $b0$ image, where $b = 0$. The signal intensity of the diffusion weighted image corresponds to S, and that of the least diffusion weighted image is S_0 in the previous section. We transform Equation (2.35), which is an expression for a diffusion measurement along a single axis, to the equation for an description to treat the anisotropic diffusion.

$$\begin{aligned} \ln \frac{S}{S_0} &= -\int_0^t \gamma^2 \left[\int_0^{t^*} \boldsymbol{G}(t^{**}) dt^{**} \right] \cdot \overline{\mathbf{D}} \cdot \left[\int_0^{t^*} \boldsymbol{G}(t^{**}) dt^{**} \right] dt^* \\ &= -\tilde{\boldsymbol{b}} \overline{\mathbf{D}} \tilde{\boldsymbol{b}}^T, \end{aligned} \tag{2.37}$$

where $\tilde{\boldsymbol{b}}$ is $\gamma \boldsymbol{G} \delta \sqrt{(\Delta - \delta/3)}$. The value of $\tilde{\boldsymbol{b}}$ and $\boldsymbol{G}$ are vectors, since they represent not only the value of gradient strength but also about the orientation.

Since the gradient vector $\boldsymbol{G}$ has three components (G_x, G_y, G_z) corresponding to the x, y, and z axis, the vector $\tilde{\boldsymbol{b}}$ is defined as $\tilde{\boldsymbol{b}} = [\sqrt{b_x}, \sqrt{b_y}, \sqrt{b_z}]$. Then Equation (2.37)

becomes

$$\begin{aligned}
\ln \frac{S}{S_0} &= -\left[\sqrt{b_x}, \sqrt{b_y}, \sqrt{b_z}\right] \begin{bmatrix} D_{xx} & D_{xy} & D_{zx} \\ D_{xy} & D_{yy} & D_{yz} \\ D_{zx} & D_{yz} & D_{zz} \end{bmatrix} \begin{bmatrix} \sqrt{b_x} \\ \sqrt{b_y} \\ \sqrt{b_z} \end{bmatrix} \\
&= -(D_{xx}b_x + D_{yy}b_y + D_{zz}b_z + 2D_{xy}\sqrt{b_x}\sqrt{b_y} + 2D_{zx}\sqrt{b_z}\sqrt{b_x} + 2D_{yz}\sqrt{b_y}\sqrt{b_z}) \\
&= -\boldsymbol{D}\boldsymbol{b} \\
\boldsymbol{D} &= [D_{xx}, D_{yy}, D_{zz}, 2D_{xy}, 2D_{zx}, 2D_{yz}] \\
\boldsymbol{b} &= \left[b_x, b_y, b_z, \sqrt{b_x}\sqrt{b_y}, \sqrt{b_z}\sqrt{b_x}, \sqrt{b_y}\sqrt{b_z}\right].
\end{aligned} \tag{2.38}$$

Therefore, we determine all components of the diffusion tensor with six kinds of the signal intensity S of diffusion weighted images corresponding to six directions of MPG and the signal intensity S_0 of the $b0$ image by the solution of six simultaneous equations. We can calculate the eigenvalues and eigenvectors characterizing the shape and the orientations of the diffusion ellipsoid from the measured diffusion tensor. These measurements and calculations are performed in each voxel in DTI, and the diffusional ellipsoid is defined per voxel.

2.3.2 Expressions of diffusional anisotropy

We introduce three expressions to quantify the condition of the diffusional anisotropy obtained from DTI. We can visualize the degree of the diffusional anisotropy in these expressions, and estimate the feature of the diffusional ellipsoid simply. The expressions are the images of the mean diffusivity (MD) called the MD image and the fractional anisotropy (FA) called the FA image, and the color map. The MD and FA images have a single value per voxel, and they are displayed with gray scale images. In the color map, each voxel has three components assigning the red, green, and blue colors.

We determine the MD value as the mean of three lengths for the longest, middle, and shortest principle axes of the diffusion ellipsoid. The MD value describe the magnitude of the diffusion insensitive to the orientation of the fibers in vivo. The three lengths are represented the eigenvalues of the diffusion tensor λ_1, λ_2, and λ_3 described in the previous subsection. The value of MD is expressed as

$$\mathrm{MD} = \frac{\lambda_1 + \lambda_2 + \lambda_3}{3}. \tag{2.39}$$

We show the example of the MD image in Figure 2.12 (a). The cerebrospinal fluid has especially high signal intensity in the MD image.

The FA value represents the strength of the diffusional anisotropy calculated as

$$\mathrm{FA} = \sqrt{\frac{1}{2}} \frac{\sqrt{(\lambda_1 - \lambda_2)^2 + (\lambda_2 - \lambda_3)^2 + (\lambda_3 - \lambda_1)^2}}{\sqrt{\lambda_1^2 + \lambda_2^2 + \lambda_3^2}}. \tag{2.40}$$

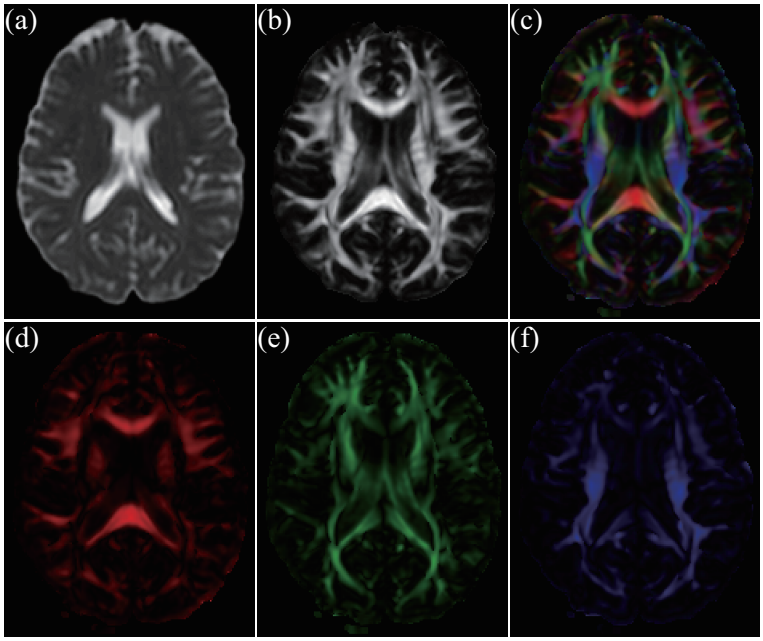

Figure 2.12: The MD image (a), the FA image (b), the color map image (c), and the images representing the x, y, and z components of the color map image (d), (e), and (f).

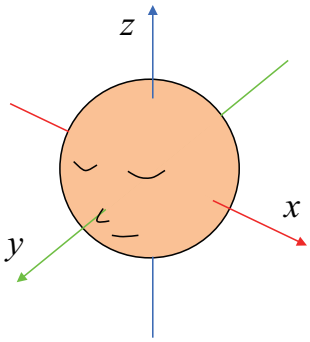

Figure 2.13: The x, y and z direction correspond to the red, green and blue colors, respectively.

This index is scaled between 0 and 1. It is 0 when the diffusion expands isotropy like sphere, and becomes larger as the ellipsoid deviates from a sphere in areas where water molecules perform anisotropic diffusion. We show the example of the FA image in Figure 2.12 (b). The tissues of the white matter, which contains the nerve tract, have high intensity in the FA image. We can recognize the difference between the white matter and the gray matter which is mainly composed of the cortex.

The color map is constructed by the first eigenvector of the diffusion tensor and the FA value. The value of eigenvector contains information about the orientation of the diffusion ellipsoid, and the first eigenvector is considered to represent the direction of the local fiber in vivo. Then the intensity of the color map is defined as

$$\text{Intensity of color map} = \text{FA} \times [e_{1x}, e_{1y}, e_{1z}]. \tag{2.41}$$

The x, y, and z components of the intensity are assigned to RGB colors. Figure 2.13 represents the correspondence between the axes directions and the colors. Although we can visualize the three components separately in Figure 2.12 (d), (e), and (f), the summarized image (c) gives the information about three components simultaneously. In the red image (d) corresponding to the x component, the commissural fibers connecting both hemispheres along the horizontal direction are well recognized. We perceive the high intensity of the association fibers connecting the anterior and posterior parts in each hemisphere along the vertical orientation in the green image (e). The blue image (f) mainly gives information of the projection fibers along the orthogonal direction to the sheet.

2.4 Fiber tracking

The diffusion ellipsoid described in the previous section characterizes the shape and the orientation of the diffusion of water molecules. Water molecules perform anisotropic diffusion in the ordered structure such as nerve tracts in the white matter of the brain. The shape and the orientation of the anisotropic diffusion depends on those of the nerve tract. We can reconstruct the shape and the orientation of the nerve tract three-dimensionally with DTI data. This tract reconstruction technique is called the fiber tracking. We introduce some methods for the fiber tracking.

In order to perform the fiber tracking, we determine the three-dimensional coordinate of a point, from which we start the fiber tracking. We call this point a seed point. The deterministic approach based on 'tract propagation' and probabilistic approach based on 'energy minimization' exist for the reconstruction strategy of the neural pathway [46]. The tracking is propagated step by step from a seed point uniquely and we do not establish a point to terminal the fiber tracking before the fiber tracking is started in the deterministic approach. We call each point tracked step by step a stepping point. In the probabilistic

approach, we determine points to start and end the fiber tracking before we start the fiber tracking, and the most probable pathway to connect the two points is selected on the basis of the likelihood of connection, with information of the pathway and each voxel on the pathway.

There are three principal stages for the deterministic fiber tracking method. The first stage is an estimation of a local fiber orientation. We stabilize the direction of the track propagation at each seed point and stepping point. In the second stage, we propagate the tracked line from the present stepping point to the next stepping point based on the information of the estimation of the orientation. Finally the propagation is terminated in the third stage when the local condition matches some terminal criteria. Here, we describe some commonly used deterministic methods.

2.4.1 Orientation of track propagation

Streamline tracking method (STT)

The orientation of the tracking is determined on the basis of the first eigenvector of the diffusion tensor in each stepping point [14, 15, 16]. This method is called the streamline tracking method (STT) [49]. It was reported that the first eigenvector of the diffusion tensor lies parallel to the local fiber orientation of the white matter [50, 51]. We show the schematic diagram of this method in Figure 2.14 (a). The orange line represents the tracked streamline, and the black arrows indicate the eigenvectors in each stepping point. Although the first eigenvector $\boldsymbol{e}_1$ has an unique direction, the opposite direction of the first eigenvector $-\boldsymbol{e}_1$ is also selectable, since the diffusion ellipsoid has a symmetric shape. The direction that has less angle turned from the vector from the previous stepping point to the present point is selected in these two opposite directions; i.e. the orientation of $\boldsymbol{e}_1$ is chosen when the angle between the previous direction vector and $\boldsymbol{e}_1$ becomes an acute angle, and the direction of $-\boldsymbol{e}_1$ is selected when the angle between the previous vector and $\boldsymbol{e}_1$ establishes an obtuse angle.

Tensor deflection method (TEND)

The other method to define the orientation of the propagation is called the tenor deflection method (TEND). In this method the orientation is determined on the basis of the diffusion tensor in the present stepping point and the direction vector from the previous point to the present point [52, 53, 49]. The outgoing vector in the present stepping point is

$$\boldsymbol{v}_{\text{out}} = \overline{\mathbf{D}}\boldsymbol{v}_{in}, \tag{2.42}$$

where $\overline{\mathbf{D}}$ is the diffusion tensor in the present stepping point and $\boldsymbol{v}_{in}$ represents the incoming line orientation. This is shown in Figure 2.14 (b). The ellipsoid described as

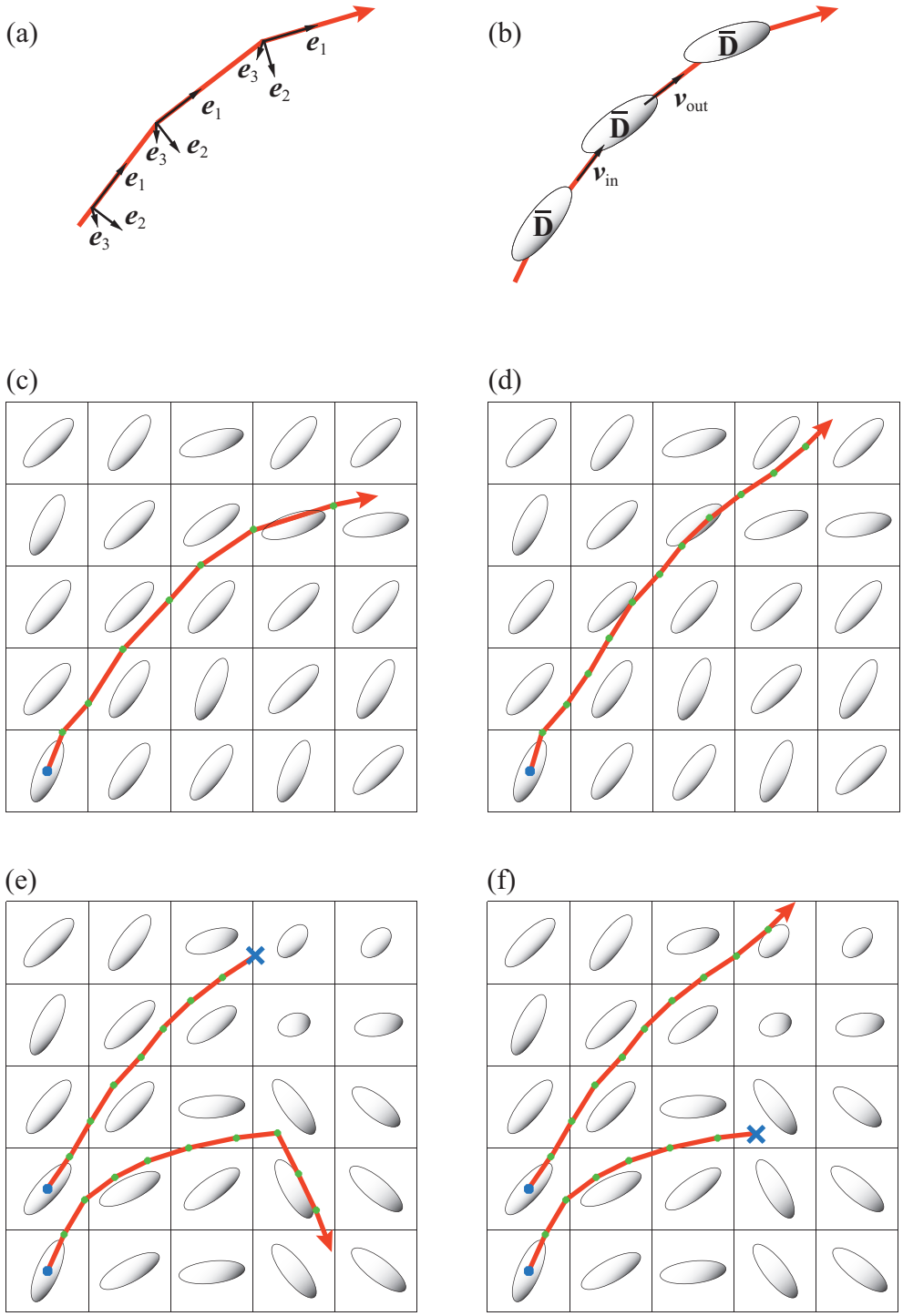

Figure 2.14: The schematic diagrams for the orientation of track propagation by STT method (a) and TEND method (b), the propagation of tracked line by FACT method (c) and Runge-Kutta method (d), and the terminal criteria with the anisotropy (e) and the flip angle (f).

$\overline{\mathbf{D}}$ represents the diffusion tensor in each stepping point, and the black arrows of $\boldsymbol{v}_{in}$ and $\boldsymbol{v}_{\text{out}}$ indicate the incoming and outgoing vectors through the center diffusion tensor for the present stepping point. The strength of the diffusional anisotropy is also reflected to the outgoing vector in this method.

2.4.2 Propagation of tracked line

Fiber assignment by continuous tracking (FACT)

The first method to propagate the tracked line is called the fiber assignment by continuous tracking method (FACT) [14, 54, 17]. In this method the tracking is initiated from the center of a voxel at a certain coordinate, and propagated in the voxel until the edge of the initiating voxel. The line starts the propagation in the next voxel after the orientation of the tract propagation changes on the boundary line of voxels. This schematic diagram is shown in Figure 2.14 (c). The schematic diagram is depicted in two-dimension for simplification, although the actual fiber tracking is performed in three-dimension. The grids represent the boundary lines of voxels, and the ellipsoid indicates the diffusion tensor in each voxel in the picture. The tracking is started at the center of the voxel at the lower left (blue dot) and propagated along the orange arrow changing the orientation on boundary lines. The green dots on the tracked line represent the stepping points.

Euler's method

The trajectory of the propagating line can be represented as a space curve [55, 56]. The relation between a position vector $\boldsymbol{r}(s)$ parameterized by an arc length s on the propagating line and the unit tangent vector $\boldsymbol{t}(s)$ to $\boldsymbol{r}(s)$ at s is represented by a differential equation. With the consideration that the tangent vector $\boldsymbol{t}(s)$ is equated to the unit first eigenvector $\boldsymbol{e}_1$ at the position $\boldsymbol{r}(s)$, we obtain the equation connecting the position vector $\boldsymbol{r}(s)$ and the first eigenvector $\boldsymbol{e}_1$ at the position $\boldsymbol{r}(s)$ [16].

$$\frac{d\boldsymbol{r}(s)}{ds} = \boldsymbol{t}(s) = \boldsymbol{e}_1(\boldsymbol{r}(s)). \tag{2.43}$$

This equation is solved with an initial condition $\boldsymbol{r}(0)$, which specifies a position of a seed point for the fiber tracking.

Euler's method is employed to find the position of the next stepping point on the basis of a solution of the differential equation (2.43) [57]. The position of the next point $\boldsymbol{r}(s_{n+1})$ is estimated from the position $\boldsymbol{r}(s_n)$ and the first eigenvector $\boldsymbol{e}_1(\boldsymbol{r}(s_n))$ of the present point by a choice of a small number h.

$$\boldsymbol{r}(s_{n+1}) = \boldsymbol{r}(s_n) + h\boldsymbol{e}_1(\boldsymbol{r}(s_n)). \tag{2.44}$$

The location of stepping points along the fiber trajectory $\boldsymbol{r}(s)$ is estimated by repetition of this procedure.

In order to obtain more accuracy in the estimation of the location, Runge-Kutta method of the fourth order (RK4) is employed to solve the system of differential equations [57].

$$\begin{aligned} \boldsymbol{k}_1 &= \boldsymbol{e}_1\left(\boldsymbol{r}(s_n)\right) \\ \boldsymbol{k}_2 &= \boldsymbol{e}_1\left(\boldsymbol{r}(s_n) + \frac{h}{2}\boldsymbol{k}_1\right) \\ \boldsymbol{k}_3 &= \boldsymbol{e}_1\left(\boldsymbol{r}(s_n) + \frac{h}{2}\boldsymbol{k}_2\right) \\ \boldsymbol{k}_4 &= \boldsymbol{e}_1\left(\boldsymbol{r}(s_n) + h\boldsymbol{k}_3\right) \\ \boldsymbol{r}(s_{n+1}) &= \boldsymbol{r}(s_n) + \frac{h}{6}\left(\boldsymbol{k}_1 + 2\boldsymbol{k}_2 + 2\boldsymbol{k}_3 + \boldsymbol{k}_4\right). \end{aligned} \tag{2.45}$$

These scheme is shown in Figure 2.14 (d). Each length between the two continuous stepping points is a constant h, and RK4 is performed in each step.

2.4.3 Terminal criteria

Degree of anisotropy

When the degree of anisotropy is lower than the threshold value during the fiber tracking, the propagation is terminated. In low-anisotropy regions, we can assume that the nerve fibers are not ordered or the area contains not the white matter but the gray matter. The FA value, which represents the strength of the anisotropy of the diffusion tensor scaled between 0 to 1, is the representative threshold value for the determination of the anisotropy. The value of FA $> 0.15 - 0.3$ is commonly used for the anisotropy threshold, since the gray matter typically has an FA of $0.05 - 0.15$ [46]. This condition is shown in Figure 2.14 (e), where the shape of the ellipsoid indicates the strength of the anisotropy. The elongate ellipsoids have high degree of the anisotropy, whereas the anisotropy of the circular ellipsoids is the low degree. The tract propagation is terminated at the point with the blue x mark.

Deflected angle

We call the angle between the two continuous direction vectors of the tracking a deflected angle [49].

$$\text{Deflected angle} = \arccos(\boldsymbol{v}_{in} \cdot \boldsymbol{v}_{\text{out}}), \tag{2.46}$$

where $\boldsymbol{v}_{in}$ and $\boldsymbol{v}_{\text{out}}$ represent the incoming vector to and the outgoing vector from the present stepping point, respectively.

When the deflected angle is larger than the threshold value, the fiber tracking is terminated. The large deflected angle indicates a sharp turn of the trajectory. We can

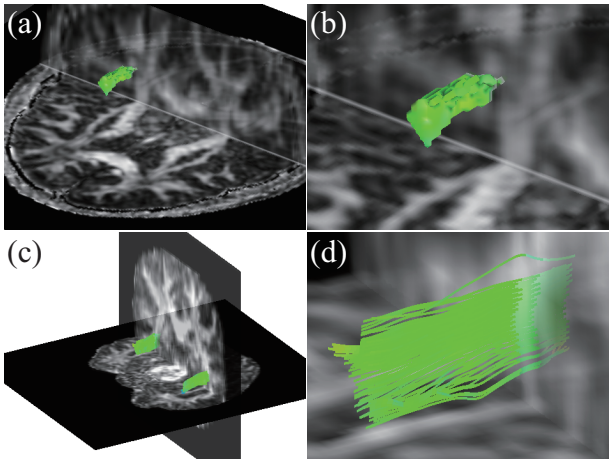

Figure 2.15: The examples of the tractography. (a) The surface of the mass of voxels on the trajectory is colored on the basis of information of the voxels. (b) The close-up image of the picture (a). (c) The trajectory is visualized directly. (d) The close-up image of the tractography (c).

consider that the tracking jumps to adjacent unrelated tracts at the point with the large deflected angle [46]. We select the threshold value corresponding to the shape of the related tracts.

2.4.4 Tractography

The trajectory of the tract propagation is visualized three-dimensionally. This technique is called a tractography. The two types of the tractography techniques exist principally. The first one is a technique that the voxels on the trajectory is colored and the surface of the mass of voxels as a volume data are colored with the information of the trajectory. The examples of the tractography with this method is shown in Figure 2.15 (a) and (b). In this pictures, the coloring is corresponding to the color map; i.e. the x, y, and z components of the direction vector on the trajectory are assigned to the red, green, and blue factors of the color for each voxel, respectively. Figure 2.15 (b) is the close-up image of Figure 2.15 (a). The second technique visualizes the trajectory directly. The location of each stepping point is plotted on the three-dimensional space. The connected line among the points represents the trajectory of the tracked fiber. We show the example of the tractography with this technique in Figure 2.15 (c) and (d). The coloring of the trajectory describes the direction of the tract propagation. In the close-up image (d), we can recognize each trajectory propagated from each seed point.

2.5 Schizophrenia

In this study we focus on the schizophrenia. Schizophrenia is a severe, long-term psychiatric illness and the most debilitating disease of all adult psychiatric disorder [6]. It is characterized by impairments in social functioning, the ability to work, self-care skills, positive and negative symptoms, and cognitive impairments.

The lifetime prevalence of schizophrenia is approximately 1 % of the universal population. Schizophrenia tends to have an episodic course over the lifetime. Patients with schizophrenia have delusions, experience hallucinations, and exhibit confused speech, and grossly disorganized or catatonic behaviors. These symptoms constitute obstacles to daily living. Consequently, a number of patients depend on other people around them to meet their daily living needs.

Although there are many evidence that indicates schizophrenia is a biological illness cased by a variety of factors, such as genetic contributions and early environmental influences like insults to the developing fetus, environmental stress can either precipitate the onset of the illness or symptom relapses. It is known that an early initiation of antipsychotic medications results in a better long-term outcome because the environment affects patient. This is why the early diagnosis of schizophrenia is desired. Quantifying a pathosis allows early diagnosis and appropriate treatment during episodes.

Chapter 3

Fiber tracking for schizophrenia

The fiber tracking for the quantitative evaluation of schizophrenia with manual setting of the region of interest is described in this chapter. We assume that the measurements during the fiber tracking along the targeted bundle clarify the abnormality of the white matter in the schizophrenia. The features of nerve bundles are considered to be well extracted, by not the voxel based analysis but the streamline based analysis on the tracked fibers. We obtain the magnetic resonance diffusion tensor images of schizophrenic patients and normal comparison subjects. Then we perform the fiber tracking on the targeted nerve bundles using the images. The statistical analysis with the indices representing the features of tracked fibers is performed to evaluate the abnormality of the white matter of patients leading to the group effect and the hemisphere effect. The results suggest that we may evaluate the disruption in white matter integrity in schizophrenic patients quantitatively.

3.1 Subjects

A total of 35 subjects were scanned: 14 schizophrenic patients (mean age and standard deviation of 35.0 ± 10.0 years, 7 males, 7 females, 13 right-handed, and 1 left-handed) who met the DSM-IV-TR criteria for schizophrenia and were patients attending at or entering Kyorin University Hospital and 21 normal comparison subjects (mean age and standard deviation of 31.7 ± 7.6, 12 males, 9 females, 21 right-handed). There were no significant differences in age, gender, or handedness between the schizophrenic patients and the comparison subjects. All the subjects gave written informed consent to participate in this study after receiving a full explanation of the procedures. The exclusion criteria for all the subjects included a history of convulsive disease, head injury, and a history of alcohol or substance dependence. In addition, the following were excluded as study subjects: those with diabetes and hypertension, those who had undergone electroconvulsive therapy, and those whose MRI brain scans already showed clear abnormalities. Prior to implementing

this study, we obtained the approval of the Ethics Committee of the Kyorin University School of Medicine.

3.2 Image acquisition

DTI data were obtained by use of a 1.5 T Intera Achieva Nova Dual (Philips Electronics) located at the Medical Satellite Yaesu Clinic. We used the spin echo pulse sequence with a fat suppression technique applying the EPI technique for the segmented k-space variant. The imaging matrix was 256 × 256, with a field of view (FOV) of 240 × 240 mm. The image orientation was axial, with a 5.0 mm slice thickness. We mention 'axial' in the next section. A total of 25–30 slices covered the entire cerebral hemispheres, with no gap. A voxel size was 0.9375 × 0.9375 × 5.0 mm^3. The repetition time (TR) was 2900 ms, the echo time (TE) was 60 ms, and the number of excitations (NEX) was six. The diffusion weighting was encoded along six non-collinear orientations of the motion probing gradient (MPG) ($[0.3333, 0.6666, -0.6666]$, $[0.6666, 0.3333, 0.6666]$, $[-0.6666, 0.6666, 0.3333]$, $[0.7071, 0.7071, 0]$, $[0, 0.7071, 0.7071]$, $[-0.7071, 0, 0.7071]$), with $b = 1000 \mathrm{s/mm^2}$. Additional image with $b = 0$ $\mathrm{s/mm^2}$, which is called the $b0$ image is also acquired.

3.3 Image processing

The obtained images are stored in dicom format with slice by slice and the multiple directions of MPG separately. In other words, each image file has only a single axial slice observed from the inferior side with each direction of MPG. For a definition of anatomical directions in a human body, an axial plane divides the body into cranial and caudal portions perpendicular to the z axis from the inferior side to the superior side, a sagittal plane divides the body into left and right portions perpendicular to the x axis from right side to left side, and a coronal plane divides the body into dorsal and ventral portions perpendicular to the y axis from the posterior side to the anterior side. The frame of reference is represented as in a left-hand system with setting the x, y and z coordinates as stated above.

A signal intensity described as Equation (2.25) in each voxel is preserved with an integer in a dicom image. Since all images have the same matrix size and the field of view, signal intensities of a voxel at the same place in multiple images acquired from the same slice are considered the signals from the same place. We calculate the diffusion tensor in each voxel using the set of 7 image files for a single slice, which they include a $b0$ image without MPG and six diffusion weighted images by Equation (2.38).

We show the examples of dicom images for MR-DTI in Figure 3.1. Each image is

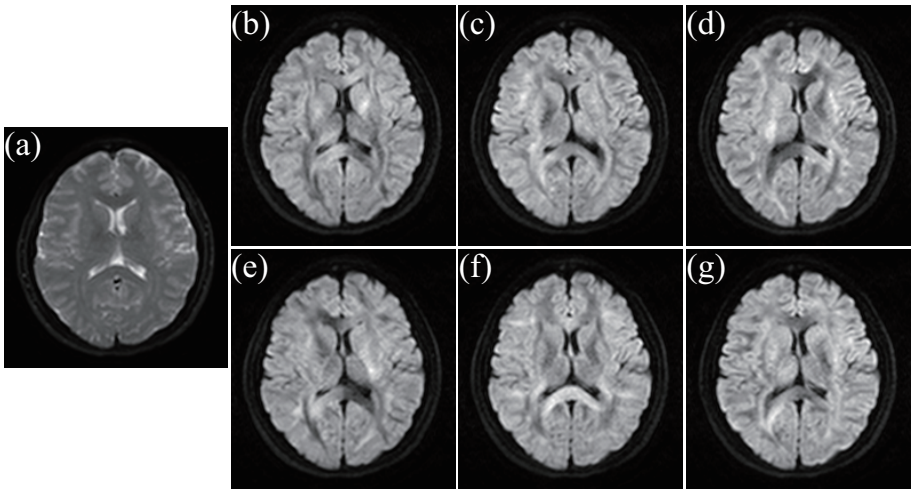

Figure 3.1: (a) The dicom image of the $b0$ image seen from the inferior side. (b)-(g) The diffusion weighted images encoded along six non-collinear orientations of the motion probing gradient. ($z = 14$)

the fourteenth axial image in 25 slices from the inferior side to the superior side of the brain. All images are the view from the inferior side, which is the common orientation for the depiction of MRI images. The images are seem as gray scaled images, since each voxel has a single value of the signal intensity. Figure 3.1 (a) represents the $b0$ image, and the others indicate the diffusion weighted images. The diffusion weighted images are collected in the same order as the orientations of MPG in the previous section. We can see the different contrast in a single slice for each diffusion weighted image. The $b0$ image is corresponding to T_2-weighted image in Section 2.1. The diffusion tensor is constructed with these seven images in a single slice.

Using the value of the diffusion tensor in each voxel, we calculate the eigenvalues and the first eigenvector corresponding to the largest eigenvalue. In addition, the FA value and the MD value are also calculated in each voxel by Equations (2.40) and (2.39), respectively. We show the example of those images in Figure 3.2. All images represent the same axial slice to the image in Figure 3.1 for the same subject. Figure 3.2 (a) indicates the FA image, which clarifies the contrast associated principally with the white matter and the gray matter. In the FA image, a white matter has a large intensity. We can recognize the contrast given mainly by the cerebrospinal fluid and the other tissues in the MD image of Figure 3.2 (b). In the MD image, the cerebral ventricle is seem to be bright, since the cerebral ventricle is mostly composed of the cerebrospinal fluid. Figure 3.2 (c), (d), and (e) represent the values of the first eigenvector along the x, y, and z axes, respectively. The component of the first eigenvector has both of a negative and positive value. Therefore we also show the images representing absolute values of the

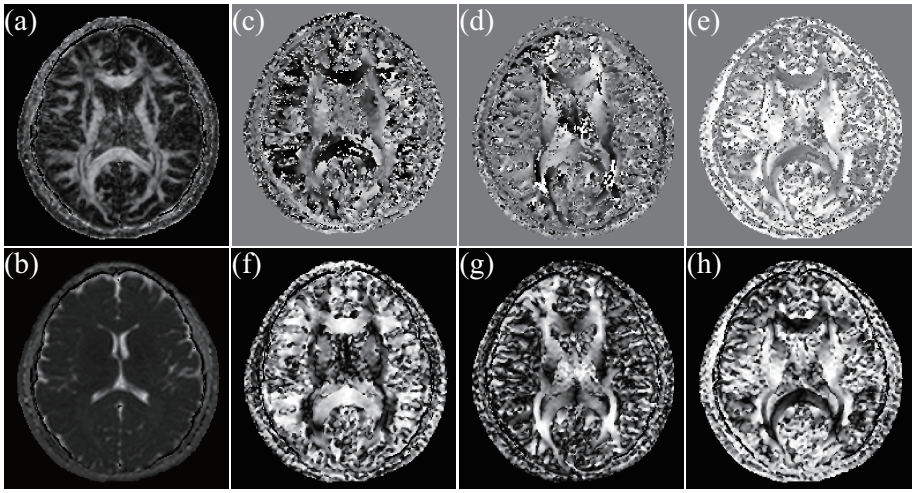

Figure 3.2: (a) The FA image. (b) The MD image. The images (c), (d), and (e) represent the components of the first eigenvector along the x, y, and z axes, respectively. (f)-(h) The images representing absolute values of the first eigenvector. ($z = 14$)

components of the first eigenvector in Figure 3.2 (f), (g), and (h). In Figure 3.2 (f) of the x component of the first eigenvector, white matters lying in the x direction such as commissural fibers are shown brightly. The association fibers along the y axis have large intensities in the image (g) of the y component. We see the bright parts of the projection fiber along the z axis in the z component image (h). Then we construct the calculated values as three dimensional data in keeping with the actual direction of the subject's brain. All calculations are performed in MATLAB for Windows (Version 7.6.0.324) and the calculated values are stored in '.m' format for MATLAB.

Furthermore, for the selection of the region of interest we prepare the data set for the color map as mentioned in Section 2.3 in Chapter 2. The x, y and z directions in this study conventionally correspond to the red, green and blue colors, respectively. The absolute values of the x, y and z components of the first eigenvector of the diffusion tensor multiplied by the FA value in each voxel are converted to the integers according to the 256-grade system from 0 to 255. The x, y and z components and the FA value are resampled at a voxel size of $1 \times 1 \times 1$ mm^3 by interpolating according to the volume data among the center points of the nearest eight voxels around the resampled point. In Figure 3.3, the value of A at (x_n, y_n, z_n) is interpolated by Equation (3.1). The coordinates of the eight points around the point (x_n, y_n, z_n) represent the coordinates of the centers of the voxels with an imaging matrix $256 \times 256 \times 25$. The interpolation according to the volume data is described by the total of the multiplication of the value at each corner by the volume of the opposite angle (for instance, the value at (x_m, y_m, z_m) with red color in Figure 3.3 and the light pink colored volume).

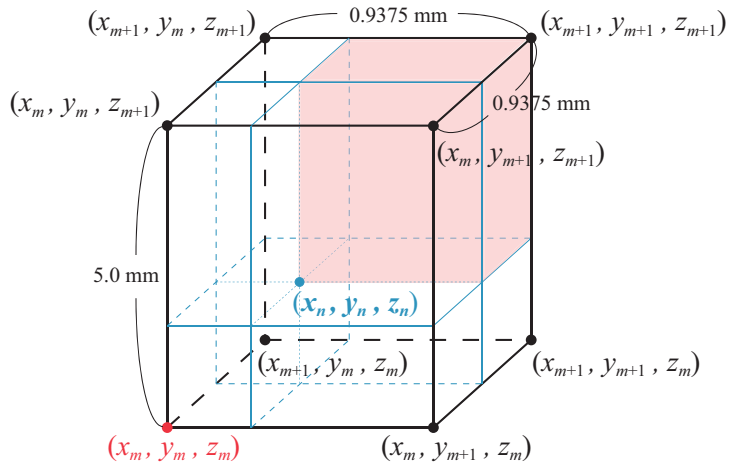

Figure 3.3: The interpolation according to the volume data among the center points of the nearest eight voxels with the imaging matrix.

$$
\begin{aligned}
A(x_n, y_n, z_n) = \quad & A(x_m, y_m, z_m) \times (x_{m+1} - x_n)(y_{m+1} - y_n)(z_{m+1} - z_n) \\
& + A(x_{m+1}, y_m, z_m) \times (x_m - x_n)(y_{m+1} - y_n)(z_{m+1} - z_n) \\
& + A(x_m, y_{m+1}, z_m) \times (x_{m+1} - x_n)(y_m - y_n)(z_{m+1} - z_n) \\
& + A(x_m, y_m, z_{m+1}) \times (x_{m+1} - x_n)(y_{m+1} - y_n)(z_m - z_n) \\
& + A(x_{m+1}, y_{m+1}, z_m) \times (x_m - x_n)(y_m - y_n)(z_{m+1} - z_n) \\
& + A(x_m, y_{m+1}, z_{m+1}) \times (x_{m+1} - x_n)(y_m - y_n)(z_m - z_n) \\
& + A(x_{m+1}, y_m, z_{m+1}) \times (x_m - x_n)(y_{m+1} - y_n)(z_m - z_n) \\
& + A(x_{m+1}, y_{m+1}, z_{m+1}) \times (x_m - x_n)(y_m - y_n)(z_m - z_n) \, . \qquad (3.1)
\end{aligned}
$$

In addition, the degree of transparency 'alpha' which is also according to the 256-grade system from 0 to 255 is designated as 255 which corresponds to complete opacity. A data set including the x, y and z components and the degree of transparency is put together to one four dimensional volume data resulting RGBA color model in raw data format in order to display the data as a color map in VOLUME-ONE software. This software is provided by the VOLUME-ONE developer group and available on the Internet (Version 1.72, http://volume-one.org/index-j.htm) for the OS of Windows. After we initiate the executable file of VOLUME-ONE, a raw image is loaded from 'Open' in 'File' function. In Figure 3.4, we show two screens arising when we load an image. In the left screen, we select the image that is depicted. First we choose the directory in the left window, and find the image in the right window. Second we assign the matrix size shown in the right screen. Since the matrix size of data set is $4 \times 240 \times 240 \times 125$ with RGBA representation, we

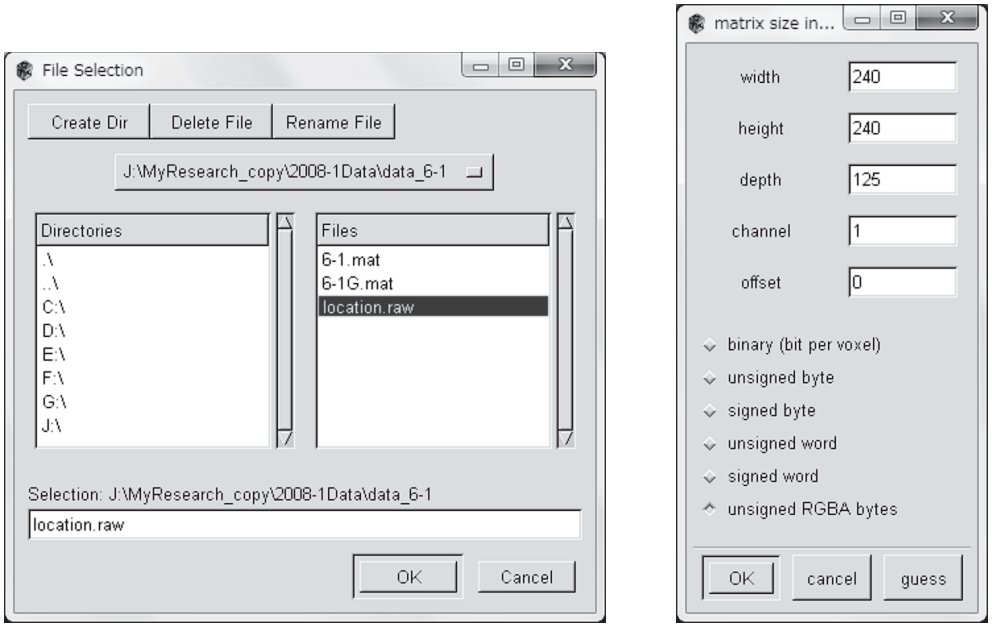

Figure 3.4: The pop-up screens arising when an image is loaded into VOLUME-ONE. In the left screen the image file is selected, and we assign the matrix size in the right screen.

view the color map image with some setting; 'width' of 240, 'height' of 240, 'depth' of 125, 'channel' of 1, 'offset' of 0 and 'unsigned RGBA bytes' in VOLUME-ONE.

The loaded image is displayed as Figure 3.5. The axial, sagittal, and coronal slices are visualized in the upper, middle, and lower left windows, respectively. Note that the orientation of the slice's aspect depicted in this software and the definition of the x, y, and z axes are different from the other images in this dissertation. We see the axial image from the superior side of the brain; i.e. the upper side of this axial image represents the right side of the brain. The coronal image is the slice seen from the posterior side of the brain. The x, y, and z axes in VOLUME-ONE software are corresponding to the y, x, and z axes in the other parts of this dissertation. The coordinate system is also the left-handed system. The red lines indicate the location of each slice. We can change slices by a mouse click on the image of slices or a 'Jump to' function in 'Tools' function group numerically. When we change slices, the coordinates and the values of RGBA at the voxel, where the slices are crossing each other, are checked in the lowest bar of the screen. In the right window in Figure 3.5, we can confirm the three-dimensionally constructed image with selected slices. The image is rotated by double clicks and dragging. With a right click of a mouse and dragging, the three-dimensional image perform parallel displacement. The direction of the three-dimensional image is also changed by a 'View' function. However, note that the transcribed direction is different from that of the visualized image due to the incoherence of the axis orientations; 'Front' in this software is seen from the right

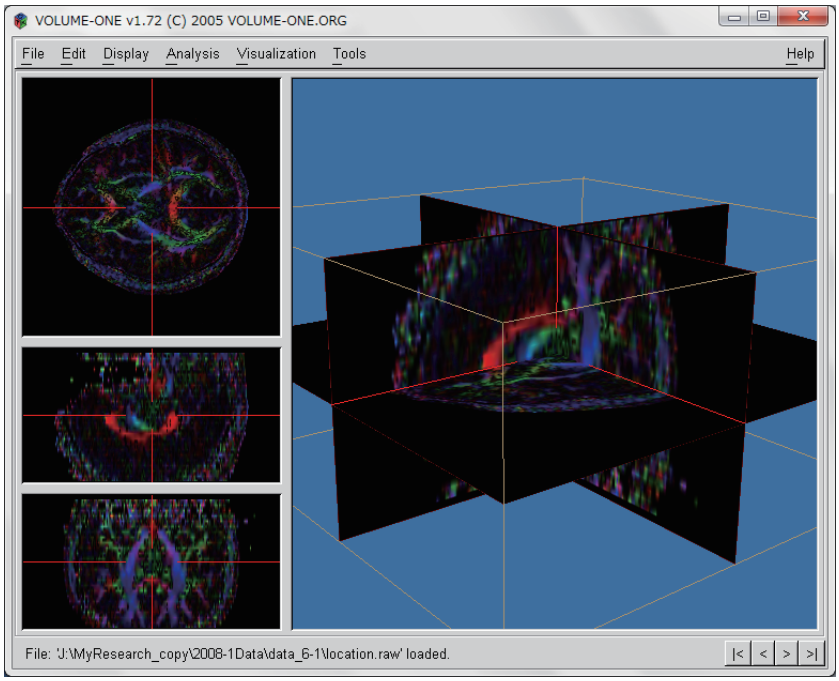

Figure 3.5: The operation screen of VOLUME-ONE. The axial, sagittal, and coronal images are placed in the left column, and the three-dimensional image composed of the selected slices is represented in the right window.

side of the brain, 'Back' is from the left side, 'Left' is from the posterior side, 'Right' is from the anterior side, 'Top' is from the inferior side, and 'Bottom' is from the superior side. We can control the visibility of slices, a bounding box, and cursors by a 'Visibility' function in the 'Visualization' function group.

Figure 3.6 shows examples of color maps. We changed the orientation of these images from the original direction in VOLUME-ONE corresponding to the commonly used orientation of MRI images, in order to establish consistency with the other depicted images. The axial image (a) is almost same slice to the images in Figure 3.2. It is not just the same slice, since the matrix size is different from the previous images. The prominent parts represented with reddish colors in the anterior and the posterior sides around the median line are the genu and splenium of the corpus callosum. The remarkable inside bluish areas indicate the internal capsules, and the outside bluish areas describe the external capsules for the bilateral hemispheres. In addition, the greenish parts in the anterior division show the anterior corona radiata, and the posterior greenish areas indicate the posterior thalamic radiation including the optic radiation. The sagittal image (b) on the midline is seen from the left side of subject's brain. The remarkable red area in the center position represents the corpus callosum. We can see the fornix with bluish colors under the corpus callosum. In the coronal image (c), the superior corona radiata and the pos-

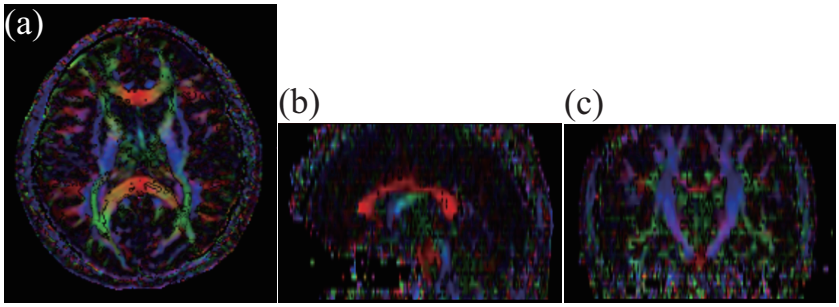

Figure 3.6: (a) The axial image of a color map. ($z = 70$) (b) The sagittal image on the midline. ($x = 121$) (c) The coronal image around the center of the brain. ($y = 121$)

terior limb of internal capsule are seen distinguishing bluish parts. This sagittal image is the slice looked from the anterior side of the brain, which is the usual direction when we show the MRI images. The greenish part surrounded by the bluish areas is mainly composed of the thalamus. The superior greenish areas outside the bluish areas represent the superior longitudinal fasciculi, and the inferior greenish parts outside the bluish circle include the association bundles such as the inferior longitudinal fasciculus and the inferior front-occipital fasciculus.

3.4 Region of interest (ROI)

We define the starting and ending areas for the fiber tracking on two coronal planes, assuming the tracking of the association fiber, which connects the areas in a single hemisphere and goes mainly to the anteroposterior orientation. The starting and ending areas for the fiber tracking are called the region of interest (ROI) in this study. The tracking area is a sandwiched area by two coronal planes. We establish the starting area on the posterior plane, and the ending region on the anterior plane. Since the association fiber lies on bilateral hemispheres separately, ROI for the right and left hemispheres are prepared separately.

The position of ROI for the fiber tracking is selected visually on the color map displayed in VOLUME-ONE and designated with an integer in the matrix with the 1 mm cubed voxel. In Figure 3.7 we show the procedure for the selection of the location and area of ROI. The 'selection' function is initiated from the 'Tools' function group. The light yellow rectangle is appeared on the images, when we assign a location and a width of the area numerically, which we want to select as a starting or an ending region. We can change the location and the area per 1 mm in the image. Note that the direction of x, y, and z axes are different from the definition of those in the case without VOLUME-ONE. The relation of the orientations between those in VOLUME-ONE and those in the case

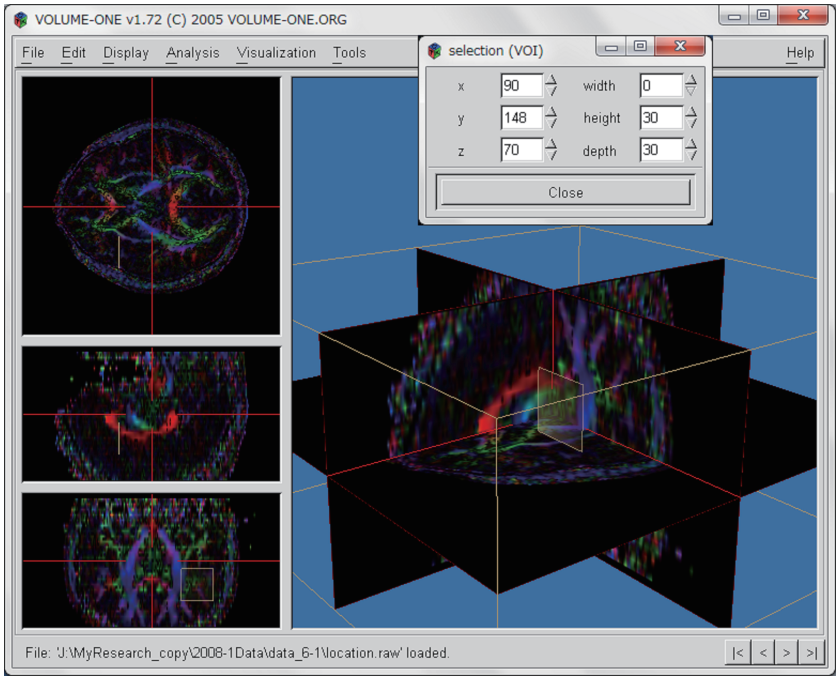

Figure 3.7: The selection of ROI on the color map visualized in VOLUME-ONE.

without VOLUME-ONE is mentioned above.

3.4.1 Superior longitudinal fasciculus

First, we target the superior longitudinal fasciculus, which is an association fiber that connects the frontal lobe, temporal lobe, parietal lobe, and occipital lobe. The superior longitudinal fasciculus becomes aligned around the center of the cerebral cortex, whereas it expands in the vicinities of the frontal and occipital lobes. In the present study, we target the fasciculus around the center of the cerebral cortex for more accurate tracking.

Uniquely specified ROI

The starting and ending regions are defined on a single coronal plane severally with square areas. The right and left regions in the same coronal section are prepared separately. They are set based on the corpus callosum to exclude individual differences due to different volumes of the cerebral cortex. The corpus callosum is the largest commissural fiber in the cerebrum. Since it runs along the direction of the x axis around the center of the brain, it is described by warm reddish colors in a color map.

As for setting the ROI in the targeted nerve bundle, we first select the sagittal plane including the midline (Figure 3.8(a)) on the axial plane where we find the splenium of the corpus callosum. In this sagittal plane (Figure 3.9), we identify the coronal planes

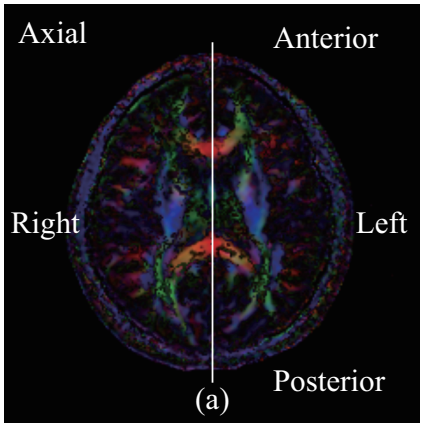

Figure 3.8: The selection of the sagittal plane, which includes the midline of the brain.

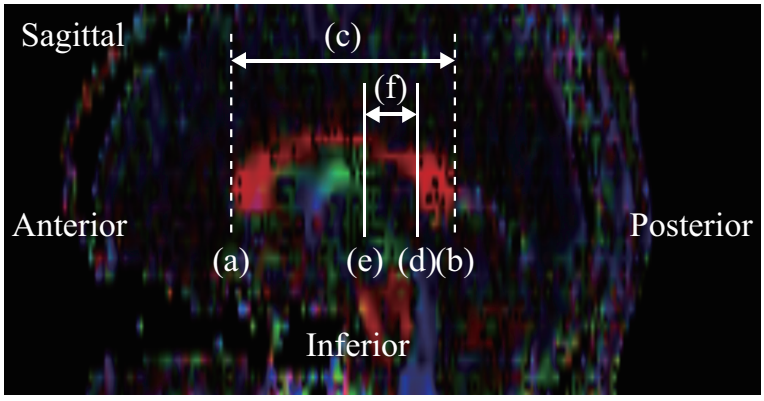

Figure 3.9: The starting and ending coronal planes are selected in the sagittal plane for the fiber tracking of the superior longitudinal fasciculus. The edges of the corpus callosum are identified on the midline. We establish the starting and ending planes based on the position of the corpus callosum.

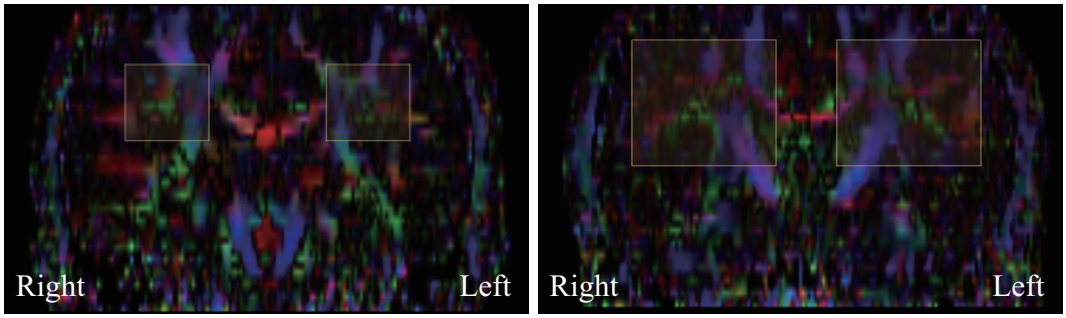

(a) (b)

Figure 3.10: The starting and ending areas are selected with square shape on the coronal planes when we track the superior longitudinal fasciculus. (a)The starting areas on the coronal plane (d) in Figure 3.9. (b)The ending areas on the plane (e) in Figure 3.9.

including the anterior edge (a) and the posterior edge (b) of the corpus callosum. The width of the corpus callosum is represented in (c). We also identify the anterior edge of the splenium of the corpus callosum (d) and establish this coronal plane as the starting plane for fiber tracking. In addition, we establish the coronal plane (e), which is located in 40 % of the width (c) ahead of the posterior edge of the corpus callosum (b), as the ending plane. The region (f) signifies the anteroposterior region of the ROI in this study. The position and anteroposterior length of the ROI were determined by the trial and error method.

On the starting and ending coronal planes, the areas for the fiber tracking are defined in square shape. The light yellow areas in Figure 3.10(a) and (b) represent the starting and ending areas, respectively. The greenish deltoid areas in the starting areas represent the target tracts, since the superior longitudinal fasciculus runs along the direction of the y axis around the target area.

The other association fibers such as the cingulate fasciculus also run in the vicinity of the ROI. The cingulate fasciculus runs almost parallel to the superior longitudinal fasciculus, and approaches the midline compared to the superior longitudinal fasciculus. If untargeted bundles are tracked concurrently with the targeted bundle, and they are apart from the targeted bundle, we cannot obtain precise indices characterizing the targeted bundle. Not to include the other fasciculus, we adjust the starting or ending regions by reducing or shifting the areas in the same coronal plane. After we track fibers with the original ROI, we judge if some untargeted bundles are included in the tractography visually, and exclude the untargeted fibers. We describe the method of the fiber tracking in the next section.

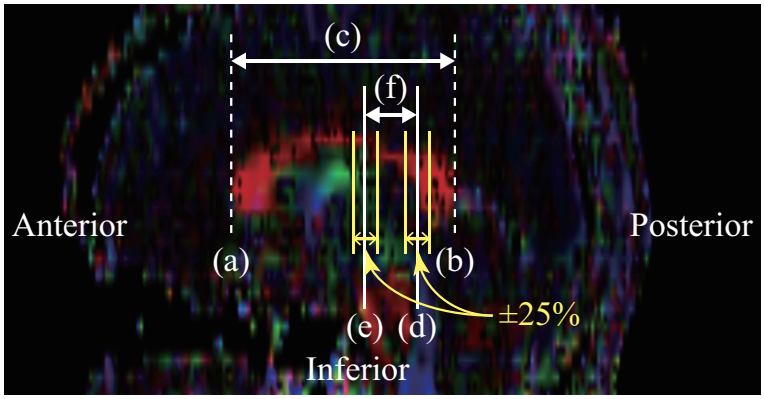

Figure 3.11: The individual ROI for the tracking of the superior longitudinal fasciculus is selected by changing the starting and ending planes in anteroposterior direction for 25 % of the width between the initial starting and ending planes. In the selected area, the maximum total number of fibers in the right and left hemispheres is tracked.

Specified ROI based on the bilateral fibers

The initial starting and ending coronal planes are determined in the same way as the case of the uniquely specified ROI. We choose individual ROI by changing the starting and ending regions around the initial area, to deal with individual differences of the position of nerve bundles and slight rotation of the head in acquiring images. The distance between the starting and ending planes is kept in the same width between the initial planes. The starting and ending coronal planes are changed in conjunction anteroposterior up to 25 % of the width between the initial starting and ending planes (Figure 3.11). The length of 25 % of the width corresponds to about 4 mm in the actual brain. The range of the changing was established through trial and error. Fiber tracking is performed in the region between each starting and ending planes. Then, we select the starting and ending regions where the maximum total number of fibers in the right and left hemispheres is tracked. In this case we also exclude the untargeted fibers by changing the square measures or positions in the coronal plane.

3.4.2 Inferior longitudinal and inferior fronto-occipital fasciculi

The present study also targets the inferior longitudinal fasciculus and the inferior fronto-occipital fasciculus, both of which are representative association fibers. The inferior longitudinal fasciculus connects the temporal lobe and occipital lobe, goes through outside of inferior and dorsal horn of the lateral ventricle. The inferior fronto-occipital fasciculus connects the frontal lobe and occipital lobe, passes through ventrolateral edge of the lenticular nucleus. These two nerve bundles also become aligned around the center of the cerebral cortex, whereas they expand near the frontal lobe and occipital lobe. We

target the part of those fasciculi, which spreads toward a little more backward position compared to the ROI in the case of the superior longitudinal fasciculus. The fasciculi gather densely in this area.

Specified ROI based on the unilateral fibers

The initial starting and ending planes, which are the same planes for the fiber tracking of the two targeted bundles, are set based on the corpus callosum. The ROI areas for the two bundles are prepared separately.

As for setting the regions of interest in the target nerve bundles, we identify the sagittal plane on the midline, the anterior and posterior edges of the corpus callosum on the sagittal plane (Figure 3.12 (a) and (b)), and the anterior edge of the splenium of the corpus callosum (d) in the same way as the case of the superior longitudinal fasciculus.

After that, we establish the coronal plane (Figure 3.12 (e)) that includes the center of splenium of the corpus callosum as the initial starting plane for fiber tracking. In addition, we configure the initial ending plane on the plane (f) 40 % ahead of the diameter of the corpus callosum (c) from the initial starting plane. The degree of the length of the ROI was defined through trial and error. In Figure 3.12, region (g) represents the initial ROI.

In order to set the individual ROI, we select the starting and ending regions where the maximum number of streamlines in each hemispheres are tracked, when changing the regions simultaneously anteroposterior up to 5 % of the length of the corpus callosum (Figure 3.12 (c)) in each subject. We used the length of the corpus callosum as the reference value of the anteroposterior changing, since the ratio of the difference in the length of the reference value among individuals compared to the case when we applied the distance between the starting and ending planes as the reference value. The length of the corpus callosum is always longer than the distance between the starting and ending planes. We can define the coordinates of the starting and ending regions in integers. When we round the coordinate off to an integer, the rounded value in one decimal place often takes a relatively large value, if the short length is referenced. The rate of the changing was established by the trial and error method. The length of 5 % also corresponds to around 4 mm in the brain of the subjects. In addition, we determine ROI based on the number of the tracked fibers in each hemispheres differently from the case in the superior longitudinal fasciculus. The inferior longitudinal and inferior fronto-occipital fasciculi have relatively thin shapes compared to the superior longitudinal fasciculus. If we apply the maximum total number in the both of hemispheres, ROI cannot be selected properly to obtain the features of tracked fasciculi, when more fibers are tracked in only a single hemisphere.

We construct areas of ROI for the inferior longitudinal and inferior fronto-occipital fasciculi separately with rectangles. The two bundles lie adjacently each other around the

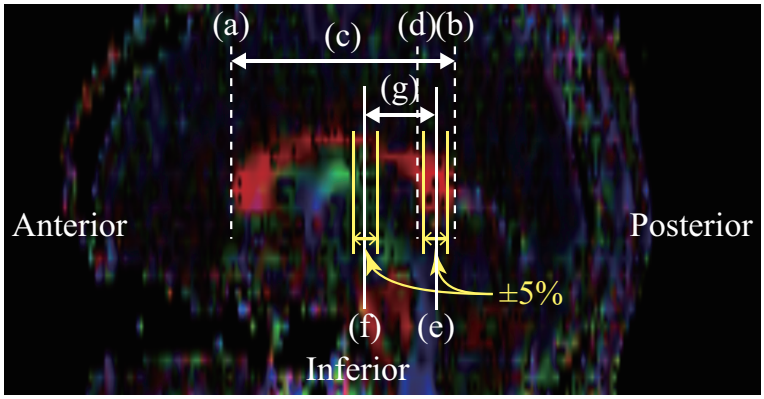

Figure 3.12: The individual ROI for the tracking of the inferior longitudinal and inferior fronto-occipital fasciculi is selected by changing the starting and ending planes in antero-posterior direction for 5 % of the length between the anterior and posterior edges of the corpus callosum. In the selected area, the maximum number of fibers in each hemispheres is tracked.

starting region. After the fiber tracking with relatively wide areas of ROI was performed, we determined ROI visually for the two bundles, not to contain the other bundle. If the other bundle is included in the tractography, we change the areas or positions of ROIs.

3.5 Performing of the fiber tracking

We use the streamline tracking method (STT) to determine the direction of tracking and the Runge-Kutta method of the fourth order (RK4) to propagate to the next stepping point, which are mentioned in Section 2.4. We perform the fiber tracking in MATLAB using the data set containing the three-dimensional data of FA, MD and the first eigenvector.

The diffusion tensor at a stepping point is decided by interpolation using the volume and the diffusional tensor data of the eight points around the stepping point. We described the interpolating method in Section 3.3. The interpolation is performed during the Runge-Kutta method.

The stepping width h is the constant value of 0.5 mm, which is short enough experimentally for the accurate tracking in this study. Although we can save time during the fiber tracking if more long width is adapted, the adequate information of the tensors to evaluate the targeted bundles cannot be reflected in the tracked streamlines when too long width is adapted.

The points to start the fiber tracking are dispersed evenly in the starting areas at a rate of 4 points/mm^2; i.e., each seed point has a cross-sectional area of 0.25 mm^2. We start the fiber tracking from each seed point assuming that a fiber is tracked from the outside

of ROI along the y axis. The direction for or against the first eigenvector of the diffusion tensor at a seed point is selected based on the assumed orientation of the tracking to the seed point.

In order to display the tractography of tracked fibers, we create the three-dimensional data including the tracked fibers, the FA image on the starting coronal plane with the alpha of about 20 % transparency, and the guiding axial plane in the matrix of 240 $\times$ 240 $\times$ 125 in a raw format. The value of the alpha indicates the degree of transparency of an image. For rendering the fibers, the voxels on the streamline are colorized with RGB according to the direction of the streamline. The axis of the coloring follows a low of the color map.

3.6 Terminal criteria

Fiber tracking is completed when the streamline goes through the ending region, if the fiber is tracked continuously without any termination during the tracking. In order to exclude the tracked streamlines, which seem to run off the accurate tracked fibers, we establish some terminal criteria of the tracking.

The FA value at the present stepping point is calculated via interpolation using the volume data for the center points of the nearest eight voxels around the stepping point. The fiber tracking is terminated at a point with FA of less than 0.25 because FA decreases in areas where the nerve fibers are not well-ordered and the tracking is considered to move away from the targeted nerve bundles. This threshold is commonly used in previous studies [58, 30]. The degree of FA has a large value in the area where nerve fibers exist and especially lie in tight formation. It is often said that FA is more than 0.25 in the white matter including the fiber tract in the human brain and FA is less than 0.25 in the gray matter and cerebrospinal fluid.

The tracking is also terminated when the deflected angle is greater than 45° so as to except a large angular shift because the targeted bundles has a relatively linear shape. The deflected angle is the angle between the two stepping directions of the continuous steps. We determine this threshold originally, since the axons in the targeted bundles are not considered to curve quickly. In the actual tracking, almost all deflected angles are much smaller than 45°, when the tracking is performed on only the targeted bundles successfully. The deflected angle markedly increases around the point where the tracking runs off the original fiber. Since the deflected angle sometimes has a slightly large value on the assumed bundles, we apply the angle of 45° for the additional coverage.

In order to identify and erase erroneously tracked streamlines, we select the extracted streamline with the shortest length, and employ that length as the baseline length of the tracked streamline. The baseline length is determined separately for the right and left

hemispheres. Any streamline measurements with a length exceeding 105 % for the superior longitudinal fasciculus or 110 % for the inferior longitudinal and inferior fronto-occipital fasciculi of the base length are judged to have an erroneous tracking result and are thus eliminated from the streamline group. The superior longitudinal fasciculus adjoin the arcuate fasciculus, which go toward the inferior direction in the anterior region [59]. Since we target the central part of the superior longitudinal fasciculus for the fiber tracking and the evaluation, we determine the strict permissible range for the fasciculus. On the other hand, we establish the relatively tolerant acceptable limits, since the inferior longitudinal and fronto-occipital fasciculi are independent of the other bundle in the targeted areas. We determined these thresholds originally by trial and error method to exclude the streamlines, which were assumed to be turned out from the targeted bundle. As for the setting of this threshold, we paid attention not to eliminate the streamlines on the targeted bundles.

3.7 Statistics

In order to analyze the features of the tracked fibers statistically, we calculate five evaluation indices. Each index is defined separately in the right and left hemispheres in a individual. We perform the statistical analysis for all indices to compare the values between the right and left hemispheres, and between the schizophrenic patients and the comparison subjects. The statistical analysis by a t-test (significance level of $P < 0.05$) is carried out for comparison between the subject groups and between the hemispheres separately, after the analysis by two-way repeated-measured analysis of variance (ANOVA) [60] for comparison with two factors; the hemispheres as the within-subjects factor and the groups as the between-group factor. We performed the statistical analysis with SPSS.

As an evaluation index, the cross-sectional area of the neuronal tract in the starting region represented by S is calculated. S is defined as 0.25 mm^2 multiplied by the number of tracked fibers until the ending region without termination or elimination. The size of 0.25 mm^2 indicates the area of a single seed point.

The value of FA and MD are calculated for each stepping point by the interpolation based on the volume and the central value of the nearest voxels. The mean and standard deviation of FA and MD for a single tracked fiber are obtained. These four indices, represented as FAM (the mean of FA), FASD (the standard deviation of FA), MDM (the mean of MD), and MDSD (the standard deviation of MD), are averaged among all tracked fibers separately for the right and left hemispheres in individual subjects.

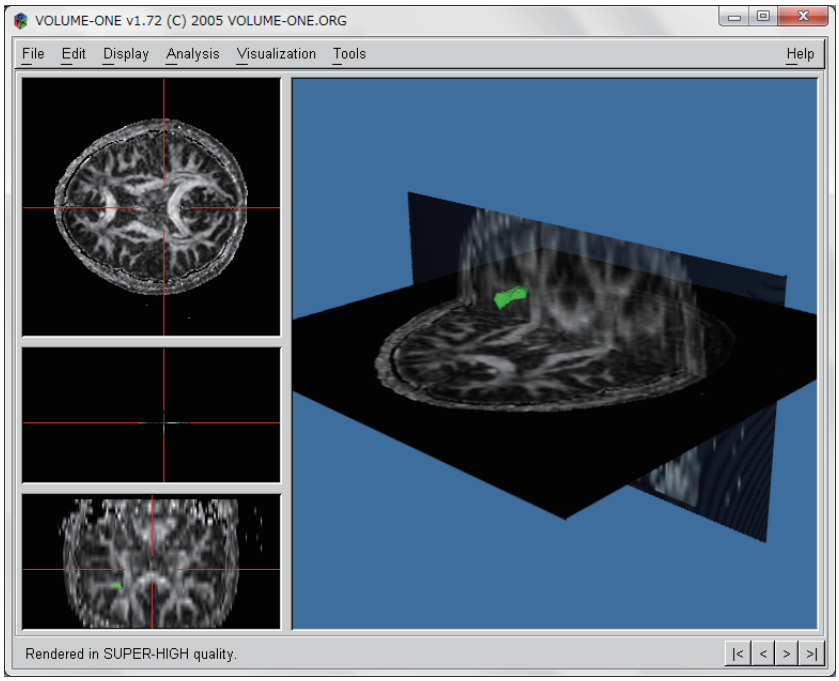

Figure 3.13: The principal screen of VOLUME-ONE, when the tracked fibers are displayed as a tractography.

3.8 Results

We provide the tractography of the tracked fibers of the representative subjects, the graphs of all evaluation indices, and the statistical results for the three fasciculi in separate subsections. The graphs express the average values with error bars of the standard deviations for each group and hemisphere.

The tractography is displayed with the FA image of the coronal plane, which indicates the starting plane of the initial starting plane. It is visualized using VOLUME-ONE. In Figure 3.13, we show the example of the visualization of the tractography. The way to load an image is the same as the case of visualization of the color map. We establish the three-dimensional imaging by the 'Alpha composite' function in the 'Visualization' function group with choosing the rendering engine of 'VOL RayCaster'. The rendering quality is set as 'super' in the 'Visualization' function group. Note that we rotate the three-dimensional image in the beginning of the visualization in order to display the processed image, after the three-dimensional construction. Since the three-dimensional visualization takes some seconds, we wait for the accomplishment after a single rotation of the image without any repetition of rotation.

In each figure of the tractography representing each result in each case, the front left side is the anterior orientation of the brain and the top is the superior direction. We can

find the greenish fibers tracked toward the front left side from the starting region along the y axis.

3.8.1 Superior longitudinal fasciculus

Uniquely specified ROI

The tractography for representative four subjects in the patient group and healthy comparison group are shown in Figure 3.14 and 3.15, respectively. Although we can not read features of tracked fibers from the tractographies numerically, we can check if the other bundles are tracked together and if the tractographies lie in proper targeted ROI with the assumed shape corresponding to anatomical knowledge. In each figure, images of (a-L), (b-L), (c-L), and (d-L) indicate the results in the left hemisphere for four individuals. The images of (a-R), (b-R), (c-R), and (d-R) represent the tractographies in the right hemisphere.

The means and standard deviations of the five evaluation indices for all subjects are shown in Figure 3.16. Black and white bars indicate the values for the patients and healthy subjects, respectively. The results in the left hemisphere are shown in the left side (L) in each graph and those of the right hemisphere are placed in the right side (R).

We performed ANOVA for all indices, and t-tests for three indices, which had a significant effect ($P < 0.05$) or a tendency of having a significant effect ($P < 0.1$) in ANOVA. The results of ANOVA (Table 3.1) show the tendency of having a significant group effect in S and the significant hemisphere effect in FAM and MDM. Especially, the strong effect was observed for hemispheres in MDM.

In the t-test for the statistical test of the mean value (Table 3.2) between the schizophrenic patient and healthy comparison groups, the patient group had significantly smaller S of the superior longitudinal fasciculus of the right hemisphere, whereas no significant difference existed in the left hemisphere. The index FAM showed no significant difference between hemispheres in both of the groups. In the t-test for comparison between the left and right hemispheres, MDM for the left hemisphere was significantly larger than that for the right in both the patient and healthy comparison groups.

The indices, which had a significant difference between groups or hemispheres in a t-test, are represented in Figure 3.16. A single asterisk indicates that the signed pair had a significant difference, with significance level $P < 0.05$. The double asterisk indicates that the significance level was $P < 0.01$.

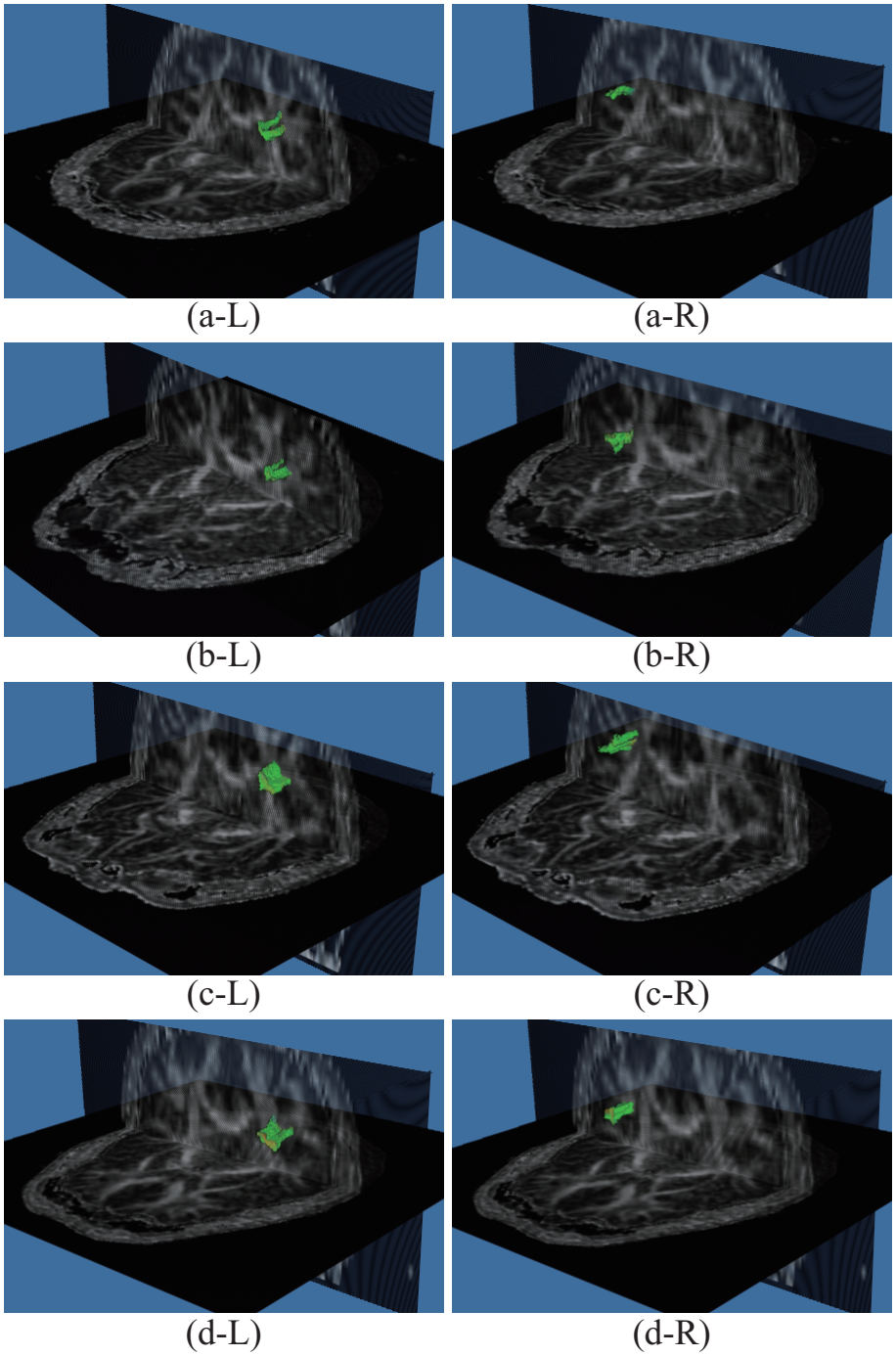

Figure 3.14: The tractography of the superior longitudinal fasciculus with the uniquely specified ROI for the patients of schizophrenia.

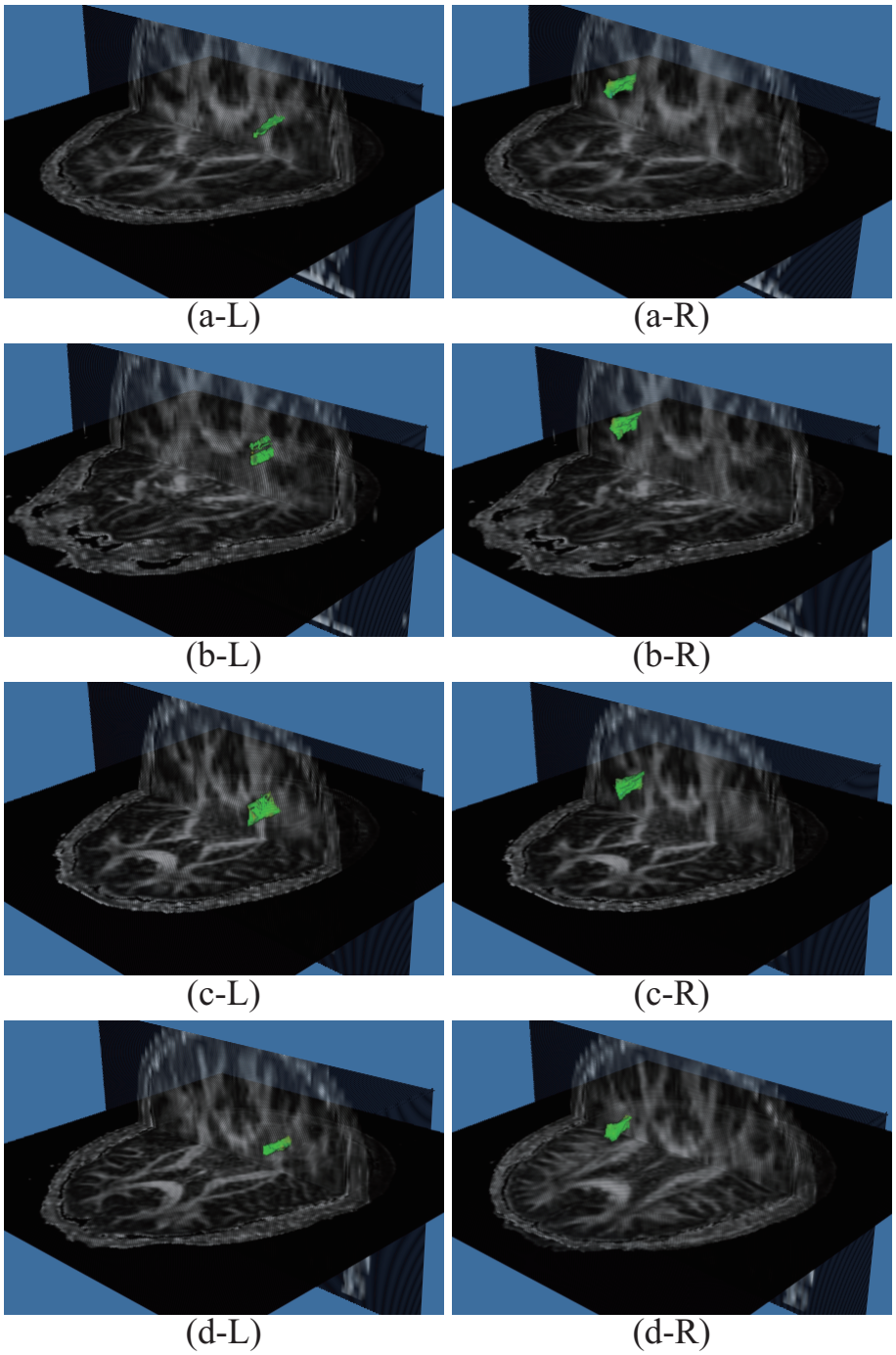

Figure 3.15: The tractography of the superior longitudinal fasciculus with the uniquely specified ROI for the healthy subjects.

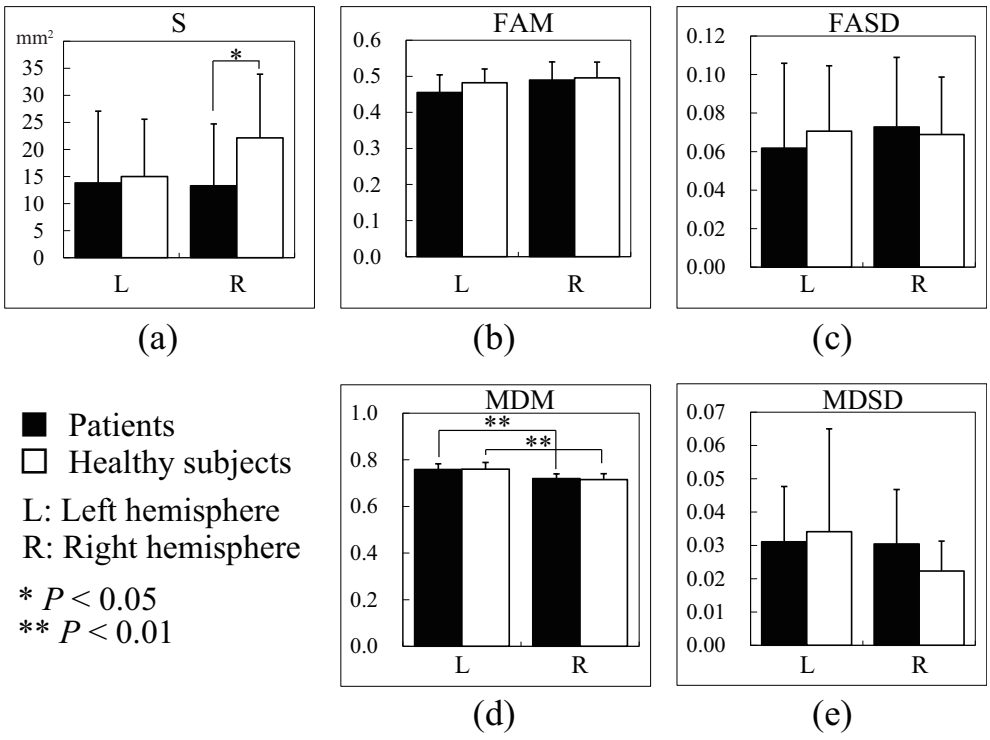

Figure 3.16: The average of five evaluation indices for the superior longitudinal fasciculus with the uniquely specified ROI. The abbreviations of L and R denote the left and right hemisphere, respectively. The patients and healthy comparison subjects are indicated by black and white bars, respectively. (a)the cross-sectional area on the starting coronal plane (S), (b)the mean of FA (FAM), (c)the standard deviation of FA (FASD), (d)the mean of MD (MDM), and (e)the standard deviation of MD (MDSD).

Table 3.1: The results of two-way repeated-measured ANOVA for comparison of all evaluation indices with group as between-group factor and hemisphere as within-subject factor for the superior longitudinal fasciculus with the uniquely specified ROI.

Two-way ANOVA						
	Group effect		Hemisphere effect		Interaction	
Indices	$F(\mathrm{df} = 1, 66)$	P Value	$F(\mathrm{df} = 1, 66)$	P Value	$F(\mathrm{df} = 1, 66)$	P Value
S	3.231	0.077	1.586	0.212	1.766	0.188
FAM	1.799	0.184	4.418	0.039	0.638	0.427
FASD	0.073	0.788	0.329	0.568	0.529	0.470
MDM	0.260	0.612	47.898	0.000	0.060	0.808
MDSD	1.409	0.239	0.865	0.356	1.106	0.297

Table 3.2: The results of the t-test separately examining three indices between patient and healthy comparison subject groups and between left and right hemispheres for the superior longitudinal fasciculus with the uniquely specified ROI.

t-test						
	Group effect (Patient - Healthy)					
	Left			Right		
Indices	t Value	df	P Value	t Value	df	P Value
S	0.332	33	0.742	2.205	33	0.035
	Hemisphere effect (Left - Right)					
	Patient			Healthy		
Indices	t Value	df	P Value	t Value	df	P Value
FAM	1.743	26	0.093	1.086	40	0.284
MDM	4.382	26	0.000	5.605	40	0.000

Specified ROI based on the bilateral fibers

The tractography for the subjects in the patient group and healthy comparison group are shown in Figure 3.17 and 3.18, respectively. The printed subjects are the same to the case of the uniquely specified ROI. For almost all of the subjects, we can see that the number of the tracked fibers increase in the comparison to the above-mentioned case.

We calculated the means and standard deviations of the five evaluation indices for all subjects in Figure 3.19. The tendency of averaged values of FAM, FASD, and MDM was similar to the values in the case of the uniquely specified ROI. The value of S except for the occasion in the left hemisphere for patients was tend to be close to that of the above result. The measurement of MDSD did not show a tendency to be akin to the value for the unique ROI.

After the statistical analysis of ANOVA for all indices was performed, t-tests were carried out for three indices. The significant effect was shown in the results of ANOVA (Table 3.3) for the interaction of S and the hemisphere effect of MDM and MDSD.

We performed t-tests (Table 3.4) between the schizophrenic patient and healthy comparison groups. We found that the patient group had significantly smaller S of the superior longitudinal fasciculus in the right hemisphere, whereas no significant difference between groups existed in the left hemisphere. Furthermore, right S increased in comparison to that of left hemisphere for the healthy comparison group. No significant difference resided in the patient group between hemispheres. In the t-test for comparison between the left and right hemispheres, MDM for the left hemisphere was significantly larger than that for the right in both the patient and healthy comparison groups. We did not observe any significant difference between hemispheres for the index MDSD in both of the groups.

The results of the t-test are represented in Figure 3.19 by a single asterisk with the

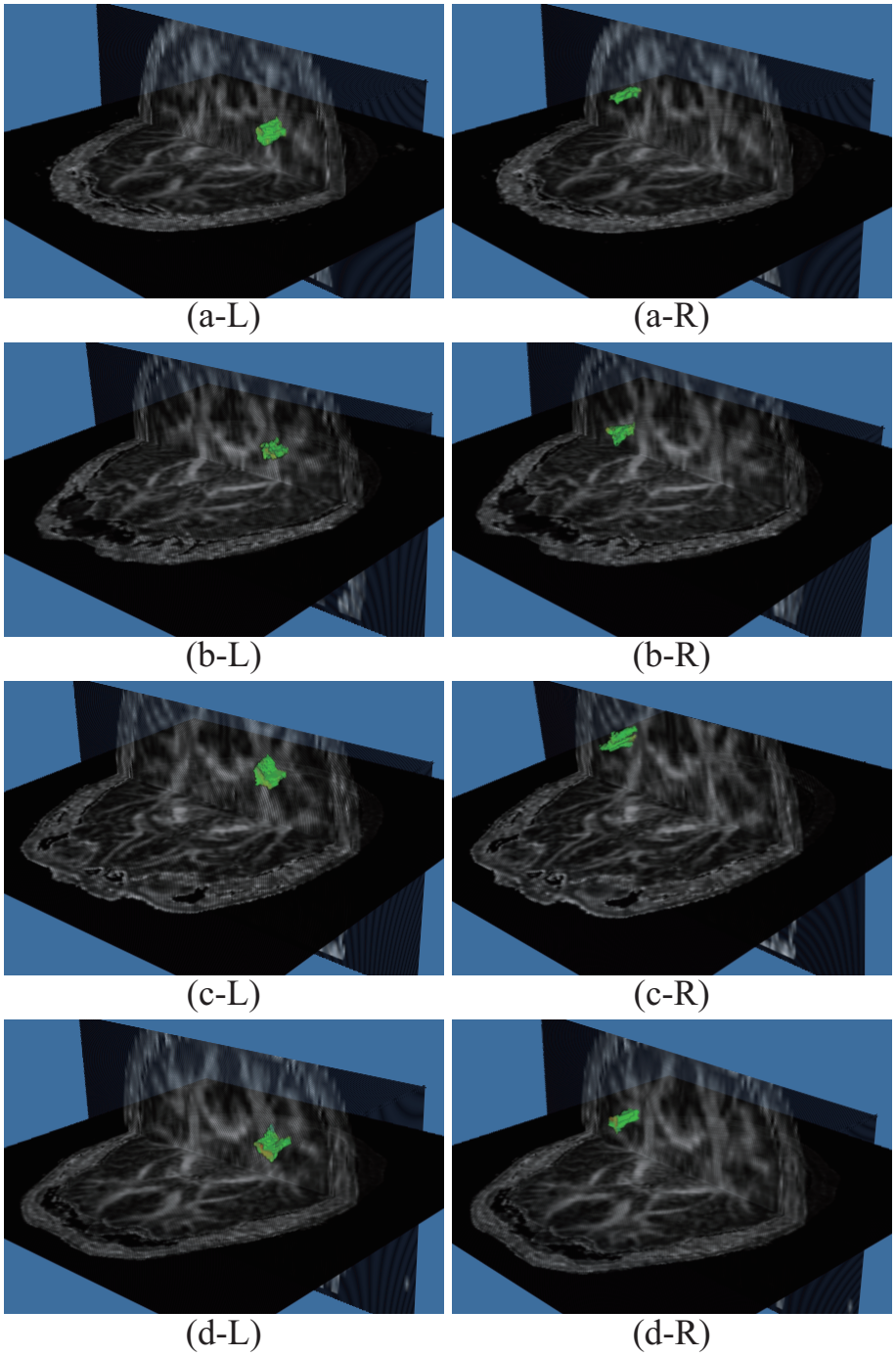

Figure 3.17: The tractography of the superior longitudinal fasciculus with the specified ROI based on the bilateral fibers for the patients of schizophrenia.

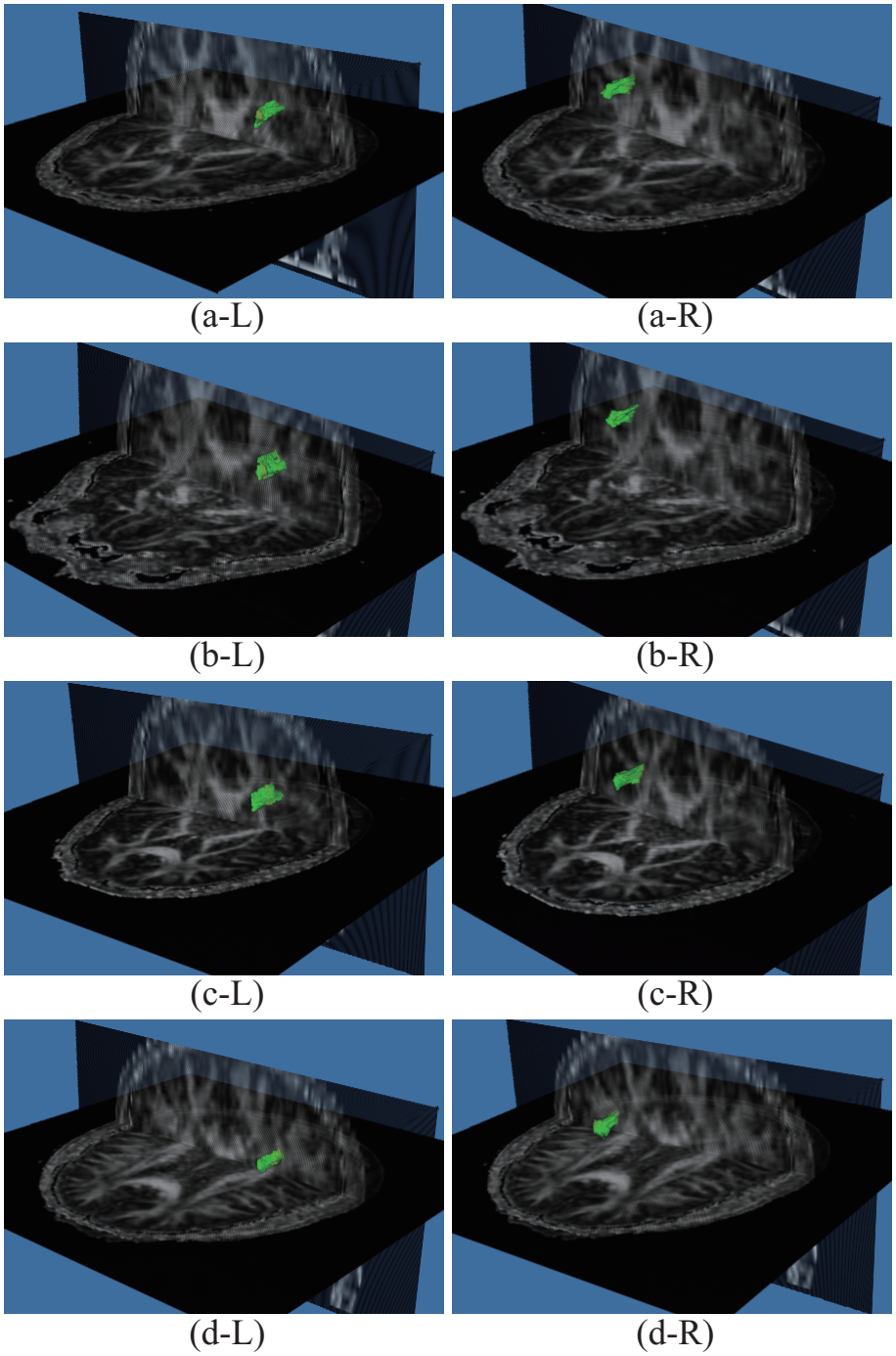

Figure 3.18: The tractography of the superior longitudinal fasciculus with the specified ROI based on the bilateral fibers for the healthy subjects.

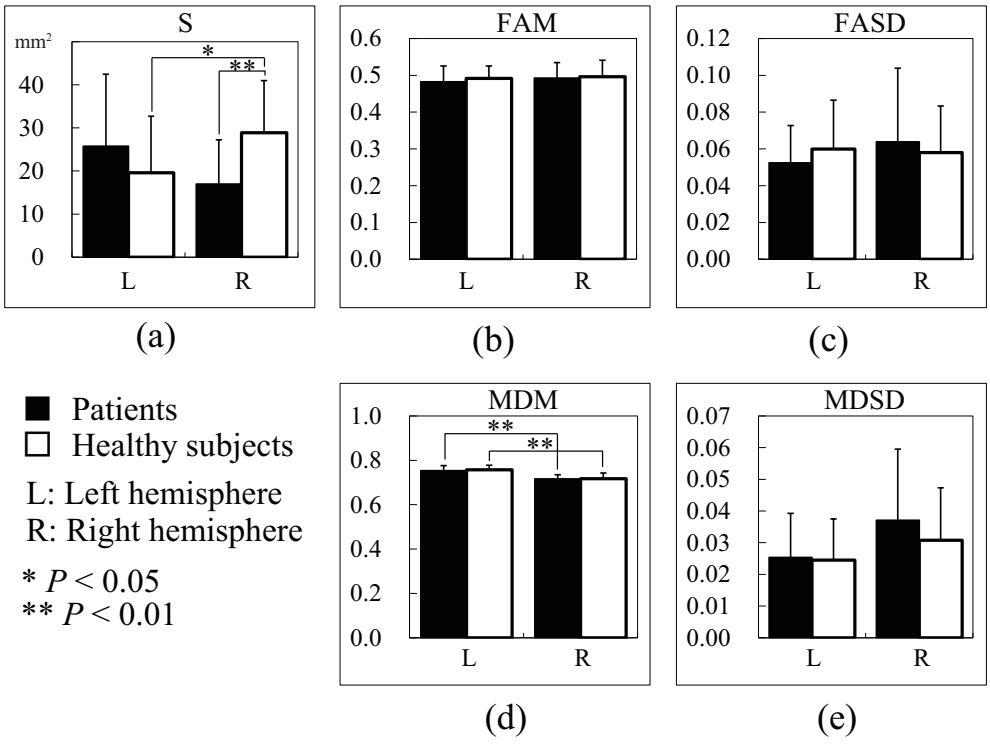

Figure 3.19: The average of five evaluation indices for the superior longitudinal fasciculus with the specified ROI based on the bilateral fibers.

Table 3.3: The results of two-way repeated-measured ANOVA for the superior longitudinal fasciculus with the specified ROI based on the bilateral fibers.

ANOVA						
	Group effect		Hemisphere effect		Interaction	
Indices	F(df=1, 33)	p	F(df=1, 33)	p	F(df=1, 33)	p
S	0.810	0.371	0.006	0.937	8.018	0.006
FAM	0.375	0.542	0.562	0.456	0.069	0.794
FASD	0.014	0.905	0.472	0.494	0.945	0.335
MDM	0.165	0.686	49.107	0.000	0.098	0.755
MDSD	0.792	0.377	4.979	0.029	0.463	0.499

Table 3.4: The results of the t-test separately examining three indices between patient and healthy comparison subject groups and between left and right hemispheres for the superior longitudinal fasciculus with the specified ROI based on the bilateral fibers.

t-test						
	Group effect (Patient - Healthy)					
	Left			Right		
Indices	t Value	df	P Value	t Value	df	P Value
S	1.225	33	0.229	3.033	33	0.005
	Hemisphere effect (Left - Right)					
	Patient			Healthy		
Indices	t Value	df	P Value	t Value	df	P Value
S	1.681	26	0.105	2.394	40	0.021
MDM	4.646	26	0.000	5.549	40	0.000
MDSD	1.658	26	0.109	1.359	40	0.182

significance level $P < 0.05$ and the double asterisk with the significance level was $P < 0.01$. The statistical results in the t-test were almost same to the case with the uniquely specified ROI, however, we could detect the significant difference of S between hemispheres in the healthy comparison group and more strong effect of S between groups in the right hemisphere.

3.8.2 Inferior longitudinal fasciculus

The tractographies for a representative single subject in each group are shown in Figure 3.20. They are displayed with MATLAB for more clear depiction. The axis direction of the whole image is the same to that of the image in the above subsection. In the close-up image, we can see the details of the tracked bundle. The sagittal and axial views are the images observed from the left side and the superior side, respectively. In the figure illustrating the tractography, the FA image is displayed for the reference with the tracked fibers. We colored the surface of the bundle of the tracked fibers with the RGB color corresponding to the color map, which is assigned to each voxel in the tracked fibers. The lines in the sagittal view describe the locations of the axial and coronal plane of the referenced FA image.

The means and standard deviations of the five evaluation indices for all subjects are shown with bar graphs in Figure 3.21. We provide the results of ANOVA in Table 3.5. In the inferior longitudinal fasciculus, ANOVA showed significant group effect and hemisphere effect for S, hemisphere effect for MDM, and group effect for MDSD. No other significant effects were observed.

The statistical results by t-tests are presented in Table 3.6. In the t-test for S, it was

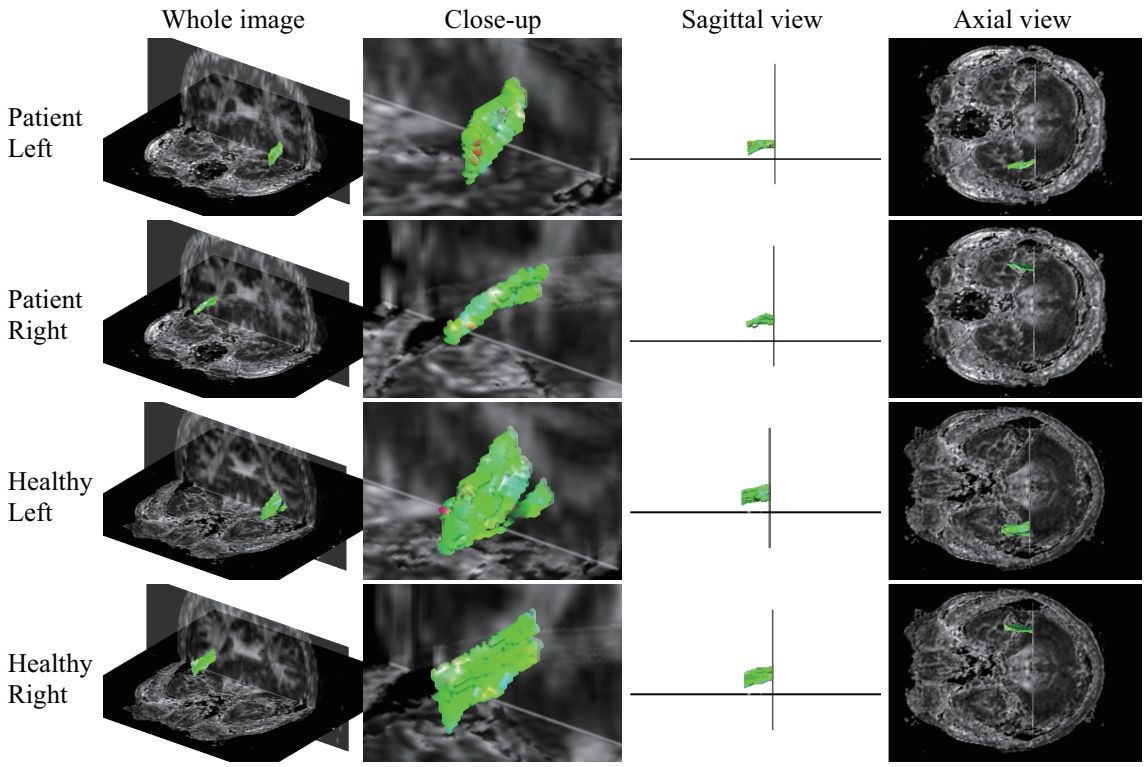

Figure 3.20: The tractography of the inferior longitudinal fasciculus with the specified ROI based on the unilateral fibers.

Table 3.5: The results of two-way repeated-measured ANOVA for the inferior longitudinal fasciculus.

Two-way ANOVA						
	Group effect		Hemisphere effect		Interaction	
Indices	F(df=1,33)	p	F(df=1,33)	p	F(df=1,33)	p
S	4.275	0.043	6.219	0.015	0.401	0.529
FAM	0.288	0.593	0.062	0.805	0.102	0.750
FASD	0.014	0.905	0.172	0.680	0.156	0.694
MDM	0.008	0.929	27.570	0.000	0.066	0.798
MDSD	6.026	0.017	2.147	0.148	0.406	0.526

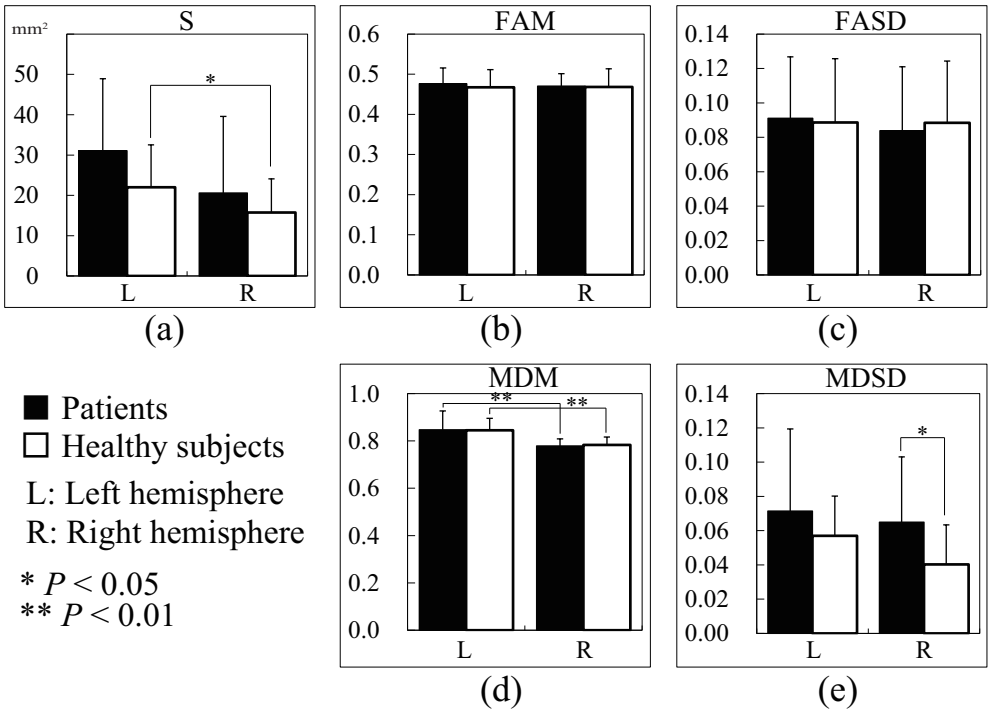

Figure 3.21: The average of five evaluation indices for the inferior longitudinal fasciculus with the specified ROI based on the unilateral fibers.

Table 3.6: The results of the t-test separately examining three indices between patient and healthy comparison subject groups and between left and right hemispheres for the inferior longitudinal fasciculus.

t-test						
	Group effect (Patient - Healthy)					
	Left			Right		
Indices	t Value	df	P Value	t Value	df	P Value
S	1.887	33	0.067	1.026	33	0.312
MDSD	1.194	33	0.240	2.382	33	0.023
	Hemisphere effect (Left - Right)					
	Patient			Healthy		
Indices	t Value	df	P Value	t Value	df	P Value
S	1.502	26	0.145	2.131	40	0.039
MDM	2.985	26	0.006	4.646	40	0.000

found that left hemisphere was significantly larger than right in the comparison group, but between-hemisphere in the patient group showed no significant differences. In the left hemisphere, patients' S was tend to be large compared with that in the comparison group, but between-group in the right hemisphere showed no significant differences. For MDM, left hemisphere was significantly larger than right in the patient group and the comparison group. For MDSD, the patient group showed significantly larger value than that in the comparison group in the right hemisphere, but between-group in the left hemisphere showed no significant differences. The pairs, which had significant differences are shown in Figure 3.21 with asterisks.

3.8.3 Inferior fronto-occipital fasciculus

The tractographies for a representative single subject in each group are shown in Figure 3.22. The way to display the images was the same to the case of the inferior longitudinal fasciculus.

We show the means and standard deviations of the five evaluation indices for all subjects in Figure 3.23. The results of ANOVA are represented in Table 3.7. In the inferior fronto-occipital fasciculus, ANOVA showed significant hemisphere effect and group-by-hemisphere interaction for S, hemisphere effect for FAM, group effect and hemisphere effect for MDM and group effect and hemisphere effect for MDSD. No other significant effects were observed.

In the t-test for S, right hemisphere showed significantly larger value than that in the left in the comparison group, but between-hemisphere in the patient group, between-group in the left hemisphere and the right hemisphere showed no significant differences. For FAM, right hemisphere showed significantly larger value than that in the left in the patient group and the comparison group. For MDM, the patient group showed significantly larger value than that in the comparison group in the left and right hemispheres, and left hemisphere showed significantly larger value than in the right in the patient and the comparison groups. For MDSD, the patient group showed significantly larger value than that in the comparison group in the left and right hemispheres, and right hemisphere showed significantly larger value than that in the left in the comparison group but between-hemisphere in the patient group showed no significant differences.

3.9 Discussion

The findings in this chapter illustrate the significant differences between the patient and healthy comparison groups and between the left and right hemispheres, using the manual setting ROI for the fiber tracking of the superior longitudinal, inferior longitudinal and fronto-occipital fasciculi.

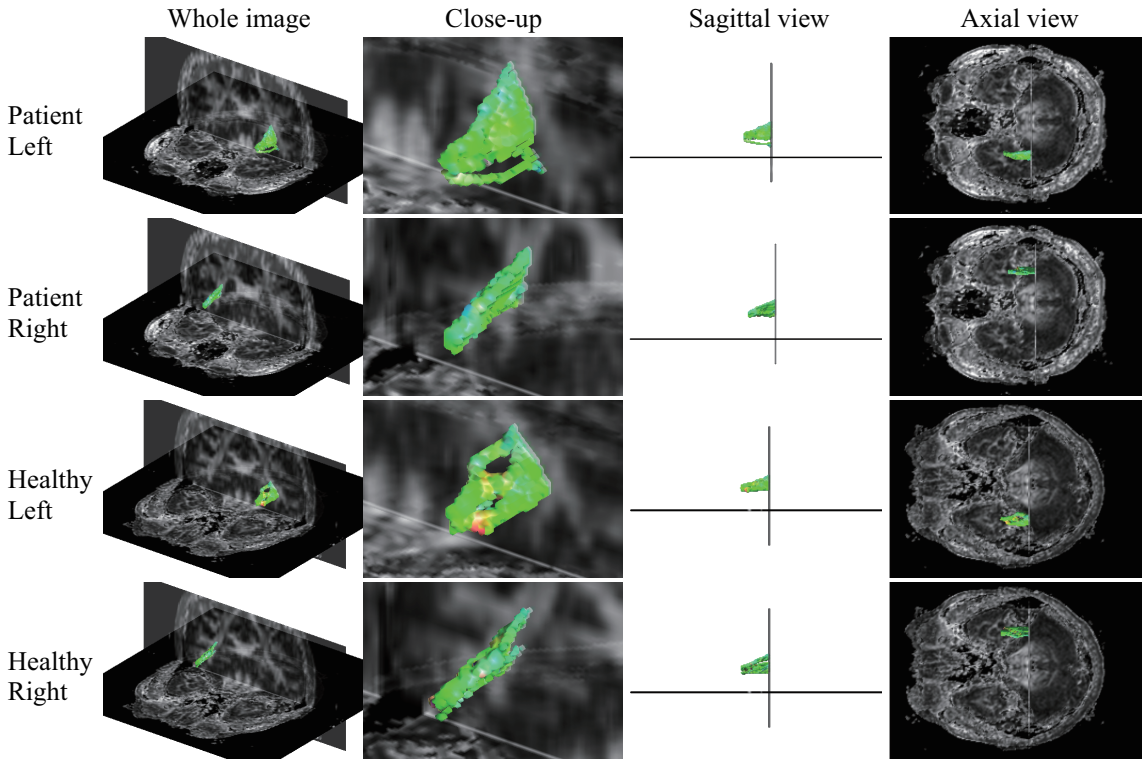

Figure 3.22: The tractography of the inferior fronto-occipital fasciculus with the specified ROI based on the unilateral fibers.

Table 3.7: The results of two-way repeated-measured ANOVA for the inferior fronto-occipital fasciculus.

Two-way ANOVA						
	Group effect		Hemisphere effect		Interaction	
Indices	F(df=1,33)	p	F(df=1,33)	p	F(df=1,33)	p
S	0.124	0.726	21.663	0.000	5.276	0.025
FAM	2.264	0.137	16.278	0.000	0.000	0.993
FASD	0.299	0.586	0.316	0.576	0.041	0.840
MDM	17.270	0.000	25.566	0.000	0.013	0.908
MDSD	11.739	0.001	5.459	0.023	0.069	0.794

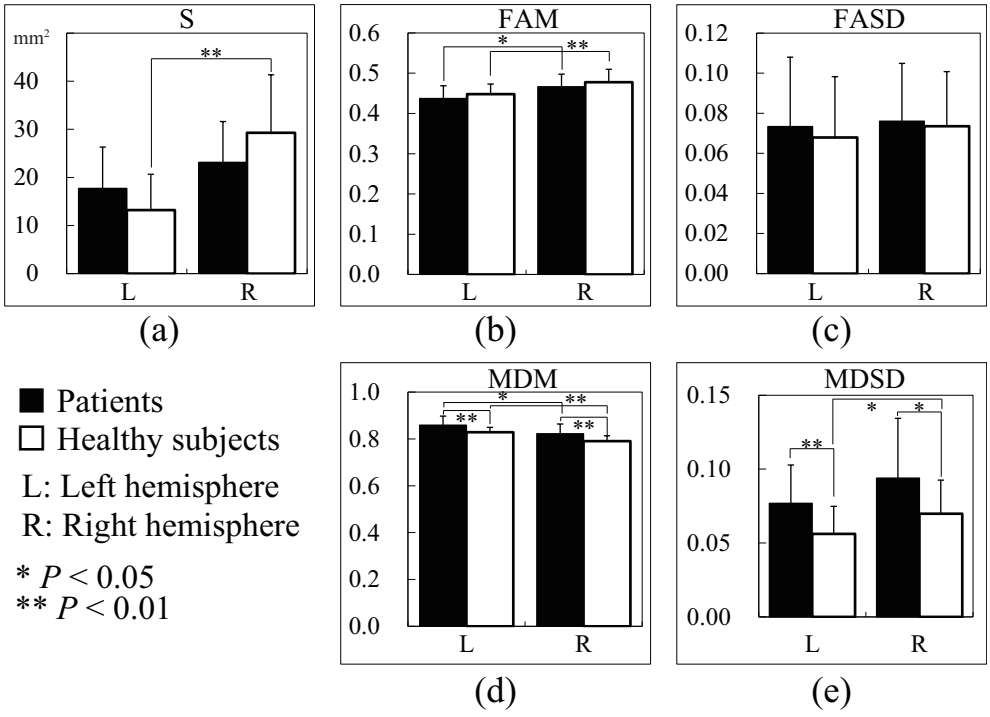

Figure 3.23: The average of five evaluation indices for the inferior fronto-occipital fasciculus with the specified ROI based on the unilateral fibers.

Table 3.8: The results of the t-test separately examining four indices between patient and healthy comparison subject groups and between left and right hemispheres for the inferior fronto-occipital fasciculus.

t-test						
	Group effect (Patient - Healthy)					
	Left			Right		
Indices	t Value	df	P Value	t Value	df	P Value
S	1.643	33	0.109	1.642	33	0.109
MDM	2.992	33	0.005	2.920	33	0.006
MDSD	2.749	33	0.009	2.254	33	0.030
	Hemisphere effect (Left - Right)					
	Patient			Healthy		
Indices	t Value	df	P Value	t Value	df	P Value
S	1.687	26	0.103	5.188	40	0.000
FAM	2.463	26	0.020	3.310	40	0.001
MDM	2.408	26	0.023	5.692	40	0.000
MDSD	1.322	26	0.197	2.115	40	0.040

For the superior longitudinal fasciculus, the significant differences of S between the patient and healthy comparison groups in the right hemisphere were observed in both cases with the uniquely specified ROI and the ROI specified with the maximum number of tracked fibers in both hemispheres. In addition, the hemisphere effect in the comparison group was shown with the ROI based on the number of fibers.

These results are not consistent exactly with the results in the previous study [30], but it is considered that they support the reported results. In the present study, we performed the fiber tracking in the range of FA > 0.25; i.e., the fiber tracking was terminated in the area where FA had a low value. The index S is corresponding to the number of the tracked fibers successfully from the starting area to the ending region. Since the number of the tracked fibers for the patient group reduced in the right hemisphere, the more number of streamline was terminated during the fiber tracking of the patient group compared to the healthy comparison group. Therefore, the reduction of FA for the patient group is considered to be reflected in the decrease of the number of tracked fibers.

We assumed that the decrease of S for the patient group also existed in the inferior longitudinal fasciculus, since the FA reduction was also reported for the bundle [21]. However, patient's S did not have smaller value in comparison to the healthy comparison subject. We interpreted this result as the inadequacy of the setting of ROI. The inferior longitudinal fasciculus and the inferior fronto-occipital fasciculus go through in the very close area. Owing to the manual setting of ROI, it could be considered that the arbitrariness was included in the definition of ROI and the bundles might not be separated adequately.

For the longitudinal fasciculus, patient's MDSD was greater than that of the healthy group. The mean diffusivity represents the degree that water molecules are easy to move in vivo; i.e. the white matter has a rough tissue in the area where the mean diffusivity shows the large value. The value of MDSD indicates the degree of the dispersion of the mean diffusivity and the degree of the inhomogeneity of the tissue. Therefore it is supposed that patients have more inhomogeneous tissue of the longitudinal fasciculus.

In the results of the fiber tracking for the inferior fronto-occipital fasciculus, MDM and MDSD had the significant group effect for both of the hemispheres. Since MDM reflects the density of brain tissue, it is considered that the inferior fronto-occipital fasciculus of patients has more rough tissue compared to that of the healthy subjects in both of hemispheres. On the other hand, it is thought that dispersion of the density of brain tissue may increase in the whole tracked fibers where MDSD is high level.

It is suggested that the structural abnormalities in the cerebral white matter of schizophrenic patients are reflected by changes in the indices, which have the significant differenced between groups. However the method for the setting of ROI leaves a problem in the quantity of work and the arbitrariness derived from the manual establishment. In

addition, it is supposed that the normalization of subject's brain corresponding to the standard normal brain is demanded for more reproducibility of the fiber tracking and the setting ROI. We expand this study to deal with above problems in the next chapter.

Chapter 4

Automatic ROI construction

We provide the automatic construction method of ROI for the fiber tracking and the application of the method to the quantitative evaluation of the schizophrenia. We perform the fiber tracking in the specific nerve bundle by using the ROI construction and the normalization of the subject's image to improve the reproducibility. The statistical analysis is performed for the indices signifying the extracted features of the bundle. The manual ROI setting in the previous chapter suffers from the arbitrariness to determine the starting area in the fiber tracking. We overcome the crucial problem on the previous study by the proposal of the automatic ROI construction, which can avoid the inherent error in the previous study. It gives rise to the improvement of the accuracy of the ROI construction in the present scheme. The results suggest the efficiency of the definition of ROI for the evaluation of patient's abnormality in the white matter, and the feasibility of the quantitative evaluation eliminating the arbitrariness for the schizophrenic patients.

4.1 Image processing

We use the same MR-DTI images of the same subjects as those in Chapter 3. The 14 schizophrenic patients and the 21 healthy comparison subjects were recruited in Kyorin University Hospital for this study. We normalize the subjects' images corresponding to the standard brain before performance of the construction of ROI.

For the normalization, we use MRI Studio, the image processing software, including DTI Studio (Version 3.0.3) [61], ROI Editor (Version 1.5), and Diffeo Map (Version 1.7.3), which are developed through the support of the Laboratory of Brain Anatomical MRI and the Center for Imaging Science at Johns Hopkins University (https://www.mristudio.org/). The details of actual operation for the normalization by MRI Studio are given in Appendix A.

DTI Studio calculates the diffusion tensor, the first eigenvector and eigenvalue of the diffusion tensor, the FA value, and the trace using MR-DTI data in dicom format. The

trace is defined as follows; i.e., it has three times as large as the MD value.

$$\text{trace} = \lambda_1 + \lambda_2 + \lambda_3, \tag{4.1}$$

where λ_1, λ_2, and λ_3 indicate the eigenvalues of the diffusion tensor data. We transform the trace data to the MD data when we calculate the MD value along the tracked fibers.

As described in Appendix A, the originally acquired images of subjects are loaded in DTI Studio and the artifacts by brain motion are removed. The $b0$ image, the diffusion tensor data, the first eigenvector and eigenvalue data of the diffusion tensor, the FA and trace images, and the color map are obtained by the calculations in DTI Studio.

In order to normalize the subject's brain according to the standard brain accurately, we extract only the area including the cerebral parenchyma. This operation is called the skull stripping [62]. ROI Editor is used to apply the skull stripping to the calculated data sets. The mask for the skull stripping is determined on the $b0$ image in each subject, and it is applied to the FA, trace, and first eigenvector images as described in Appendix A.

All skull stripped images are resampled according to the standard brain, which has a $181 \times 217 \times 181$ matrix and a voxel size of $1 \times 1 \times 1$ mm^3. We use the single subject image on the MNI (Montréal Neurological Institute) coordinate for the standard brain named 'JHU MNI SS' in Diffeo Map.

The normalization of the subject's brain corresponding to the standard brain is performed through both of the linear and the nonlinear transformations. The linear transformation matrix is made with Diffeo Map matching the $b0$ image of each subject to that of the standard brain, and the matrix is applied to all the resampled images.

We normalize the subject's images nonlinearly corresponding to the standard brain, using both of the FA image and the trace image. In the FA image, it is easy to recognize the contrast between the white matter and the other tissues such as the gray matter and the cerebrospinal fluid. The trace image is sensitive to the discrimination between the cerebrospinal fluid and the others. The multichannel transformation with the FA and trace images is considered that it has enough discernment of borders between tissues and it suits the transformation for the white matter and the tissues located in the center part of the brain.

The nonlinear transformation matrix is constructed with Diffeo Map based on the large deformation diffeomorphic metric mapping (LDDMM) [63] fitting to the standard brain. The matrix is applied to the linearly transformed $b0$, FA, trace, and first eigenvector images. The finally normalized $b0$ image in Figure A.16. The flow of these preprocessing and some setting of parameters given in Appendix A were instructed by the developers to suit them to this study.

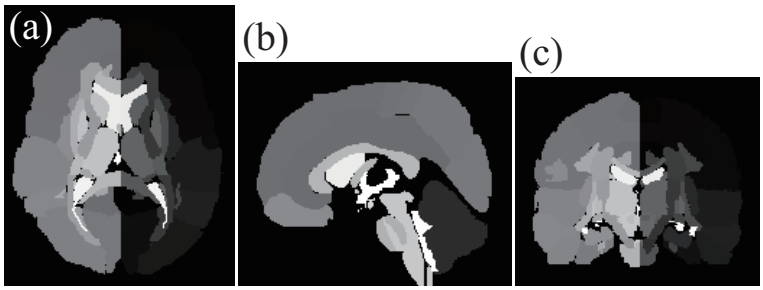

Figure 4.1: The parcellation map for the standard brain. (a) The axial image of $z = 83$, (b) The sagittal image on the midline ($x = 91$), and (c) The coronal image of $y = 109$.

4.2 Construction of ROI

The present study targets the sagittal stratum, including the inferior longitudinal fasciculus and the inferior fronto-occipital fasciculus, both of which are representative association fibers. The inferior longitudinal fasciculus and the inferior fronto-occipital fasciculus become aligned around the splenium of the corpus callosum, whereas they expand near the cerebral cortex. They are mixed around the coronal plane containing the center of the splenium of the corpus callosum, and form the sagittal stratum.

The image classified the brain into parcels is prepared in MRI studio, corresponding to the position of anatomical structures of the standard brain. We call this image the parcellation map. The region to start the fiber tracking and the ending region are selected using the parcellation map for the standard brain. In the applied parcellation map, both the gray and the white matters are separated into parcels corresponding to the anatomical disposition. The brain tissues are parcellated into 159 regions based on the original parcellation map (JHU MNI SS WMPM Type II) in MRI Studio [64, 62, 65]. Since each voxel has a nonnegative integer from 1 to 159 assigned to each segment, the parcellation map looks like Figure 4.1. This parcellation map is one prepared for the standard brain.

We employ the sagittal stratum instead of using the inferior longitudinal fasciculus and the inferior fronto-occipital fasciculus separately, since the segments for the two fasciculi are united into a single segment as the sagittal stratum in the targeted area in the parcellation map. It is not necessary to separate the bundles, if we can detect the abnormality of the white matter for the schizophrenic patients, since the aim of this study is to evaluate the abnormality quantitatively eliminating the arbitrariness as much as possible. In addition, we also target the superior longitudinal fasciculus to compare the result to the case in the previous chapter. The segments for the sagittal stratum (red), the anterior part of the inferior front-occipital fasciculus (orange), and the superior longitudinal fasciculus (blue) are colored in Figure 4.2 corresponding to the parcellation map over the FA image for the standard brain.

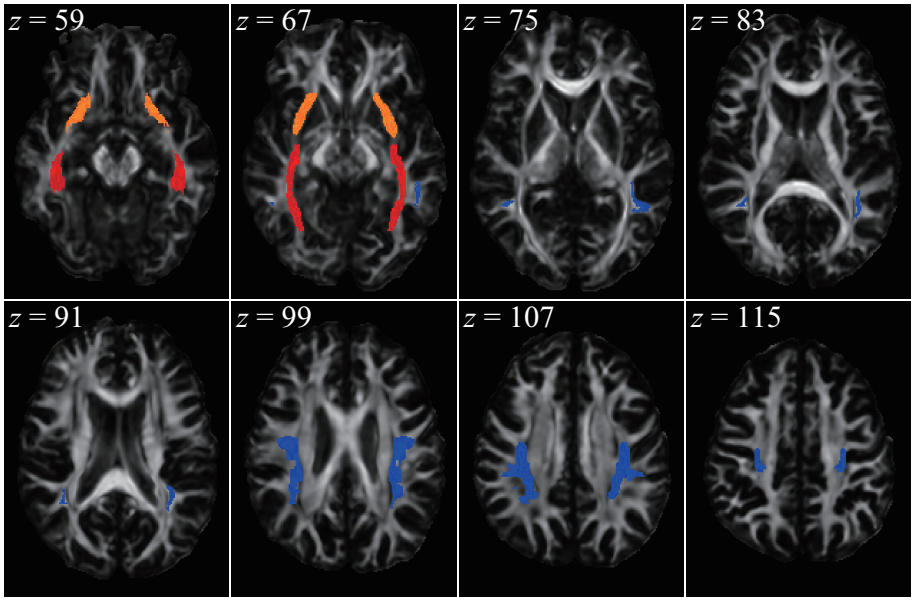

Figure 4.2: The segments for the sagittal stratum (red), the anterior part of the inferior front-occipital fasciculus (orange), and the superior longitudinal fasciculus (blue) corresponding to the parcellation map over the FA image for the standard brain. The value of z indicate the height of each axial slice.

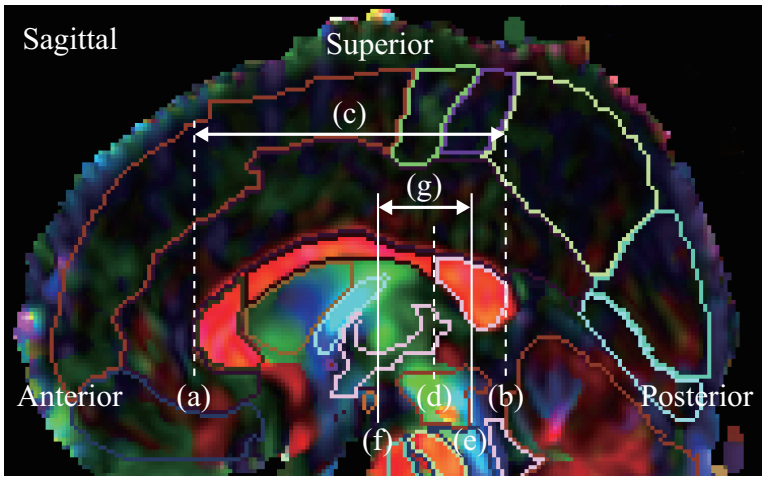

Figure 4.3: The selection of ROI for the fiber tracking of the sagittal stratum shown on a sagittal plane on a median line displayed as a color map of diffusion anisotropy. The line (e) represents the starting coronal plane, and the line (f) represents the ending coronal plane. Then, the fiber tracking is performed in the region (g).

4.2.1 Sagittal stratum

Uniquely specified ROI

We define the starting and ending regions on two distinct coronal planes. The left and right starting areas are prepared in the same coronal plane separately. We construct ROI based on the corpus callosum as described in the previous chapter.

In order to set ROI in the targeted nerve bundles, we first select the sagittal plane that includes the median line using the location of the segments, including the corpus callosum in the right and left hemispheres. The corpus callosum has three segments for each hemisphere in the parcellation map. They are the genu, body, and splenium of the corpus callosum corresponding to the anterior, center, and posterior part, respectively. Each segment has spatial extent in each hemisphere. We combine the three segments of the corpus callosum in each hemisphere, so as to determine the sagittal plane located in the midline of the brain. We employ the sagittal plane on the middle x-coordinate between the most left voxel among the right segments of the corpus callosum and the most right voxel among the left segments as the location of the median line.

Figure 4.3 shows this sagittal plane in a color map of the standard brain with the parcellation map. This figure is created using ROI Editor. In the midline sagittal plane (Fig. 4.3), we specify the anterior edge (a) and posterior edge (b) of the corpus callosum, along with the anterior edge of the splenium of the corpus callosum (d) based on the parcellation map.

After that, we establish the coronal plane (e), which includes the center of the splenium of the corpus callosum as the starting plane for fiber tracking. In addition, we set the plane (f) 40 % ahead of the diameter of the corpus callosum (c) from the posterior edge of the corpus callosum (b) as the ending plane. In Figure 4.3, region (g) represents the tracking region. The position referring to the location of the corpus callosum to define the starting and ending planes is the same as the case in Subsection 3.4.2 in the previous chapter.

Extracting the axial slice of the color map that includes the segments of the targeted bundles in Figure 4.4, we can see the left and right sagittal stratums, including the inferior longitudinal fasciculus and the inferior fronto-occipital fasciculus in the areas surrounded by the red and blue frames, respectively. The purple and brown areas indicate the left and right inferior fronto-occipital fasciculi. In this axial plane, (e) shows the starting plane for fiber tracking, and (f) represents the ending plane.

The right and left starting regions in the same coronal plane are prepared separately. In Chapter 3, we established ROI with square areas manually. However, the starting area is set inside the targeted segment in the parcellation map to eliminate the untargeted fibers and the arbitrariness in this chapter. The ending region is determined as the whole

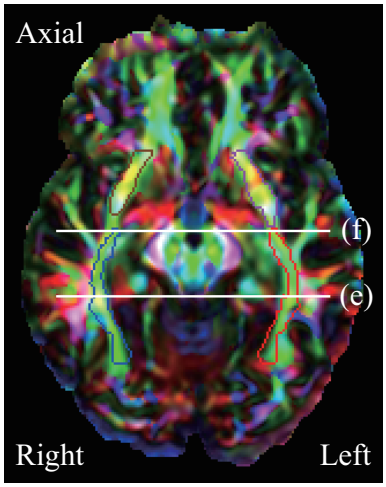

Figure 4.4: The starting (e) and ending (f) planes on axial color map ($z = 63$). The regions surrounded by the red and blue frames represent the segments of the sagittal stratum, including the inferior longitudinal fasciculus and the inferior fronto-occipital fasciculus. The purple and brown frames show the segments, which include the inferior fronto-occipital fasciculus.

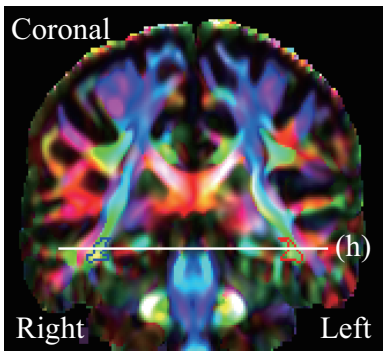

Figure 4.5: The starting plane on coronal color map. The red and blue framed regions represent the left starting region and the right starting region, respectively. The seed points are dispersed evenly in these starting regions at a rate of 4 points per 1 mm^2.

plane of the ending coronal plane.

Separate starting regions are set in the segment for the sagittal stratum on the starting coronal plane (Figure 4.5) for the left and right hemispheres. The red edged region represents the left starting region, and the area surrounded by the blue frame is that of the right hemisphere. The line (h) in Figure 4.5 represents the axial slice in Figure 4.4. These tracking region selections are performed automatically based on the parcellation map corresponding to the standard brain.

Specified ROI based on the unilateral fibers

To deal with individual differences in the positions of nerve bundles, we select the starting and ending planes for the fiber tracking according to the number of tracked streamlines in each subject. The starting and ending planes in the above case are defined as the initial starting and ending planes in this case. Those planes are selected where the maximum number of streamlines is tracked when changing the regions anteroposterior by up to 5 % of the diameter of the corpus callosum in the sagittal plane of the median line from the initial regions. This ratio is the same as that of Subsection 3.4.2. It is considered to be effective for excluding the influence of the position. When the starting and ending planes shift around the initial planes, the distance from the starting plane to the ending plane (Fig. 4.3(g)) are constant.

The starting region is restricted to the sagittal stratum area of the parcellation map on each starting coronal plane during the anteroposterior changing of ROI. For all changed ROI, the ending region is established in the whole coronal plane.

4.2.2 Superior longitudinal fasciculus

The starting and ending planes are determined in the same way as the case in Subsection 3.4.1 in the previous chapter. In this chapter the planes are set based on the parcellation map. We recognize the anterior edge and the posterior edge of the corpus callosum, and the anterior side of the splenium of corpus callosum similar to the case of the sagittal stratum in this chapter. The coronal plane including the anterior edge of the splenium of corpus callosum is established the starting plane. In Figure 4.6, the line (d) represents the starting coronal plane. We set the coronal plane 40 % of the width of the corpus callosum (Figure 4.6 (c)) ahead from the posterior edge of the corpus callosum as the ending plane (e). The area (f) indicates the anteroposterior distance of ROI in Figure 4.6.

Looked on the axial image (Figure 4.7), the segments for the right and left hemispheres of the superior longitudinal fasciculus are the areas surrounded by the blue and red frames. We can see that the targeted bundle is colored greenish, since the superior longitudinal fasciculus goes along the y axis. The lines of (d) and (e) represent the starting and ending coronal planes, respectively.

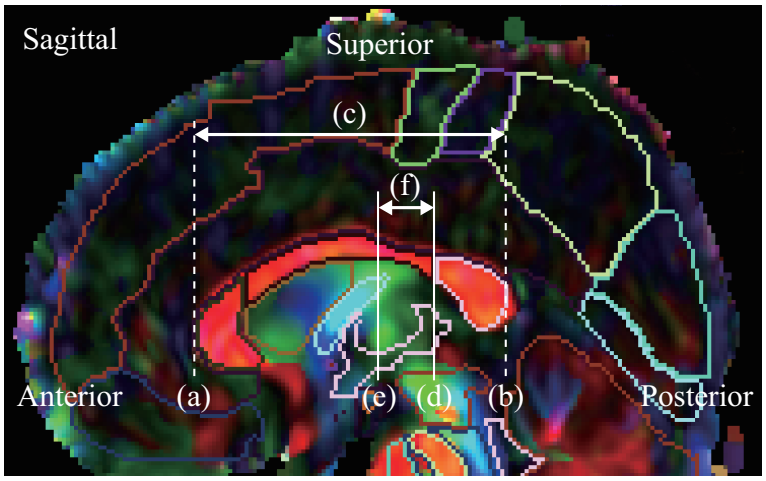

Figure 4.6: The selection of ROI for the fiber tracking of the superior longitudinal fasciculus shown on a sagittal plane on a median line displayed as a color map of diffusion anisotropy. The line (d) represents the starting coronal plane, and the line (e) represents the ending coronal plane. Then, the fiber tracking is performed in the region (f).

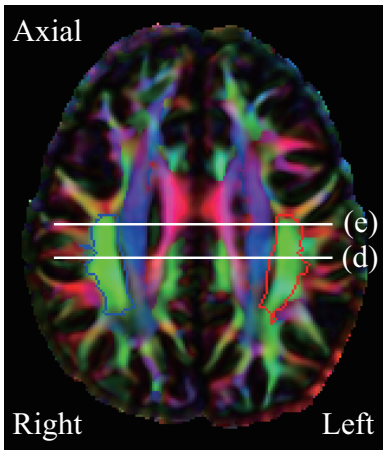

Figure 4.7: The starting (d) and ending (e) planes on axial color map ($z = 102$). The regions surrounded by the red and blue frames represent the segments of the superior longitudinal fasciculus.

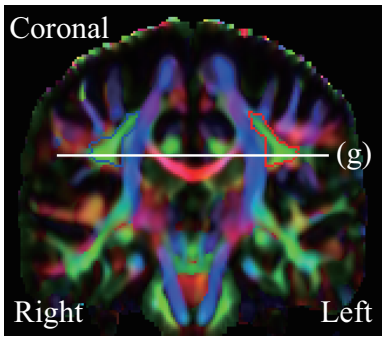

Figure 4.8: The starting plane on coronal color map. The red and blue framed regions represent the left starting region and the right starting region, respectively. The line (g) indicates the axial plane in Figure 4.7.

We establish the starting regions inside the segment for the superior longitudinal fasciculus of the parcellation map on the starting coronal plane. In Figure 4.8 the framed areas with blue and red colors indicate the starting region for the fiber tracking of the superior longitudinal fasciculus. The ending region is set on the whole ending coronal plane.

4.3 Fiber tracking with the constructed ROI

We employ the resampled and normalized images; the first eigenvector, the FA, and the trace images. The value in each voxel of the trace image divided by three makes the image having the MD value. In order to construct ROI for the fiber tracking, we identify the corpus callosum and the targeted bundles in the parcellation map for the standard brain. The starting region is determined the integer three-dimensional coordinates in the coordinate system for the standard brain.

Fiber tracking is performed using a deterministic method used in Chapter 3. The seed points are dispersed evenly on the plane of the starting region at a rate of 4 points per 1 mm^2. Although this rate may seem relatively few, it is enough to extract the feature of the fibers by the tracking, since the more starting points result only the increase of the number of the streamlines, which are close to each other and form the similar shape. The y component of the coordinate of the seed point is set at the posterior edge of the starting plane, which has a thickness of 1 mm, since we select the location of the starting region based on the locations of voxels. The x and z coordinates of four seed points in a unit pixel are established at a center of each section divided a pixel into four sections.

The first eigenvector at the stepping point, which orientation coincides with the direction of the fiber tracking, is determined by interpolating according to the volume data among the center points of the nearest eight voxels around the stepping point. The way

of the interpolation is the same as the method mentioned in Section 3.3 in the previous chapter. However, note that the voxel size is already resampled to 1 mm cube.

4.4 Terminal criteria

The fiber tracking is terminated in a case of matching the terminal criteria. When the tracking is performed successfully, it is terminated just after the present stepping point reaches the position anterior to the ending plane. We keep the calculated values of only the successful streamlines. We determine the terminal criteria for the inside and outside of ROI.

For the terminal criteria for the outside of ROI, we restrict the present stepping point between the starting and ending planes in a single hemisphere. If the tracking go behind the starting plane, the fiber tracking is not successful and it is terminated. This case does not happens usually, since we determine the assumed orientation of tracking to the seed point with the anterior direction along the y axis. However it sometimes happens, after a fiber is tracked for a long way, which must be out of the targeted bundle. In addition, if the present position of the stepping point irrupts into another hemisphere, which is the opposite side of the seed point, the tracking is ended and eliminated from the stored results.

The terminal criteria in ROI before the tracking reaches the ending region are chosen on the basis of the FA value at the present stepping point, and the deflected angle between the two stepping directions of the continuous steps. A FA value represents a photometric feature in MR-DTI imaging. It reflects the microstructural measurement of brain tissues. A deflected angle is associated with a morphometric character in the fiber tracking. It is affected by the shape of the fibers. The threshold of FA and the deflected angle are set as 0.25 and 45°, respectively. These values are the same as the previous chapter.

The baseline length are also determined as same as the case of the previous chapter. Any streamlines with a length exceeding 110 % of the baseline streamline length are judged to have an erroneous tracking result and are thus eliminated from the streamline group for the tracking of the sagittal stratum. Since the sagittal stratum is corresponding to the inferior longitudinal and fronto-occipital fasciculi in the previous chapter, we apply the same ratio for the threshold of the fiber tracking of the sagittal stratum. For the superior longitudinal fasciculus, we employ 105 % of the baseline streamline length as well as the case in the previous chapter.

4.5 Statistics

For statistical analysis, we introduce 'S', 'Cu', and 'DA' for the morphometric indices as well as 'FA' and 'MD' for the photometric measurements representing the microstructural feature of tissues. The values of FA and MD reflect fiber density, axonal diameter, and myelination in the white matter. In contrast, S is given by the thickness of the fiber bundle, Cu is associated with the shape of a mass of axons, and DA is also corresponding to the shape of the fibers. Since the fiber tracking is performed along the direction of axons, Cu characterizes the conformation of the lying fiber tract. We determine not only the microstructural indices but also the morphometric indices to measure the form of the nerve bundle and the direction of axons derived from the fiber tracking.

We determine S as the cross-sectional area of the neuronal tract in the starting region. The value of S is defined as 0.25 mm^2 multiplied by the number of tracked fibers until the ending region continuously. A value of 0.25 mm^2 indicates the area of a single seed point. The unit of index S is mm^2. This index is the same definition as the case in the previous chapter.

In each stepping point, we calculate the FA value, MD value, curvature using the coordinates of the present, last, and next points (Cu), and the inner product between the incoming vector and the outgoing vector at the present point (DA). We named an index of the inner product DA, since the angle between the two vectors is called the deflected angle. The curvature at the present point i_m is obtained using the following equation.

$$\text{Cu}(i_m) = \frac{2|(\mathbf{p}_{m+1} - \mathbf{p}_m) \times (\mathbf{p}_m - \mathbf{p}_{m-1})|}{|\mathbf{p}_{m+1} - \mathbf{p}_m| \cdot |\mathbf{p}_m - \mathbf{p}_{m-1}| \cdot |\mathbf{p}_{m+1} - \mathbf{p}_{m-1}|}, \tag{4.2}$$

where $\mathbf{p}_m$ is the position vector at the present point i_m, and $m-1$ and $m+1$ represent the last and next points, respectively. For fiber tracking the total curvature must be small, since the nerve bundles with the relatively straight shape are targeted in this study. The large curvature reflects the varying directions of the first eigenvector during the tracking. The direction of the first eigenvector characterizes the integrity of axons in the tracked fiber.

The values of FA, MD, Cu, and DA are calculated in each tracking step. The tracking is performed along the axonal fibers. The values are averaged for all steps in a single fiber and for all fibers in the unilateral hemisphere to evaluate the overall feature of targeted bundle. The suffix of 'MM' for the abbreviation of indices represents these entirely averaged indices.

In order to assess the inhomogeneity among the characters of tracked fibers, we calculate the standard deviation of each averaged value in a single fiber for all fibers in a hemisphere. This inhomogeneity is according to the dispersion of axonal structures in a bundle. We name this index with the suffix of 'MSD'.

The standard deviations of FA, MD, and Cu for a single fiber are introduced to evaluate the inhomogeneity of the micro and macro structures along axons in a single fiber. We average the standard deviation for all fibers in a hemisphere. This index ends with 'SDM'.

In addition, we express the value of the standard deviation for all tracked fibers by 'SDSD'. This index characterizes the dispersion of the inhomogeneity in a single fiber among all of the tracked fibers in a hemisphere. It describes the intricate structure of the integral of axons.

We here summarize all seventeen indices represented by S, FAMM, FAMSD, FASDM, FASDSD, MDMM, MDMSD, MDSDM, MDSDSD, CuMM, CuMSD, CuSDM, CuSDSD, DAMM, DAMSD, DASDM, and DASDSD,. These indices do not have units except for S. All the indices are calculated separately for the right and left hemispheres in the individual subjects. The definitions of FAMM, FASDM, MDMM, and MDSDM are corresponding to those of FAM, FASD, MDM, and MDSD in the previous chapter, respectively.

We perform a two-way repeated-measured analysis of variance (ANOVA) to compare all the evaluation indices for groups as the intergroup factor and hemispheres as the intra-subject factor. For the factors having significant effects (significance level of $P < 0.05$) or tending to have significant effects ($P < 0.1$) in ANOVA, separate t-tests are carried out for comparisons between the patient and healthy comparison groups, and between the left and right hemispheres. The statistical analysis is conducted using MATLAB.

4.6 Results

We describe the results obtained through the fiber tracking for the sagittal stratum and the superior longitudinal fasciculus. The tractographies depicted by MATLAB of the representative subjects and the results by the statistical analysis for all indices are provided in this section. In the figures representing the tractography with FA maps, the coronal slice in the whole image placed in the left column indicates the starting plane or the initial starting plane of the fiber tracking. We see the tracked fibers from the superior side of the brain in the axial image in the center column. The close-up image of the tracked fibers are placed in the right column for both of hemispheres separately. The coloring of the tracked fibers follows the color map. All tractographies are constructed in MATLAB.

In addition, the means and standard deviations of all the indices are calculated separately for the right and left hemispheres in the patient and healthy comparison groups. Those values of the seventeen indices for all subjects are plotted as a bar graph in each case. In each plot of an index, the mean value is shown as a bar graph and the standard deviation is represented as an error bar. The two bar graphs in the left side labeled L represent the values in the left hemisphere, and the right bar graphs labeled R indicates the measurement in the right hemisphere. The results of the patient group are shown

in the black color, and those of the healthy comparison group are described in the white color.

The results with statistics of the two-way repeated-measured ANOVA and the t-test are shown in tables. In the tables representing the results of the ANOVA, we provide the distance between individual distributions F, the degree of freedom df, and the significance level P for the intergroup factor as the group effect, the intra-subject factor as the hemisphere effect, and the interaction of the two factors corresponding to all indices. When the P value is less than 0.05 (cells with dark shade in each table), we assess that the factor is significant for the index. The factor is tend to affect the index in the case that the P value is less than 0.1 and more than 0.05 (cells with light shade), although the factor is not determined to have a significant effect.

The t-test is performed for an index with a factor, which influences the index. We perform a t-test for a comparison of values of two groups in the left and right hemispheres separately, when the P value of the intergroup factor or the interaction is less than 0.1. The values of two hemispheres are examined by a t-test for the patient group and the healthy comparison group separately, when the P value of the intra-subject factor or the interaction is less than 0.1. In tables showing the results of the t-test, we show the results of the comparison between two groups in the upper half of the table, and the results between both hemispheres in the lower half of the table. We provide the t, df, and P values obtained through the t-test. For the results of the t-test, an index has a strong significant difference between groups or hemispheres when the significance level P is less than 0.01 (cells with dark shade in each table), and an index with the P value less than 0.05 has a significant difference at the comparison (cells with light shade).

4.6.1 Sagittal stratum

Uniquely specified ROI

The tractographies of the sagittal stratum with the uniquely specified ROI for representative subjects of the patient and the healthy comparison groups are displayed in Figures 4.9 and 4.10, respectively. The topmost subjects in both figures are corresponding to the subjects in Figures 3.20 and 3.22. The other represented subjects are corresponding to those in Figures 3.14 and 3.15, and Figures 3.17 and 3.18. We show the means and standard deviations of all indices in Figure 4.11.

Table 4.1 represents the results of ANOVA examinations, and Table 4.2 shows the results of the t-test. The ANOVA showed a significant effect by the intergroup factor for S, and by the intra-subject factor for MDMM, MDSDM, CuMSD, CuSDM, CuSDSD, DAMSD, and DASDSD. The tendencies of significant effects by the intra-subject factor for MDSDSD and by the interaction for MDSDM and MDSDSD were shown in the results

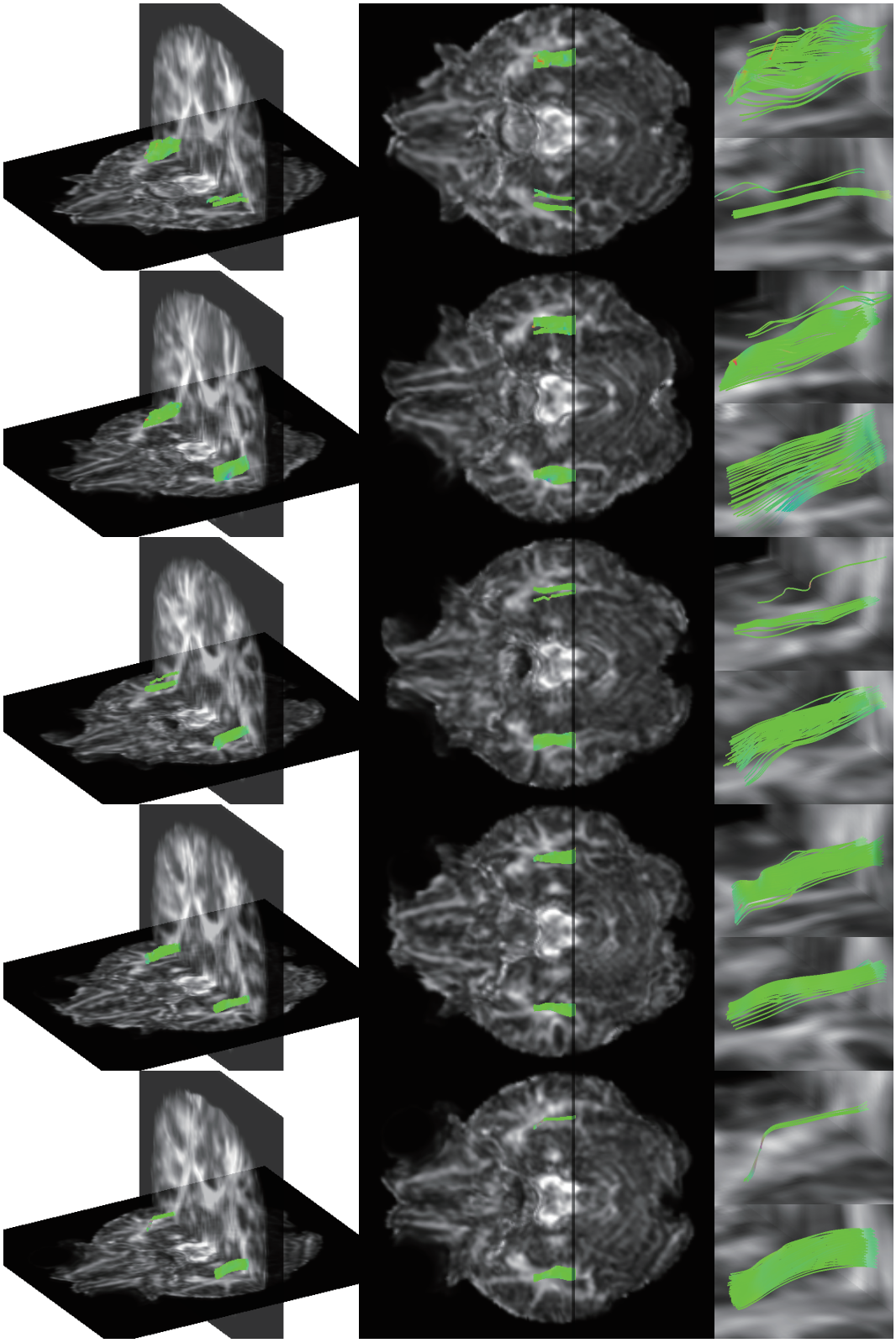

Figure 4.9: The tractography of the sagittal stratum with the uniquely specified ROI for the patient group.

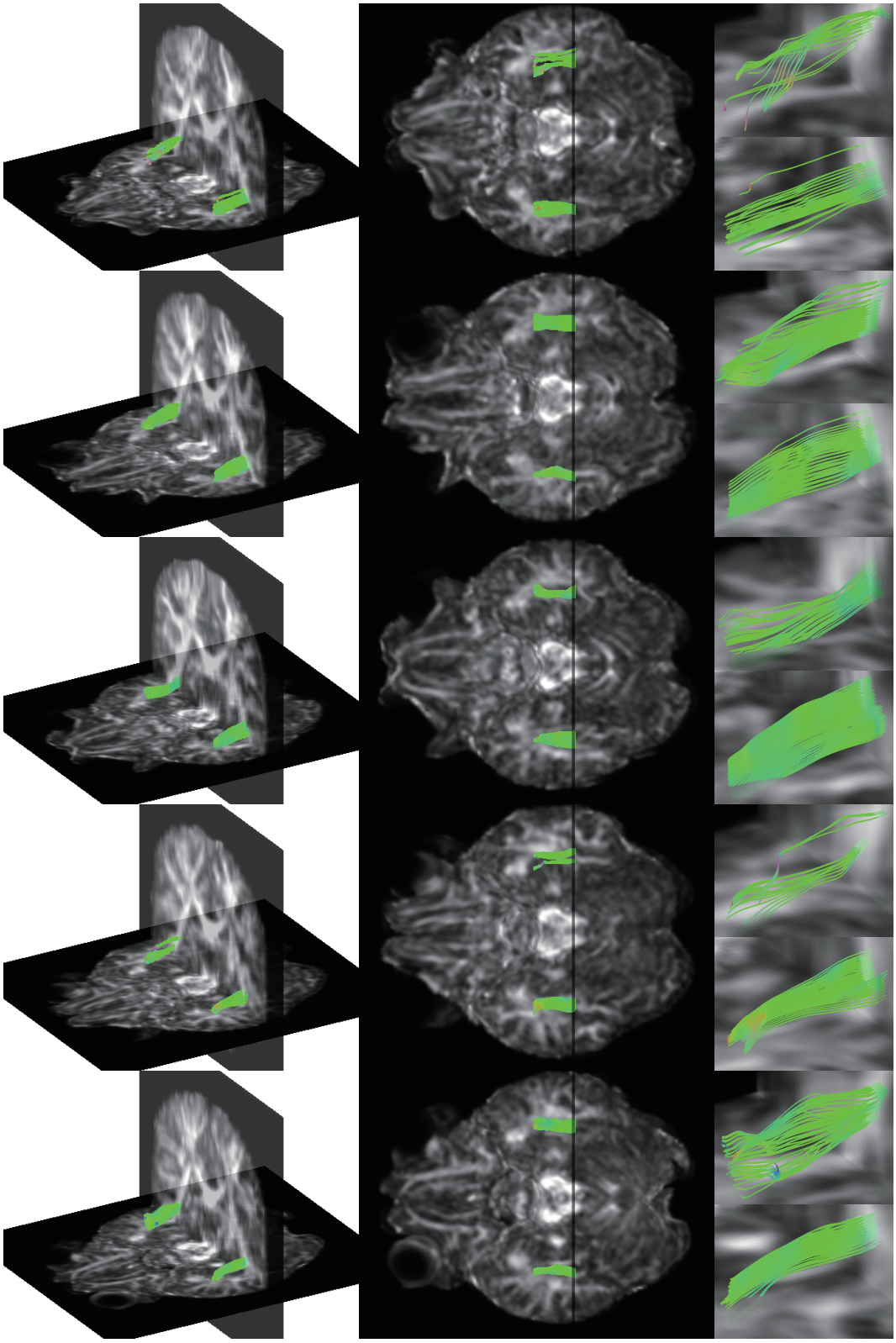

Figure 4.10: The tractography of the sagittal stratum with the uniquely specified ROI for the healthy comparison group.

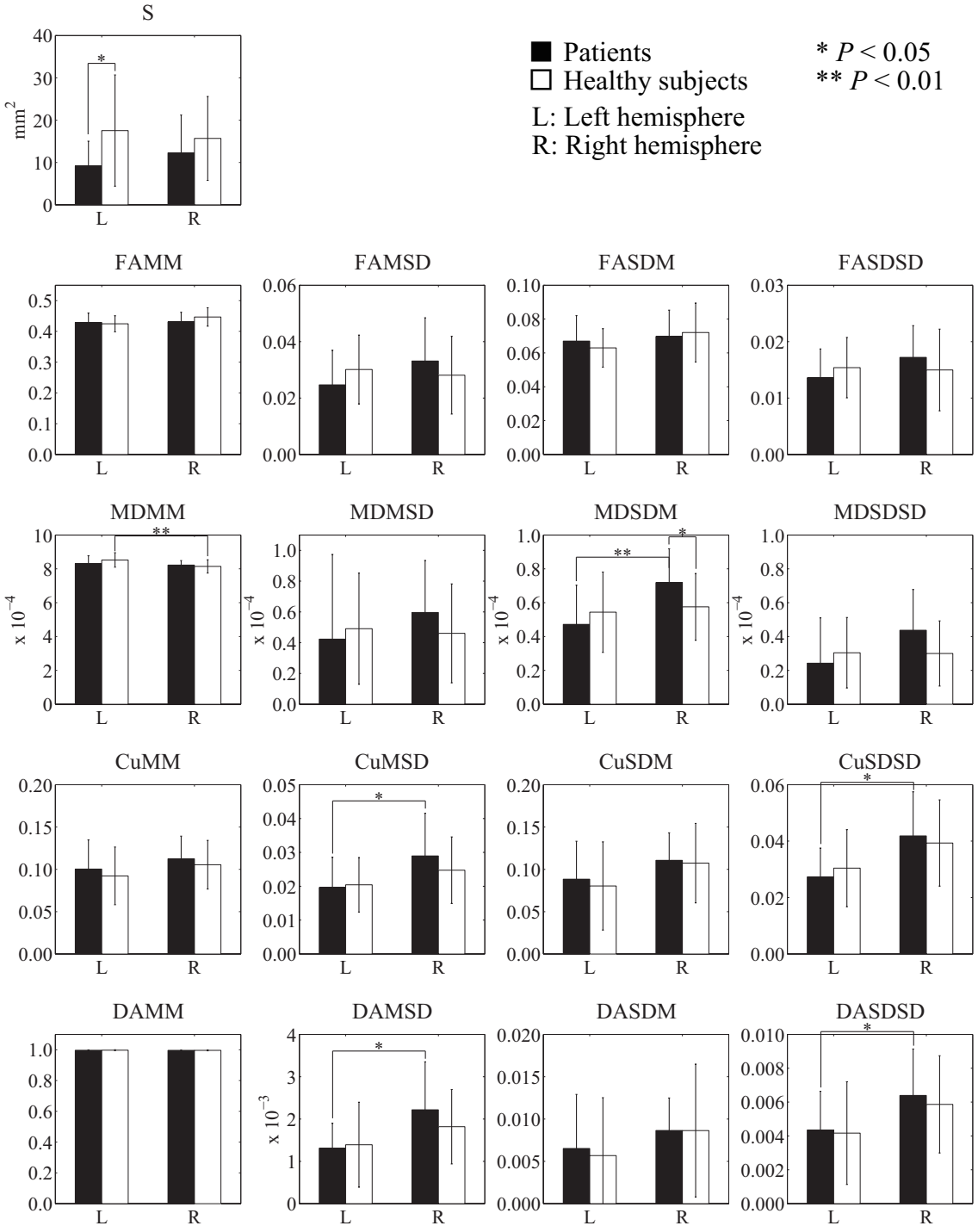

Figure 4.11: The bar plot of the mean value with the error bar of the standard deviation for all indices obtained through the fiber tracking of the sagittal stratum with the uniquely specified ROI.

Table 4.1: The results of ANOVA for indices of the sagittal stratum with the uniquely specified ROI, for comparison of all evaluation indices with group as intergroup factor and hemisphere as intra-subject factor.

Two-way ANOVA						
	Group effect		Hemisphere effect		Interaction	
Indices	$F(df = 1, 66)$	P value	$F(df = 1, 66)$	P value	$F(df = 1, 66)$	P value
S	5.273	0.025	0.059	0.808	0.936	0.337
FAMM	0.577	0.450	2.701	0.105	1.956	0.167
FAMSD	0.003	0.953	0.925	0.340	2.426	0.124
FASDM	0.051	0.822	2.462	0.121	0.719	0.399
FASDSD	0.020	0.888	1.128	0.292	1.788	0.186
MDMM	0.417	0.521	5.700	0.020	2.020	0.160
MDMSD	0.118	0.733	0.524	0.472	1.067	0.305
MDSDM	0.427	0.516	6.487	0.013	3.888	0.053
MDSDSD	0.456	0.502	2.866	0.095	3.135	0.081
CuMM	0.933	0.338	2.611	0.111	0.004	0.948
CuMSD	0.484	0.489	7.681	0.007	1.035	0.313
CuSDM	0.249	0.619	4.615	0.035	0.042	0.838
CuSDSD	0.007	0.932	11.096	0.001	0.634	0.429
DAMM	0.158	0.692	1.773	0.188	0.004	0.952
DAMSD	0.471	0.495	8.181	0.006	1.061	0.307
DASDM	0.066	0.798	2.348	0.130	0.062	0.804
DASDSD	0.257	0.614	7.128	0.010	0.061	0.805

of ANOVA. We examined these nine indices by t-tests.

According to the results of t-tests, the patient's value of S reduced significantly in comparison to that of the healthy subject in the left hemisphere. However, the values in the right hemisphere did not have a significant difference. Since the index S is corresponding to the thickness of the nerve bundle, it is considered that the patients have more thin tract in the sagittal stratum in the left hemisphere. The value of the right MDSDM of the patient group was larger than that of healthy group. In the comparison between hemispheres, the right MDSDM was larger than the left MDSDM in the patient group. The right values of CuMSD, CuSDSD, DAMSD, and DASDSD were significantly larger than the left values of those indices in the patient group.

The value of the right MDMM was significantly smaller than that of the left hemisphere in the healthy subject. The degree of mean diffusivity reflects the density of the in vivo tissue. In the areas where the MD value takes a small value, it is considered that the tissue has a dense structure. The small MDMM indicates that the entire magnitude of MD takes small degree. The healthy subjects may have the dense tissue in the sagittal

Table 4.2: The results of the t-tests examining nine indices between two groups and between both hemispheres for the sagittal stratum with the uniquely specified ROI.

t-test						
	Group effect (Patient - Healthy)					
	Left			Right		
Indices	t value	df	P value	t value	df	P value
S	2.174	33	0.037	1.006	33	0.322
MDSDM	0.863	33	0.395	2.035	33	0.050
MDSDSD	0.740	33	0.464	1.817	33	0.078
	Hemisphere effect (Left - Right)					
	Patient			Healthy		
Indices	t value	df	P value	t value	df	P value
MDMM	0.657	26	0.517	2.918	40	0.006
MDSDM	2.912	26	0.007	0.455	40	0.651
MDSDSD	1.949	26	0.062	0.069	40	0.945
CuMSD	2.178	26	0.039	1.522	40	0.136
CuSDM	1.455	26	0.158	1.723	40	0.093
CuSDSD	2.800	26	0.010	1.945	40	0.059
DAMSD	2.562	26	0.017	1.429	40	0.161
DASDSD	2.066	26	0.049	1.817	40	0.077

stratum in the right hemisphere.

The MDSDM had the significant differences in both of the group effect and hemisphere effect. The value of MDSDM indicates the degree of inhomogeneity of the magnitude of the diffusion in a each tracked trajectory. The magnitude of the diffusion reflects the microstructural integrity of axons in the white matter. Since the large MDSDM represents the disruption of the homogeneity, it is considered that the patient sagittal stratum in the right hemisphere lose the integrity compared to the healthy comparison subject.

The values of CuMSD and DAMSD reflect the dispersion of the shapes of all tracked trajectories in a hemisphere. The right values of these indices were larger than those of left hemisphere in the patient group, whereas the healthy comparison group did not show differences between hemispheres. In the right hemispheres of patients the sagittal stratum may have fibers of various shapes, although the shapes of the healthy subjects are relatively equable.

For CuSDSD and DASDSD, the values of the patient group had the significant differences between hemispheres. Although the healthy group did not have significant differences, the t-test shew the tendency that the right values were larger than the left values. The large values of these indices indicate the tracked trajectories contain fibers of both of straight and curved shapes. Therefore, it is considered that the right fibers have more various shape in both groups.

In the case of the fiber tracking with the uniquely specified ROI, the indices of S, MDMM, MDSDM, CuMSD, and DAMSD shew the features, which they discriminated the groups, since they had significant differences between groups or the results that either group had a significant difference between hemispheres and another group did not.

Specified ROI based on the unilateral fibers

We show the tractographies with the specified ROI based on the unilateral fibers for the sagittal stratum in Figures 4.12 and 4.13. Figure 4.12 represents the results for the patient group, and Figure 4.13 indicates the results for the healthy comparison group. The mean value of all indices are plotted in Figure 4.14. We provide the table representing the results obtained from statistical analyses in Tables 4.3 and 4.4.

The ANOVA showed a significant group effect for MDSDSD; hemisphere effect for FAMM, FASDM, MDMM, MDSDSD, CuMM, CuMSD, CuSDM, CuSDSD, DAMM, DAMSD, DASDM, and DASDSD; and group-by-hemisphere interaction for MDSDSD. The group effect for S and MDSDM, hemisphere effect for MDSDM, and group-by-hemisphere interaction for FAMSD tended to have significant differences in the ANOVA. No other significant effects were observed. Therefore, we examined these eleven indices by t-tests.

The results of this t-test are shown in Table 4.4. The group effect comparison between the patient and healthy comparison subjects is represented in the upper half of Table 4.4. The lower half indicates the hemisphere effect between the left and right hemispheres, separately for the patient group and the healthy group.

For the group effect, the MDSDM and MDSDSD values of the patient group were significantly larger than those of the healthy comparison group ($P < 0.05$). The patient's FAMSD value tended to be larger than that of a healthy subject ($P < 0.1$). No other significant differences were observed in the group effect.

For the hemisphere effect, the values in the right hemisphere were significantly larger than the values in the left for MDSDSD, CuMSD, CuSDM, CuSDSD, DAMSD, DASDM, and DASDSD in the patient group. The left value of DAMM was significantly larger than the right value in the patient group. In addition, the patient values for FAMSD, MDSDM, and CuMM in the right hemisphere tended to be larger than those in the left hemisphere ($P < 0.1$). In the healthy comparison group, FAMM, CuSDM, and DASDSD in the right hemisphere had significantly larger values than those in the left hemisphere, and only MDMM had a left value that was significantly larger than the right value ($P < 0.05$). The trends that the values in the right hemisphere were larger than those in the left hemisphere were observed in FASDM, CuMSD, CuSDSD, DAMSD, and DASDM ($P < 0.1$). No other significant differences were observed in the hemisphere effect.

Because MDSDM and MDSDSD showed significant group differences in the right hemisphere, it is reasonable that these two indices are appropriate as indices for the quantita-

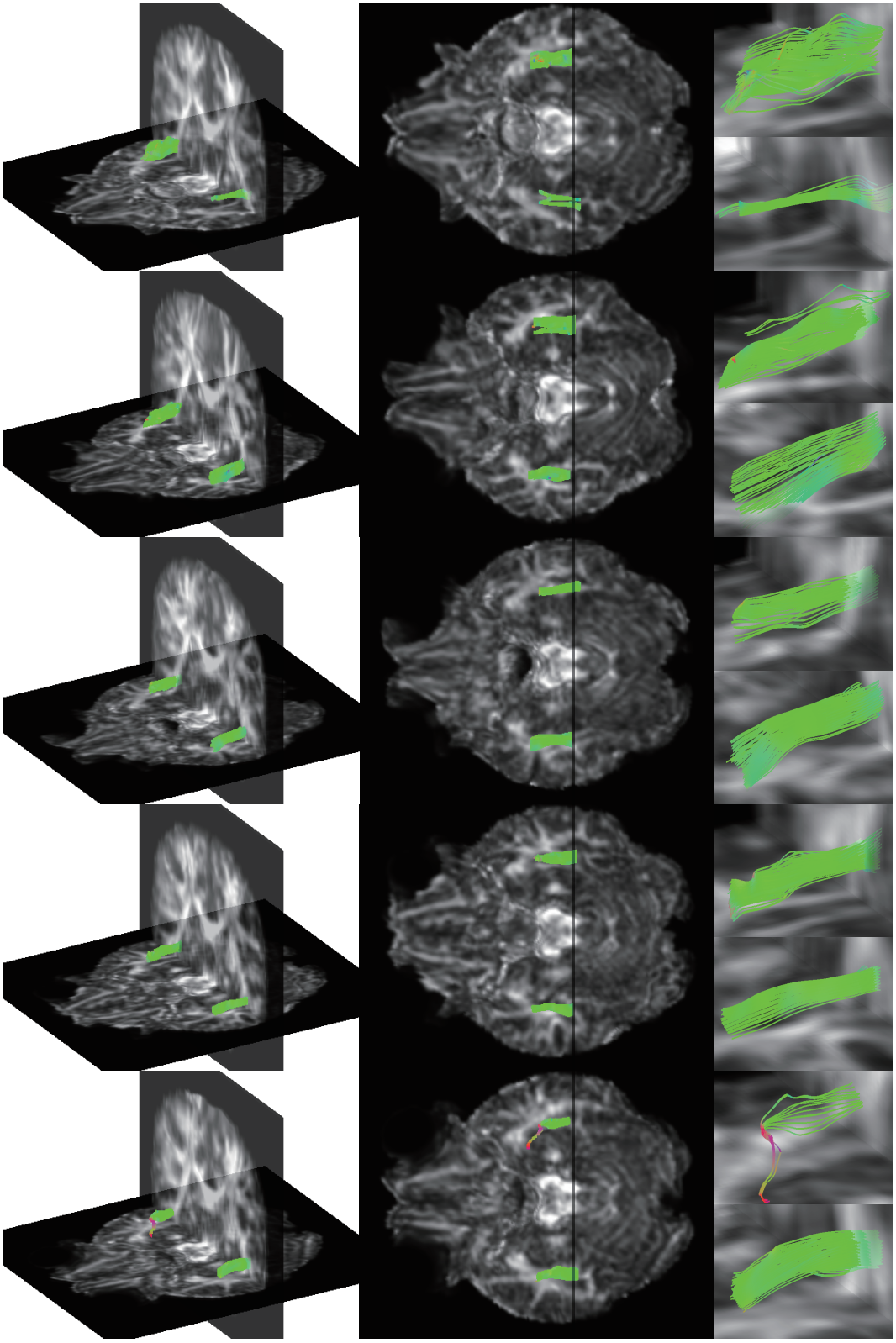

Figure 4.12: The tractography of the sagittal stratum with the specified ROI based on the unilateral fibers for the patient group.

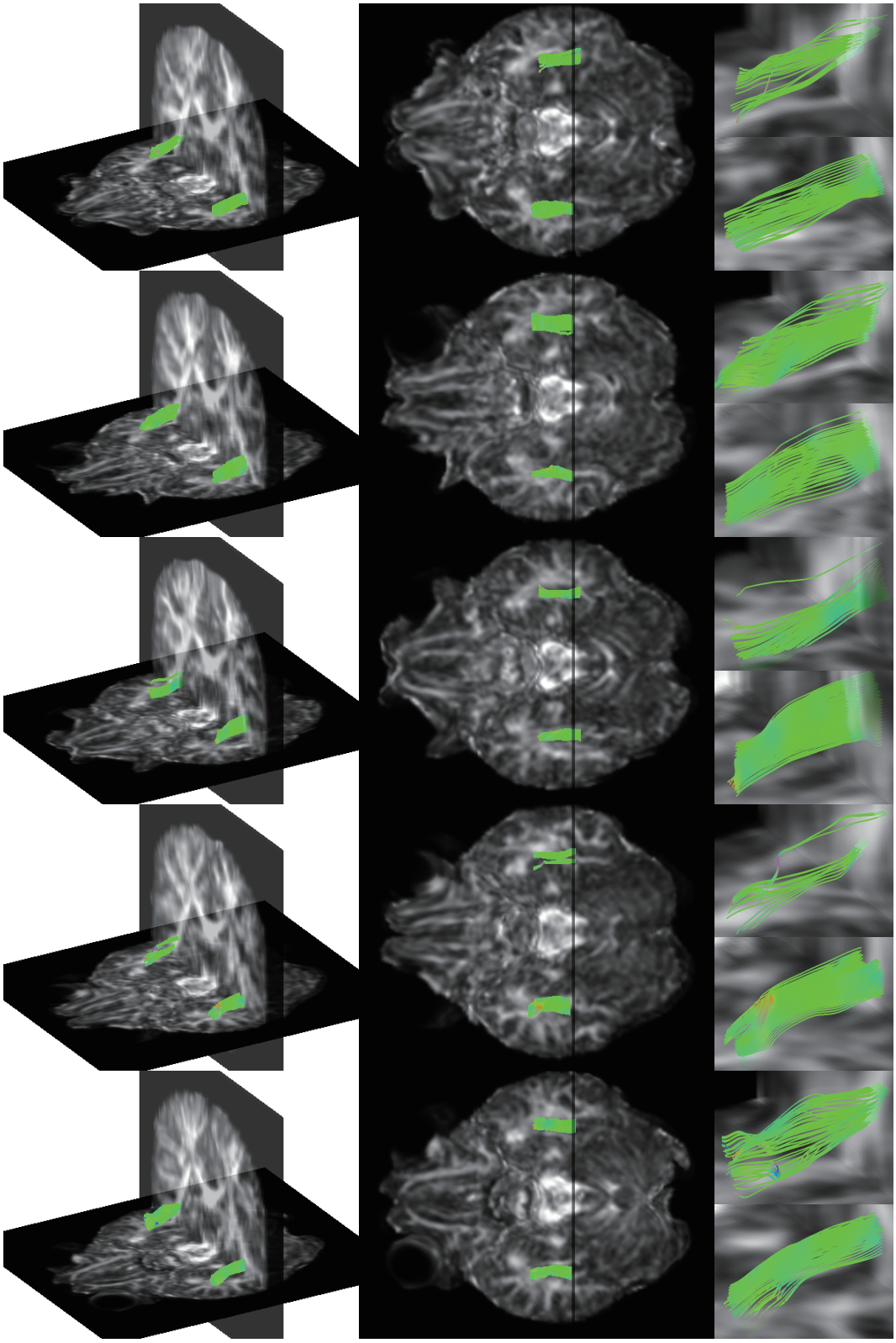

Figure 4.13: The tractography of the sagittal stratum with the specified ROI based on the unilateral fibers for the healthy comparison group.

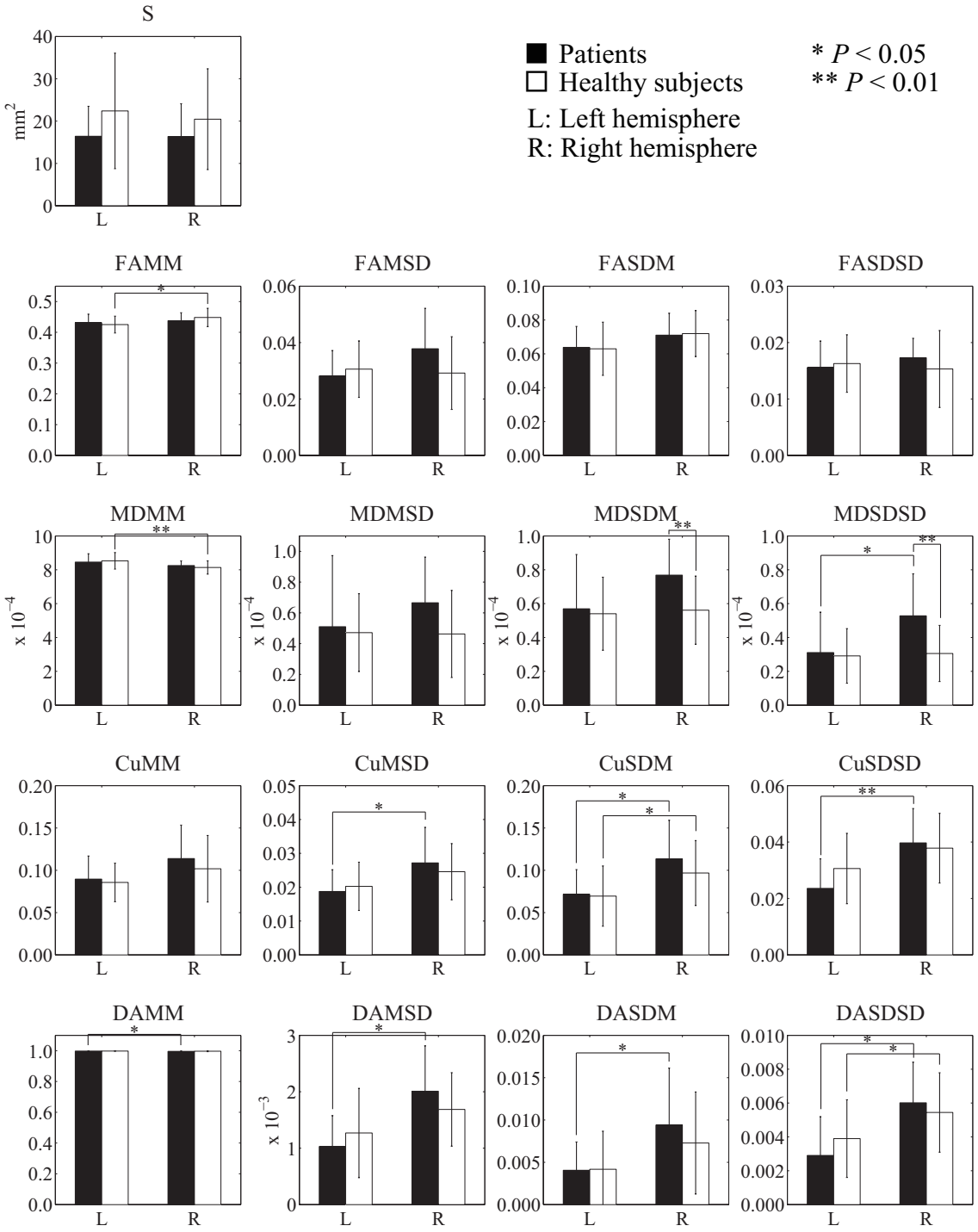

Figure 4.14: The bar plot of the mean value with the error bar of the standard deviation for all indices obtained through the fiber tracking of the sagittal stratum the specified ROI based on the unilateral fibers.

Table 4.3: The results of ANOVA for comparison of all analysis indices with group as between-group factor and hemisphere as within-subject factor for the sagittal stratum with the specified ROI based on the unilateral fibers.

Two-way ANOVA						
	Group effect		Hemisphere effect		Interaction	
Indices	$F(df = 1, 66)$	P value	$F(df = 1, 66)$	P value	$F(df = 1, 66)$	P value
S	3.345	0.072	0.132	0.717	0.118	0.732
FAMM	0.105	0.747	4.463	0.038	1.393	0.242
FAMSD	1.101	0.298	1.974	0.165	3.518	0.065
FASDM	0.000	0.994	5.386	0.023	0.062	0.803
FASDSD	0.224	0.638	0.082	0.775	1.010	0.319
MDMM	0.033	0.856	7.861	0.007	0.752	0.389
MDMSD	2.219	0.141	0.825	0.367	1.029	0.314
MDSDM	3.964	0.051	3.436	0.068	2.251	0.138
MDSDSD	5.860	0.018	5.341	0.024	4.092	0.047
CuMM	0.939	0.336	5.978	0.017	0.239	0.626
CuMSD	0.070	0.793	9.728	0.003	1.013	0.318
CuSDM	1.005	0.320	13.440	0.000	0.597	0.443
CuSDSD	0.732	0.395	15.000	0.000	2.185	0.144
DAMM	0.717	0.400	7.060	0.010	0.471	0.495
DAMSD	0.054	0.817	15.325	0.000	2.479	0.120
DASDM	0.561	0.456	10.002	0.002	0.704	0.405
DASDSD	0.131	0.719	15.792	0.000	1.778	0.187

tive evaluation of the abnormalities of schizophrenic patients. These two indices represent the mean and standard deviation of the mean diffusivity for all the tracked fibers in a hemisphere of the standard deviations in a single tracked fiber. The mean diffusivity indicates the diffusion volume, unrelated to the direction. It is believed that the dispersion of the brain tissue density may increase for all the tracked fibers when the standard deviation of the mean diffusivity is at a high level. The existence of the large values for these two indices in the patient group shows that the patients had more dispersion of the brain tissue density than the healthy comparison subjects for both each tracked fiber and all the tracked fibers. That is, it can be considered that dense and sparse areas for the fibers were intermixed in the patient right sagittal stratum. Furthermore, MDSDSD in the right hemisphere had a higher value than that in the left hemisphere in the patient group, whereas the healthy comparison group did not have a significant difference. This suggested that the MDSDSD value increased in the right hemisphere for the patient group.

The between-hemisphere analysis of FAMM showed significant differences in the healthy

Table 4.4: The results of t-tests separately examining fifteen indices between patient and healthy comparison subject groups and between left and right hemispheres for the sagittal stratum with the specified ROI based on the unilateral fibers.

t-test						
	Group effect (Patient - Healthy)					
	Left			Right		
Indices	t value	df	P value	t value	df	P value
S	1.469	33	0.151	1.103	33	0.278
FAMSD	0.711	33	0.482	1.797	33	0.081
MDSDM	0.312	33	0.757	2.831	33	0.008
MDSDSD	0.286	33	0.777	3.091	33	0.004
	Hemisphere effect (Left - Right)					
	Patient			Healthy		
Indices	t value	df	P value	t value	df	P value
FAMM	0.619	26	0.541	2.558	40	0.014
FAMSD	2.054	26	0.050	0.380	40	0.706
FASDM	1.460	26	0.156	1.934	40	0.060
MDMM	1.322	26	0.198	2.807	40	0.008
MDSDM	1.866	26	0.073	0.317	40	0.753
MDSDSD	2.273	26	0.031	0.279	40	0.781
CuMM	1.820	26	0.080	1.590	40	0.120
CuMSD	2.468	26	0.020	1.767	40	0.085
CuSDM	2.789	26	0.010	2.330	40	0.025
CuSDSD	3.624	26	0.001	1.840	40	0.073
DAMM	2.140	26	0.042	1.566	40	0.125
DAMSD	3.627	26	0.001	1.823	40	0.076
DASDM	2.566	26	0.016	1.845	40	0.072
DASDSD	3.377	26	0.002	2.108	40	0.041

comparison group but not in the patient group. Thus, it may show a difference between the patient and comparison groups. FAMM is the mean in all the tracked fibers of the means for a single tracked fiber. FA is an index of the anisotropy strength. The fibers align tightly in a fiber tract where FA has a large value. The right value was larger than the left in the healthy comparison group, which showed that the right sagittal stratum was running more densely than the left one. In the previous chapter, we described a reduction in S of the superior longitudinal fasciculus of schizophrenic patients, and that the right S was larger than the left S in the healthy comparison group [58]. S is an index that is proportional to the number of fibers tracked until the ending region. Thus, an increased S may reflect a high average fractional anisotropy along the tracked fibers. In this case, even though S did not show significant differences for the group effect and the hemisphere effect, suggesting connectivity abnormality in patients, the healthy group had significant differences between the hemispheres in FAMM, while the patient group did not.

For MDMM, the right value was smaller than the left one in the healthy group, in contrast to the results for FAMM. These observed facts were consistent. Because the mean diffusivity reflects the density of brain tissue, a high mean diffusivity may indicate rough tissue because water molecules can easily move in matter with rough tissue. Hence, these results suggest that the fiber tract in the right hemisphere is denser than that in the left one. On the other hand, the patient group did not have a hemisphere effect for MDMM. This suggests that the densities of the sagittal stratum tissues of bilateral hemispheres are almost equal.

The hemisphere effects for CuMSD and CuSDSD had significant differences in the patient group, whereas they did not have any in the healthy group. However, the indices tended to be different between the left and right hemispheres in the healthy comparison group. Hence, it is difficult to say that these indices had differences in the hemisphere effects between the groups and could be used as indices to quantitatively evaluate the abnormalities of patients. In addition, CuSDM had significant hemisphere differences for both groups. This index could also not be used as an index for the quantitative evaluation of the disease. Although the values of DAMSD, DASDM, and DASDSD of the patient group had the significant differences between hemispheres, they were not enough to evaluate the abnormality of the tract, since the values of the healthy comparison group also had the same difference or tendency between groups.

Therefore, in this case of the fiber tracking for the sagittal stratum with the specified ROI based on the unilateral fibers, it was shown that the indices of FAMM, MDMM, MDSDM, MDSDSD, and DAMM are efficient to evaluate the abnormalities of schizophrenic patients based on the differences between groups or between hemispheres of the values of the indices.

4.6.2 Superior longitudinal fasciculus

We show the tractographies with the specified ROI based on the unilateral fibers for the sagittal stratum in Figures 4.15 and 4.16. Figure 4.15 represents the results for the patient group, and Figure 4.16 indicates the results for the healthy comparison group. The mean value of all indices are plotted in Figure 4.17. We provide the table representing the results obtained from statistical analyses in Tables 4.5 and 4.6.

The ANOVA shew the significant hemisphere effect in the indices of S, FAMM, FASDM, MDMM, CuSDSD, and DASDSD, and the tendency of the significant hemisphere effect in the values of FAMSD and DASDM. We examined these eight indices by t-tests between hemispheres for the patient and healthy comparison groups separately.

The right value of S showed significantly large value compared to the left value in the healthy comparison group in the t-test, whereas the patient group did not show the hemisphere difference. We obtained the same results in the previous chapter in the case of the tracking for the superior longitudinal fasciculus with the specified ROI based on the bilateral fibers. Although this results were obtained when we selected the ROI with maximum number of tracked fibers in the previous chapter, we found the same features through the tracking with the uniquely specified ROI in the present chapter. The subject's images were normalized corresponding to the standard brain in the present chapter, whereas the subject's original images were analyzed in the previous chapter. It is considered that the selection of ROI with the maximum number may not be need to evaluate the abnormality of patient's S, when the images are normalized. However, the group factor did not show the significant effect in the examination by ANOVA in the present case.

The t-test shew the significant large values in the left hemisphere compared to those of the right hemisphere for FASDM, CuSDSD, and DASDSD in the healthy comparison group. However the patient group did not have any significant differences between hemispheres in the indices. The magnitude of FASDM reflect the inhomogeneity of the ordered structure along each trajectory tracked in the ROI. The superior longitudinal fasciculus of the healthy comparison in the left hemisphere may have more inhomogeneous micro-structure compared to the right one.

The left MDMM was larger than the right one in both groups. These results coincide with the results in the previous chapter. The degree of MDMM reflects the density of the tissue in the tract. It is considered that the right superior longitudinal fasciculus has thick density compared to the left one independent of the group.

Therefore, when we performed the fiber tracking of the superior longitudinal fasciculus, it was shown that the value of S, FASDM, CuSDSD, and DASDSD might characterize the abnormalities of the schizophrenic patients.

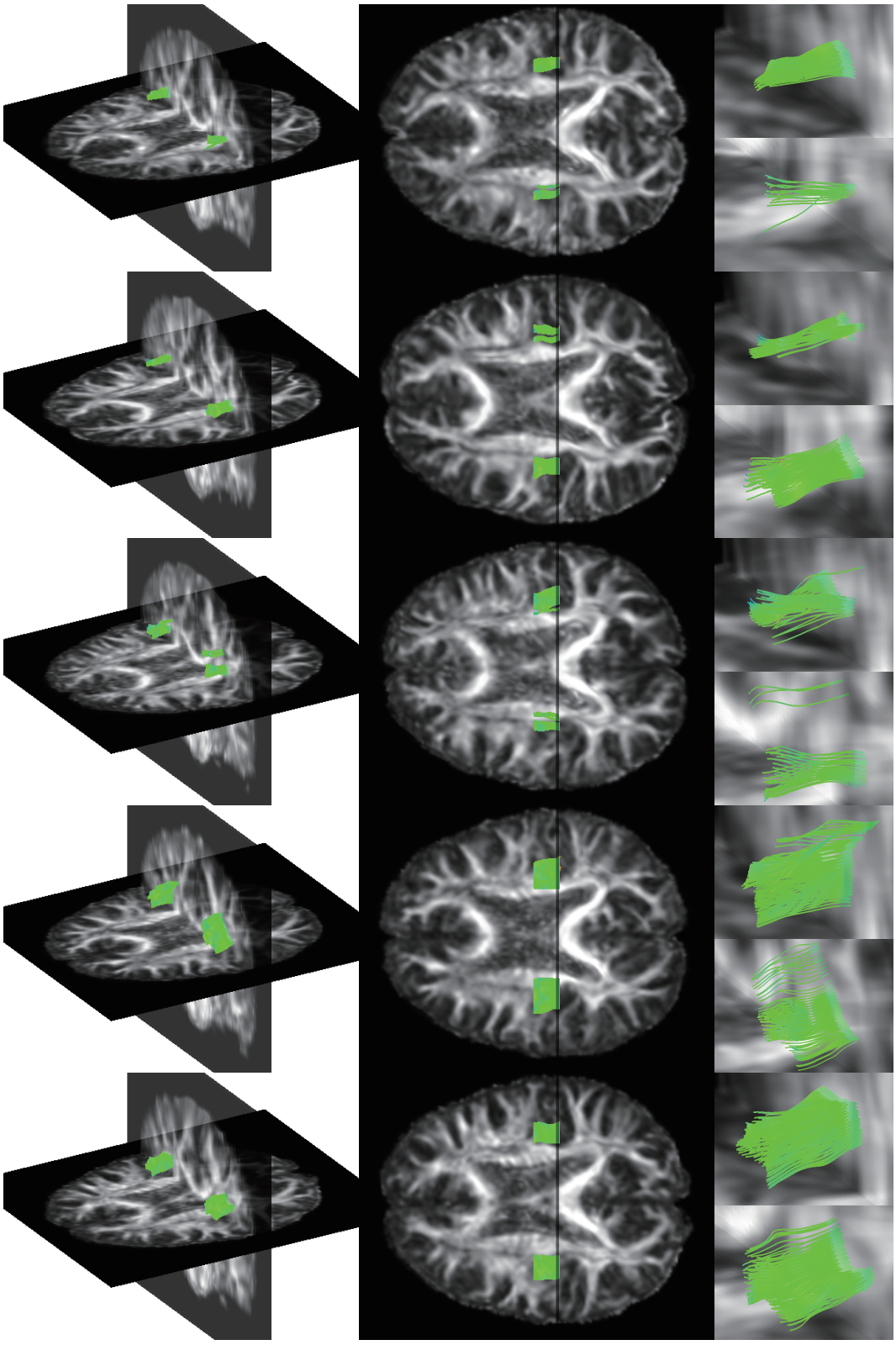

Figure 4.15: The tractography of the superior longitudinal fasciculus for the patient group.

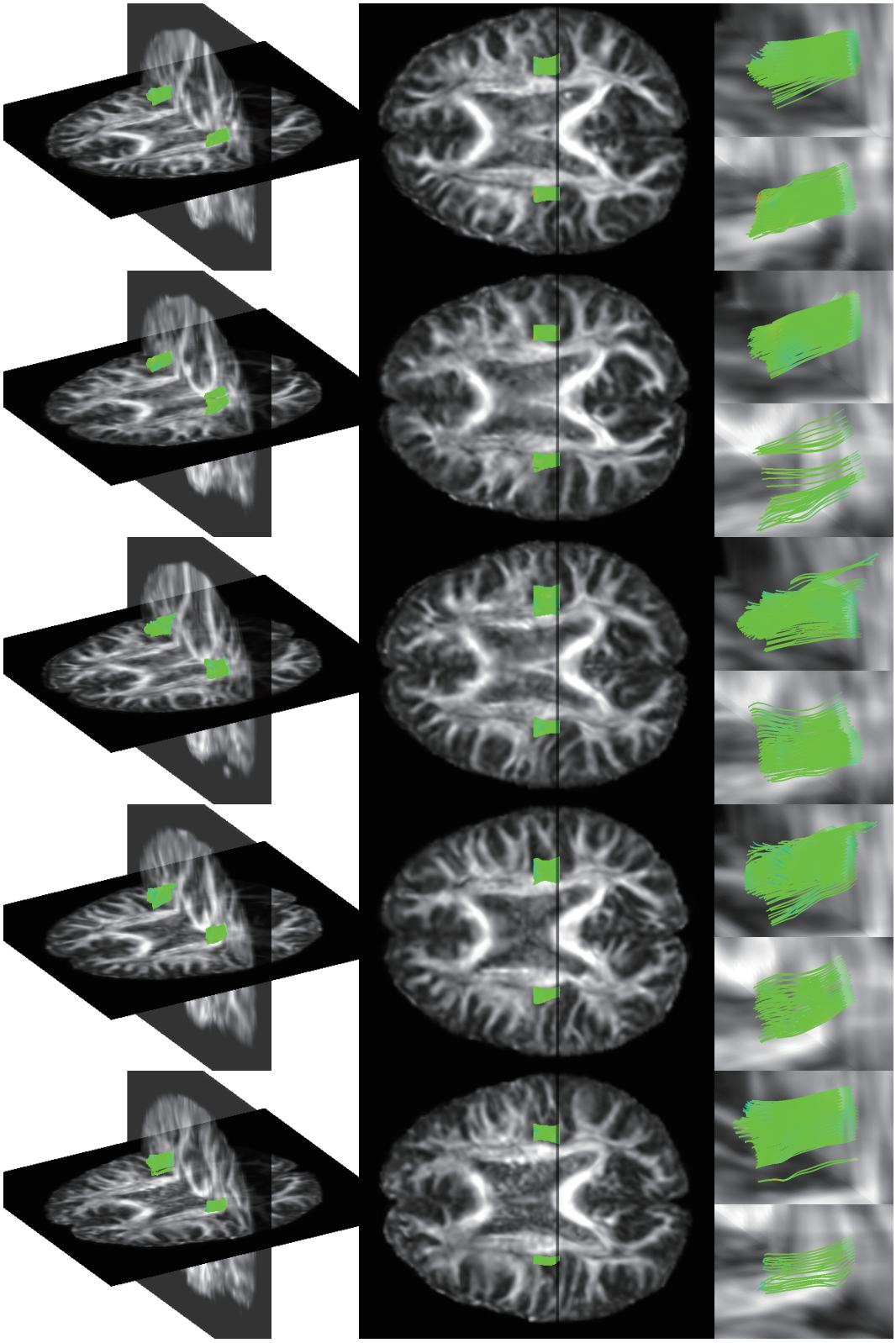

Figure 4.16: The tractography of the superior longitudinal fasciculus for the healthy comparison group.

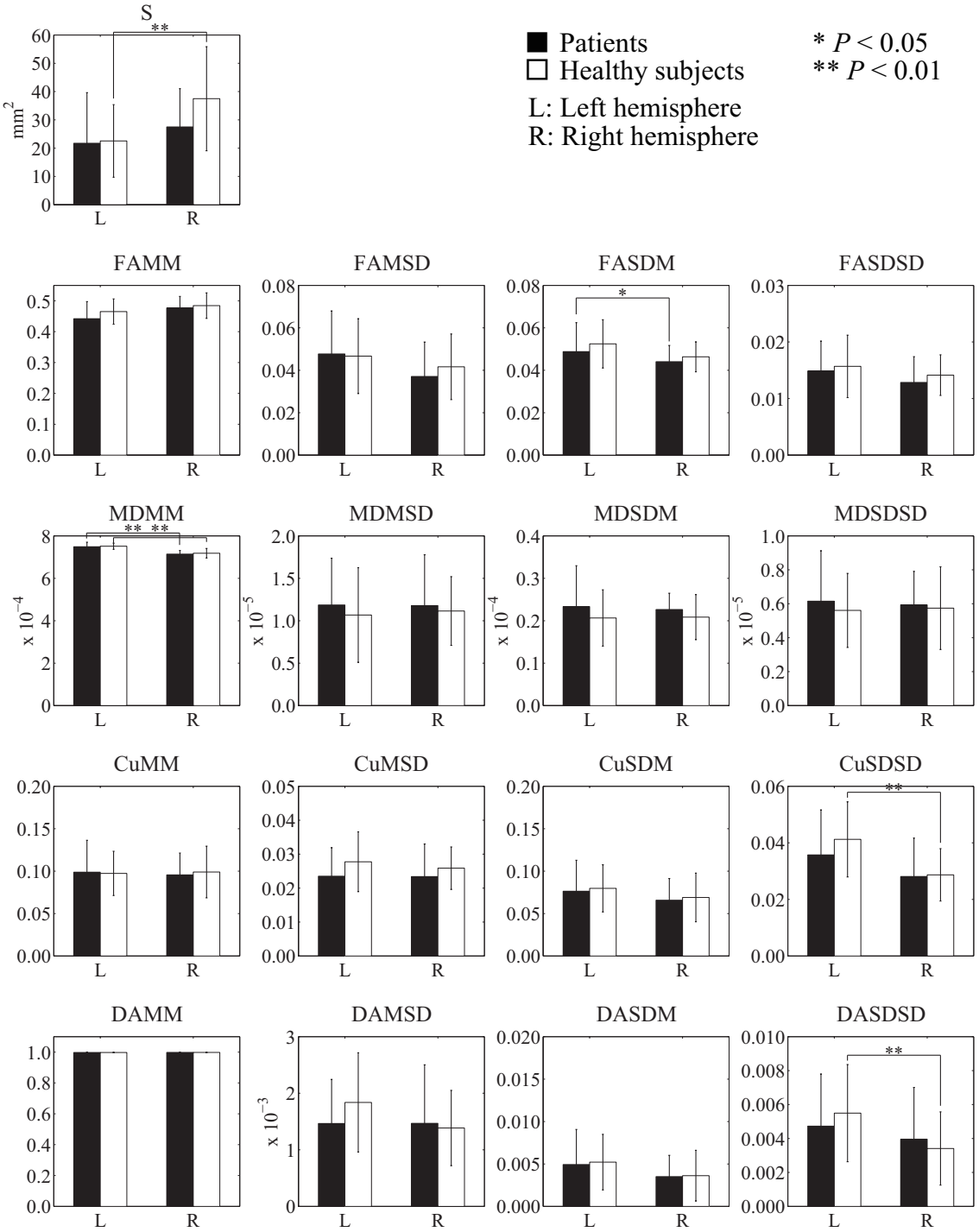

Figure 4.17: The bar plot of the mean value with the error bar of the standard deviation for all indices obtained through the fiber tracking of the superior longitudinal fasciculus.

Table 4.5: The results of ANOVA for comparison of all analysis indices with group as between-group factor and hemisphere as within-subject factor for the superior longitudinal fasciculus.

Two-way ANOVA						
	Group effect		Hemisphere effect		Interaction	
Indices	$F(df = 1, 66)$	P value	$F(df = 1, 66)$	P value	$F(df = 1, 66)$	P value
S	1.843	0.179	6.734	0.012	1.319	0.255
FAMM	1.994	0.163	5.962	0.017	0.490	0.487
FAMSD	0.166	0.685	3.227	0.077	0.408	0.525
FASDM	1.348	0.250	4.527	0.037	0.071	0.790
FASDSD	0.778	0.381	2.219	0.141	0.039	0.843
MDMM	0.444	0.508	49.436	0.000	0.027	0.870
MDMSD	0.480	0.491	0.024	0.878	0.042	0.839
MDSDM	1.828	0.181	0.022	0.882	0.074	0.786
MDSDSD	0.373	0.544	0.005	0.945	0.086	0.770
CuMM	0.015	0.901	0.011	0.916	0.100	0.752
CuMSD	2.652	0.108	0.234	0.630	0.182	0.671
CuSDM	0.197	0.659	2.073	0.155	0.000	0.995
CuSDSD	0.875	0.353	9.700	0.003	0.575	0.451
DAMM	0.010	0.922	0.748	0.39	0.021	0.885
DAMSD	0.476	0.493	1.141	0.289	1.168	0.284
DASDM	0.060	0.808	3.414	0.069	0.011	0.916
DASDSD	0.023	0.879	4.238	0.043	0.905	0.345

Table 4.6: The results of t-tests separately examining eight indices between patient and healthy comparison subject groups and between left and right hemispheres for the superior longitudinal fasciculus.

t-test						
	Hemisphere effect (Left - Right)					
	Patient			Healthy		
Indices	t value	df	P value	t value	df	P value
S	0.927	26	0.363	2.974	40	0.005
FAMM	1.859	26	0.074	1.471	40	0.149
FAMSD	1.471	26	0.153	0.96	40	0.343
FASDM	1.094	26	0.284	2.034	40	0.049
MDMM	4.506	26	0.000	5.542	40	0.000
CuSDSD	1.315	26	0.200	3.465	40	0.001
DASDM	1.061	26	0.299	1.611	40	0.115
DASDSD	0.639	26	0.528	2.6	40	0.013

4.7 Discussion

In this chapter we described the method to construct ROI for the fiber tracking automatically by use of the segmentation map of the human cerebrum. The findings in the present chapter illustrated the significant differences between the patient and healthy comparison groups and between the left and right hemispheres in the sagittal stratum and the superior longitudinal fasciculus obtained from the fiber tracking and tractography.

When we applied the uniquely specified ROI for the fiber tracking of the sagittal stratum, we obtained the difference between groups in the left hemisphere, whereas the difference was not shown in the fiber tracking with the ROI specified by the maximum number of tracked fibers. Since the number of tracked fibers increased for almost all subjects in the tracking with the specified ROI based on the unilateral fibers, the difference of S between groups might not be detected.

The behavior of the indices of MDMM and MDSDM was the same in both cases of ROI. It implies the feature that the density of the tissue can be detected even if the number of the tracked trajectories is different. The values of MDSDM had the significant difference between groups in the right hemisphere and the significant difference between hemispheres in the patient group in the condition of the selected ROI based on the maximum number of trajectories. Although the significant differences were not observed in the process with the uniquely specified ROI, the same tendency was shown in the t-tests. The entire inhomogeneity of the density of tissues can be concluded high in the right sagittal stratum of the patients.

The large value of FAMM in the right hemisphere of the healthy group was observed only in the case with the selected ROI by the maximum number of the trajectories. Although this results was not obtained in the case of the unique ROI, the differences between hemisphere MDMM, which coincided the hemisphere effect for FAMM, were observed in both situation of ROIs. These findings imply that the degree of the integrity of tissues in the sagittal stratum can be detected in both cases of ROI.

We obtained the difference of DAMM between hemispheres in the patent group when the selected ROI was applied, whereas the detection was not established in the tracking with the unique ROI. Since the magnitude of DAMM reflects the shape of the tracked trajectory, the left sagittal stratum is considered to be relatively curved in the patient group when a large number of the fibers were tracked.

In the tracking of the superior longitudinal fasciculus, the value of S had the significant difference between hemispheres in the healthy comparison group corresponding to the result in the previous chapter. The observation that the healthy group had the difference between hemispheres and the patient group did not have the difference denoted that the index S might be effective to evaluate the abnormality in the superior longitudinal

fasciculus. The significant differences associated with S were observed in both of the cases of the tracking for the sagittal stratum and the superior longitudinal fasciculus. In addition, the abnormality of patient's S was reported in the left anterior thalamic peduncle [66]. It implies the value of S is reliable index to evaluate the abnormality in the multiple tracts.

The values of FASDM, CuSDSD, and DASDSD, which shew the significant differences between hemispheres in the healthy group for the superior longitudinal fasciculus, did not show any significant differences in the analysis for the sagittal stratum. These observations imply the difference of the microstructural and structural features of the two tracts in the healthy comparison subject.

We constructed the ROI through automatic processes in this chapter. In this construction of ROI, the starting area for the fiber tracking was restricted in the area, where the segment for the targeted bundles of the parcellation map corresponding to the standard brain. This automatic ROI construction reduced the quantity of work significantly since it did not require to set the starting and ending regions for subjects one by one and to eliminate untargeted bundles from the tracking results manually with the tractographies.

In addition, this construction improved the reproducibility in comparison to the method described in the previous chapter suffered from the arbitrariness. The features of the extracted values characterizing the targeted nerve fibers with the proposed ROI construction method supported the previously reported results. The results of this chapter suggest that the proposed method are appropriate for the evaluation of the abnormalities in the nerve fibers of schizophrenic patients. Consequently, the proposed construction method is feasible to characterize the tracked fibers in order to evaluate the abnormalities in the fibers of schizophrenic patients.

Chapter 5

Interpolation for crossing area of fibers

We focused on the inherent problem in performance of the fiber tracking in this chapter. When the multiple tracts cross in the white matter, the fiber tracking jumps to the adjacent untargeted bundle frequently. Although nerve tracts do not cross in the area where only a single nerve bundle exists, the bundles often cross around areas where multiple tracts exist adjacently such as the white matter close to the cortex. If the tracking is propagated to the unrelated tract, we cannot surely extract the feature of the targeted bundle and depict the desirable tractography of the bundle. We propose a method that the fiber tracking skips the unrelated tract and interpolate the trajectory in an area where we assess multiple bundles cross during the fiber tracking on the targeted bundle. The efficiency of the proposed method is verified with the simulation data corresponding to the white matter in the human brain.

5.1 Model for simulation

We create the data sets for the simulation modeling three nerve bundles in the human cerebrum. The three bundles shown in Figure 5.1 on the color map are referenced for the model of the simulation data. This image represents the posterior right area on the axial slice. The yellow rectangle labeled by CC represents the central part of the corpus callosum, and the other labeled as V5 indicates the fifth visual cortex. We focus on the bundle passing from the corpus callosum to the fifth visual cortex (Fiber 1) for the fiber tracking. Two principal bundles cross the targeted bundle. One is a bundle connecting the frontal lobe and the occipital lobe including the primary visual cortex (Fiber 2) and another is a part of the superior longitudinal fasciculus (Fiber 3). Fibers 1 and 2 lie in parallel with the axial plane, whereas Fiber 3 passes perpendicularly to the axial plane. We construct the simulation data based on the shapes of these three nerve bundles.

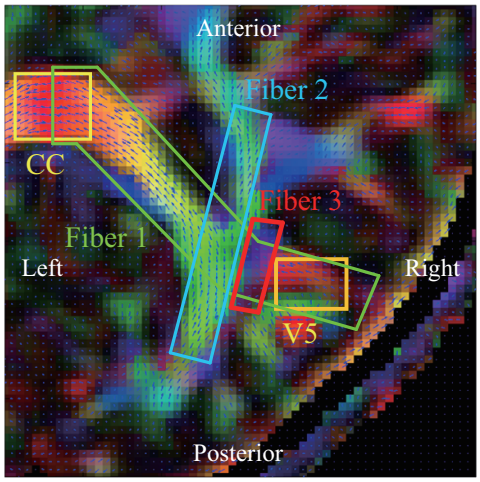

Figure 5.1: Three crossing tracts modeled for the simulation. (Fiber 1) The targeted nerve bundle from the corpus callosum (CC) to the fifth visual cortex (V5). (Fiber 2) The tract from the frontal cortex to the primary visual cortex. (Fiber 3) A part of the superior longitudinal fasciculus.

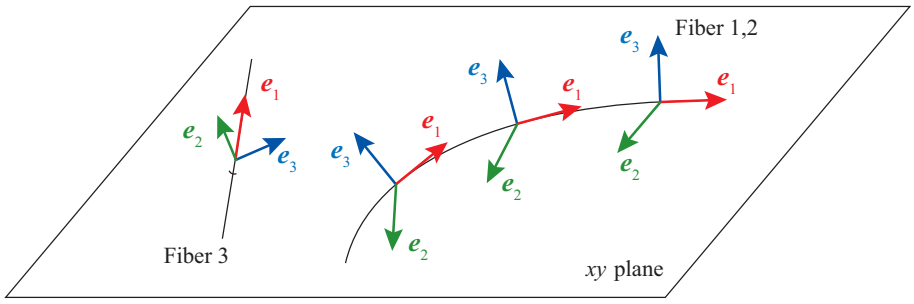

Figure 5.2: The schematic diagram of the directions of the eigenvectors for Fibers 1 and 2 (right) and for Fiber 3 (left).

5.2 Simulation data

We construct two simulation data sets, which are the straight model and the curved model. The two-dimensional schematic diagrams of the modeled tracts on the xy plane; i.e. the axial plane, are shown in Figure 5.3 although the actual data sets are three-dimensional data. The shapes of Fiber 1 in the crossing area are different in the two models. In the straight model, the entire shape of Fiber 1 is straight, whereas a part of Fiber 1 bends in the curved model. The width of Fibers 1 and 2 in the xy plane is 6 mm, and that of Fiber 3 is 4 mm. The depth of the three fibers along the z axis is 6 mm. The signal intensities of the fiber bundles and the other areas in the $b0$ images are defined as 1200 and 1700, respectively. These values correspond to the intensities in the white and gray matters

of actual measurements in the human brain. A voxel size is $1.00 \times 1.00 \times 1.00$ mm^3, an image matrix is $192 \times 192 \times 38$, and the fiber bundles exist in six slices of $12 \leq z \leq 17$.

The eigenvalues and eigenvectors in each voxel are constructed based on an actual measured image with DTI. The tangent vector of the trajectory of each bundle is determined as the first eigenvector $\boldsymbol{e}_1$, the second eigenvector $\boldsymbol{e}_2$ that has a z component of 0 such as orthogonal vector to the first eigenvector, and the third eigenvector crossed orthogonally to both of $\boldsymbol{e}_1$ and $\boldsymbol{e}_2$. The schematic diagram of the directions of the eigenvectors for the three tracts is shown in Figure 5.2. The first eigenvector $\boldsymbol{e}_1$ and the second eigenvector $\boldsymbol{e}_2$ for Fiber 1 and Fiber 2 lie on the xy plane, and the third eigenvector $\boldsymbol{e}_3$ points to the z axis. The direction of $\boldsymbol{e}_1$ for Fiber 3 is almost along the z axis. This direction is corresponding to the orientation of this fiber in the actual image. The second eigenvector $\boldsymbol{e}_2$ for Fiber 3 is on the xy plane.

The ratios of the three eigenvalues are set as $\lambda_1 : \lambda_2 : \lambda_3 = 7 : 3 : 2$ (FA $= 0.58$) in Fiber 1; $\lambda_1 : \lambda_2 : \lambda_3 = 10 : 3 : 2$ (FA $= 0.71$) in Fiber 2; $\lambda_1 : \lambda_2 : \lambda_3 = 9 : 3 : 2$ (FA $= 0.68$) in Fiber 3; and $\lambda_1 : \lambda_2 : \lambda_3 = 23 : 17 : 17$ (FA $= 0.18$) in the other area. We employ the mean diffusivity MD $= (\lambda_1 + \lambda_2 + \lambda_3)/3 = 0.80 \times 10^{-3}$mm^2/s, which corresponds to the degree of the mean diffusivity in the cerebral parenchyma of actual images obtained from DTI. In the area where multiple tracts cross each other, the diffusion tensor is averaged over the diffusion tensors of the crossing bundles. The components of the diffusion tensor are calculated from the values of eigenvectors and eigenvalues as

$$\overline{\mathbf{D}} = \begin{pmatrix} D_{xx} & D_{xy} & D_{zx} \\ D_{xy} & D_{yy} & D_{yz} \\ D_{zx} & D_{yz} & D_{zz} \end{pmatrix} = \begin{pmatrix} \boldsymbol{e}_1 & \boldsymbol{e}_2 & \boldsymbol{e}_3 \end{pmatrix} \begin{pmatrix} \lambda_1 & 0 & 0 \\ 0 & \lambda_2 & 0 \\ 0 & 0 & \lambda_3 \end{pmatrix} \begin{pmatrix} \boldsymbol{e}_1^{\mathrm{T}} \\ \boldsymbol{e}_2^{\mathrm{T}} \\ \boldsymbol{e}_3^{\mathrm{T}} \end{pmatrix}. \tag{5.1}$$

Subsequently, we create MR-DTI data sets with MPG along six independent directions and a $b0$ image based on the above parameter settings. The orientations of the MPGs are $[1, 1, 0]$, $[1, 0, 1]$, $[0, 1, 1]$, $[-1, 1, 0]$, $[1, 0, -1]$, $[0, -1, 1]$. The components of the MPGs are scaled, so that the magnitude of the vector is normalized. The b value of the DTI is 1000s/mm^2. We calculate the intensities of DTI images in each voxel using the values of b and $\overline{\mathbf{D}}$ with Equation (2.38).

In addition, we superpose some noise on the DTI data corresponding to the images of the real human brain. Since some noise cannot be removed from images in the actual imaging, we imitate the actual images. The signal-to-noise ratio (SNR) in this study corresponds to the ratio between the mean signal intensity of a part of the cerebral parenchyma and the intensity of the background in the outside of the brain. The value of SNR in the actual $b0$ image is around 300. We apply the SNR to be 300, 100, and 50 in order to evaluate the dependence of SNR. We employ the white Gaussian noises with the mean of 0 and a standard deviation of 4.0, 12.0, and 24.0 for the SNRs of 300, 100, and 50, respectively since the signal intensity of the $b0$ image is 1200 in this study.

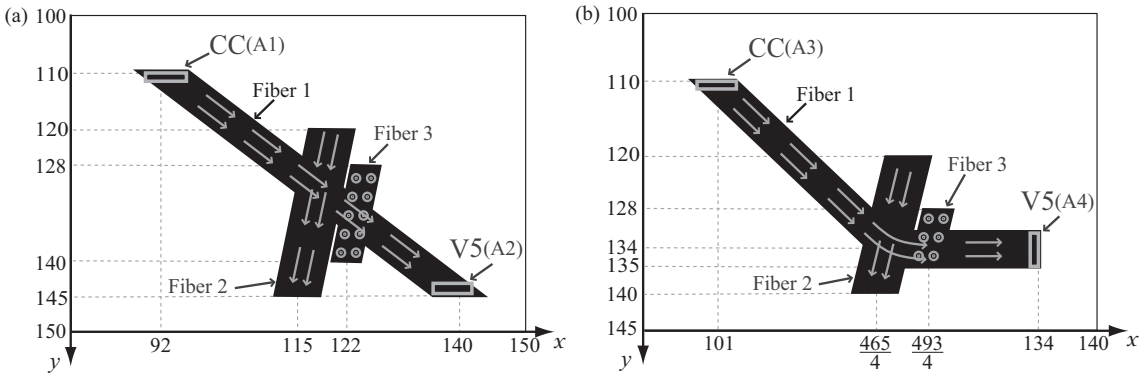

Figure 5.3: The schematic diagrams for the simulation illustrating three nerve tracts. (a) The straight model and (b) the curved model.

5.2.1 Straight model

In the straight model, the targeted bundle has an entirely straight shape in the crossing area. The width of Fibers 1 and 2 is 6 mm and the width of Fiber 3 is 4 mm around the center lines on the xy plane. The depth of all tracts are set as 6 mm along the z axis. The three tracts have fields around the central lines described as follows.

$$\text{Fiber1} \quad \begin{pmatrix} x \\ y \end{pmatrix} = \begin{pmatrix} 4 \\ 3 \end{pmatrix} s + \begin{pmatrix} 92 \\ 110 \end{pmatrix} (0 \le s \le \frac{35}{3}) \tag{5.2}$$

$$\text{Fiber2} \quad \begin{pmatrix} x \\ y \end{pmatrix} = \begin{pmatrix} 1 \\ -4 \end{pmatrix} t + \begin{pmatrix} 115 \\ 145 \end{pmatrix} (0 \le t \le \frac{25}{4}) \tag{5.3}$$

$$\text{Fiber3} \quad \begin{pmatrix} x \\ y \end{pmatrix} = \begin{pmatrix} 1 \\ -4 \end{pmatrix} u + \begin{pmatrix} 122 \\ 140 \end{pmatrix} (0 \le u \le 3). \tag{5.4}$$

The fiber's orientations in the fields are parallel to the directions of the central lines in Fibers 1 and 2; i.e., the direction vectors for the two tracts are $[4, 3, 0]$ and $[1, -4, 0]$, and the first eigenvectors are established as $[0.800, 0.600, 0]$ and $[0.243, -0.970, 0]$, respectively. The direction of the tract in Fiber 3 is set as $[1, -4, 20]$ corresponding to the first eigenvector $[0.049, -0.196, 0.979]$.

The schematic diagram of the straight model is shown in Figure 5.3 (a). The black areas represent the fields of the fiber tracts and the gray arrows indicate the direction of the fibers. Both edges are labeled as CC indicating the corpus callosum and V5 representing the fifth visual cortex, which are denoted as the starting areas A1 and A2 for the fiber tracking. The starting areas are established in the areas of $91 \le x \le 96$, $110 \le y \le 111$, $13 \le z \le 15$ (A1) and $136 \le x \le 141$, $143 \le y \le 144$, $13 \le z \le 15$ (A2) in the straight model. The number of seed points for tracking is 165 since the dispersion rate of seed points is 4 points/mm^2. The ending region is determined as the opposite side of the starting area in Fiber 1; i.e., the ending region is A2 when the starting area is A1.

5.2.2 Curved model

The targeted bundle is curved with the radius of 10 mm having a central angle 45° in the curved model. The shapes and orientations of Fibers 2 and 3 are the same as those in the case of the straight model. The ranges of the two tracts are set as $5/4 \leq t \leq 25/4$ and $5/4 \leq u \leq 3$ in Equations (5.3) and (5.4). The central line of Fiber 1 is determined by the following equations.

$$\begin{pmatrix} x \\ y \end{pmatrix} = \begin{pmatrix} -1 \\ 0 \end{pmatrix} s + \begin{pmatrix} 134 \\ 134 \end{pmatrix} \ (0 \leq s \leq 10) \tag{5.5}$$

$$\text{Fiber1} \quad \begin{pmatrix} x \\ y \end{pmatrix} = 10 \begin{pmatrix} -\sin\theta \\ \cos\theta \end{pmatrix} + \begin{pmatrix} 124 \\ 124 \end{pmatrix} \ (0 \leq \theta \leq 45°) \tag{5.6}$$

$$\begin{pmatrix} x \\ y \end{pmatrix} = \begin{pmatrix} -16 \\ -21 \end{pmatrix} s + \begin{pmatrix} 117 \\ 131 \end{pmatrix} \ (0 \leq s \leq 1). \tag{5.7}$$

The direction of the first eigenvector is established along the central line at each stage of Fiber 1. The schematic diagram of this curved model is shown in Figure 5.3 (b). The two areas at both edges denotes the starting region A3 corresponding to CC and the starting area A4 coinciding with V5. The ranges of each starting area are $98 \leq x \leq 102$, $110 \leq y \leq 111$, $13 \leq z \leq 15$ (A3) and $133 \leq x \leq 134$, $132 \leq y \leq 136$, $13 \leq z \leq 15$ (A4) in the curved model. The number of the seed points dispersed in the starting region for tracking is 135 in the curved model.

5.3 Tracking method

In the proposed method, the fiber tracking is performed in the following procedures.

1. The ordinary tracking is performed from a seed point.

2. In an area where the condition of the tracking matches with the searching criteria and the tracking is assumed to approach the crossing unrelated bundle, searching for the trajectory is started.

3. We establish the area to search the resumption point around the area where searching is performed, and disperse points to resume the ordinary tracking in the area.

4. The trajectory is interpolated by information of the tracked line after the skipping of the untargeted tract.

5. We calculate several values characterizing the interpolated trajectory at several points arranged on the trajectory.

6. We select a single interpolated trajectory with the strongest likelihood as the tract connecting before and after the crossing area, on the basis of the calculated value for all trajectories corresponding to the resumption points.

7. The ordinary tracking starts again from the uniquely determined resumption point in the searching area.

We provide the ways to perform these procedures in due order in this section.

5.3.1 Fiber tracking in non-crossing area

First, seed points are dispersed evenly in the starting region. The dispersion rate is 4 points/mm^2; i.e., starting points are dispersed at intervals of 0.5 mm. The direction of tracking at each tracking point is determined by the TEND method described in the section 2.4. The step width, which is the distance between the present stepping point and the next stepping point, is set at 0.5 mm, which corresponds to a half value of the voxel size. The stepping point proceeds to the next tracking point via a Runge-Kutta stepping scheme of the forth order. The diffusion tensor at the tracking point is determined by interpolation using the diffusion tensor data of the nearest eight voxels around the stepping point.

Fiber tracking is terminated when the FA value at the stepping point is lower than the threshold value for the terminal criteria, or when the deflected angle exceeds 45°. The threshold value of FA is determined with the histogram of the FA value for each data set. We show the histograms of the FA value for the data set of the straight model with SNR = 50 in Figure 5.4. The left histogram represents the FA values in the tract's area, and the right one describes the other areas in the image for the simulation. We transform the histogram to the probability distribution. We define the FA threshold as a $\mathrm{FA}_{\mathrm{ter}}$ such that the total probability from $\mathrm{FA}_{\mathrm{ter}}$ to 1 in the tract's probability distribution and the summation of the probability from 0 to $\mathrm{FA}_{\mathrm{ter}}$ in the other probability distribution are the same value. The FA value for the threshold is different in each simulation image. We show the value of $\mathrm{FA}_{\mathrm{ter}}$ for the straight model with SNR = 50 in Figure 5.4.

5.3.2 Searching area

In the crossing area of multiple fibers, the FA value is assumed to be a small value since the multiple directions of the diffusion of water molecules are mixed. In Figure 5.5, the diffusion ellipsoid in a voxel including a single tract has an elongate shape (a), whereas two diffusion ellipsoids corresponding to two tracts are mixed and cause a low anisotropy (b). We begin to apply the proposed method to a stepping point which is a single step before the stepping point where the FA value is lower than the threshold value $\mathrm{FA}_{\mathrm{sch}}$.

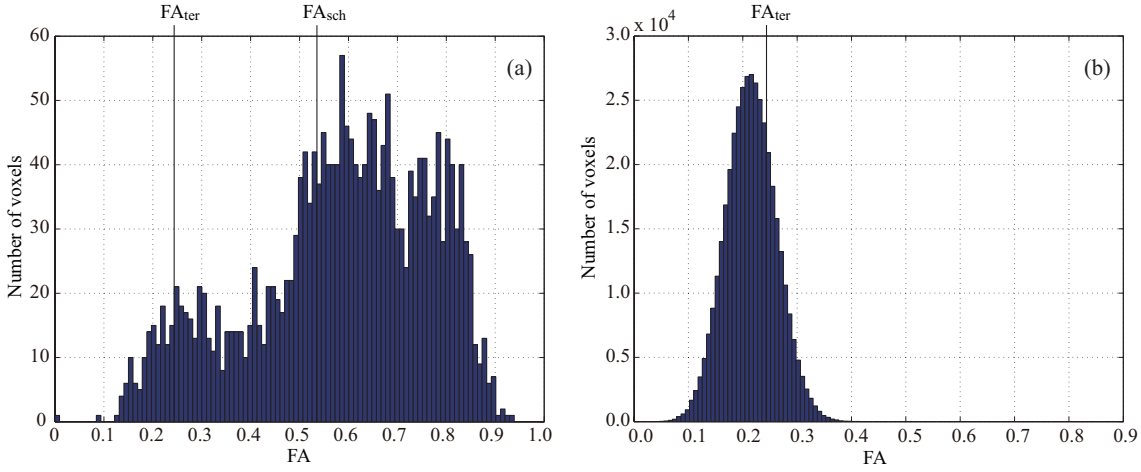

Figure 5.4: The histograms of the FA value in the tract's area (a) and the other areas (b) for the straight model with SNR = 50. Threshold FA_{ter} represents the threshold of the FA value for the terminal criteria of the fiber tracking. Threshold FA_{sch} indicates the threshold for the searching criteria.

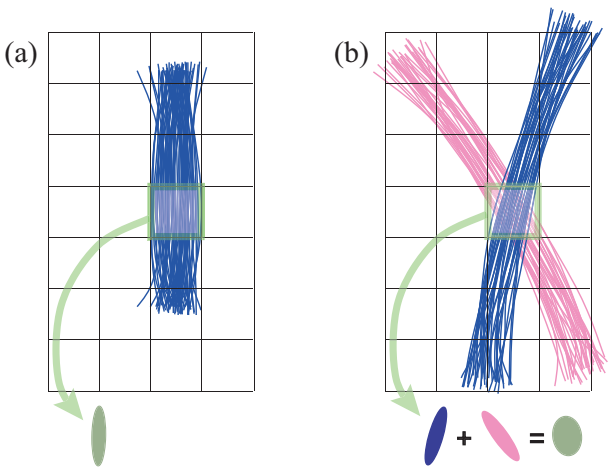

Figure 5.5: (a) A single tract exists in a voxel. (b) Two tracts exist in a single voxel.

The threshold value is the FA value where an accumulation is 20 % from 0 to the FA value in the histogram of the existing probability in the whole fiber bundles (Figure 5.4 (a)). As illustrated in Figure 5.6 (a), the ordinary tracking is performed to the blue point, which represents the present stepping point. The FA value in the blue point is less than the threshold value $\mathrm{FA}_{\mathrm{sch}}$. Then we establish the previous point s as a point to start searching for the resumption point, and the direction vector $\boldsymbol{v}_s$ from the point which is two points before the present point to the previous point s as the central vector of the area for searching.

The area to search for the resumption point is established as a part of a sphere from 5 mm to 20 mm radius from the point s at which the application of this method is begun. The range of the central angle of the area around the direction vector $\boldsymbol{v}_s$ is less than 30°. The resumption points are dispersed in the searching area. The interval among the resumption points along the vector $\boldsymbol{v}_s$ is 1 mm corresponding to the length of the two steps (Figure 5.6 (b)). The interval of the angle θ_t deflected from $\boldsymbol{v}_s$ (c) is determined on the basis of the distance from s, and the interval of the angle θ_r around $\boldsymbol{v}_s$ (d) is specified on the basis of both the distance from s and the angle θ_t in order to disperse the resumption points almost evenly. The number of steps from s along $\boldsymbol{v}_s$ corresponding to the distance is

$$l = 2L \quad (5 \leq L \leq 20), \tag{5.8}$$

where L is an integer. The angles θ_t and θ_r are

$$\theta_t = 30^\circ \times \frac{4}{l}, \quad \theta_r = \frac{360^\circ}{3l\theta_t}. \tag{5.9}$$

We define the orthogonal vectors $\boldsymbol{v}_1$ and $\boldsymbol{v}_2$ related to $\boldsymbol{v}_s$ as

$$\boldsymbol{v}_1 = \frac{[-\boldsymbol{v}_s(y)/\boldsymbol{v}_s(x), 1, 0]}{|[-\boldsymbol{v}_s(y)/\boldsymbol{v}_s(x), 1, 0]|}, \quad \boldsymbol{v}_2 = \frac{\boldsymbol{v}_s \times \boldsymbol{v}_1}{|\boldsymbol{v}_s \times \boldsymbol{v}_1|}. \tag{5.10}$$

The position vector of the resumption point $\boldsymbol{p}$ in the area for searching is then described as

$$\boldsymbol{d}_1 = \cos(r\theta_r)\boldsymbol{v}_1 + \sin(r\theta_r)\boldsymbol{v}_2 \quad (0 \leq r \leq \frac{360^\circ - \theta_r}{\theta_r}) \tag{5.11}$$

$$\boldsymbol{d}_2 = \boldsymbol{v}_s + \tan(t\theta_t)\boldsymbol{d}_1 \quad (0 \leq t \leq \frac{30^\circ}{\theta_t}) \tag{5.12}$$

$$\boldsymbol{p} = \boldsymbol{s} + 2l\boldsymbol{d}_2, \tag{5.13}$$

where t and r are integers, and $\boldsymbol{s}$ indicates the position vector at s. The dispersed resumption points are plotted by blue points in Figure 5.6 (e), and the total number of the points is 2354. Each parameter is defined through trial and error method in order to disperse the resumption points evenly and densely enough.

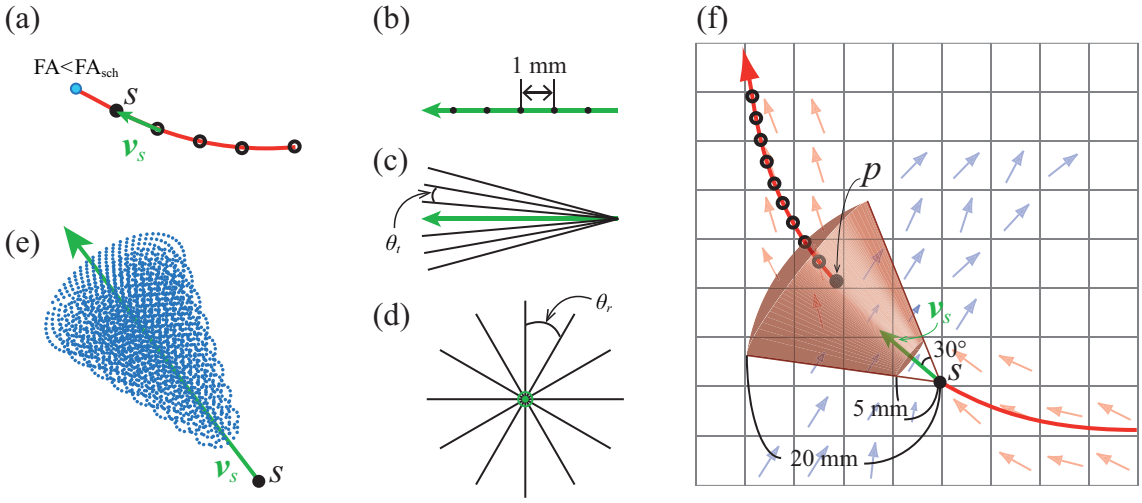

Figure 5.6: (a) The setting of the point s to start searching on the basis of the FA value at the present point. The central vector $\boldsymbol{v}_s$ for the area to search is the direction vector from the point two step before the present point to the previous point s. (b) The interval between resumption points along the central vector $\boldsymbol{v}_s$. (c) The interval angle θ_t deflected from $\boldsymbol{v}_s$. (d) The interval angle θ_r around the vector $\boldsymbol{v}_s$. (e) The three-dimensional plot of resumption points. (f) The definition of the region for searching in the crossing area. The point p represents the resumption point in the area for searching.

We show the schematic diagram of the area for searching of the resumption points in Figure 5.6 (f). The grid represents the boundary line between voxels, and small arrows indicate the direction of the first eigenvector in voxels. Red and blue arrows describe two different tracts. The tracking is propagated from the lower right side of the picture, the point s to start searching is assigned at the black point, and the pink area represents the area to search the resumption points. A resumption point is labeled as p with the position vector $\boldsymbol{p}$.

5.3.3 Interpolation

We disperse the resumption points throughout the area for searching, calculate the FA value at each resumption point, and choose a point p that has a larger value of FA than $\mathrm{FA}_{\mathrm{sch}}$. At the point we calculate the first eigenvector, and assign that to the direction vector from p to the next stepping point. The direction of the first eigenvector or the opposite orientation is selected so that the deflected angle between $\boldsymbol{v}_s$ and the direction at p. The ordinary tracking is performed for 10 steps from the resumption point. If the tracking ends before it is performed for 10 steps, we exclude the point p from the probable points as the resumption points. We establish the direction vector $\boldsymbol{v}_p$ from the resumption point p to the next point.

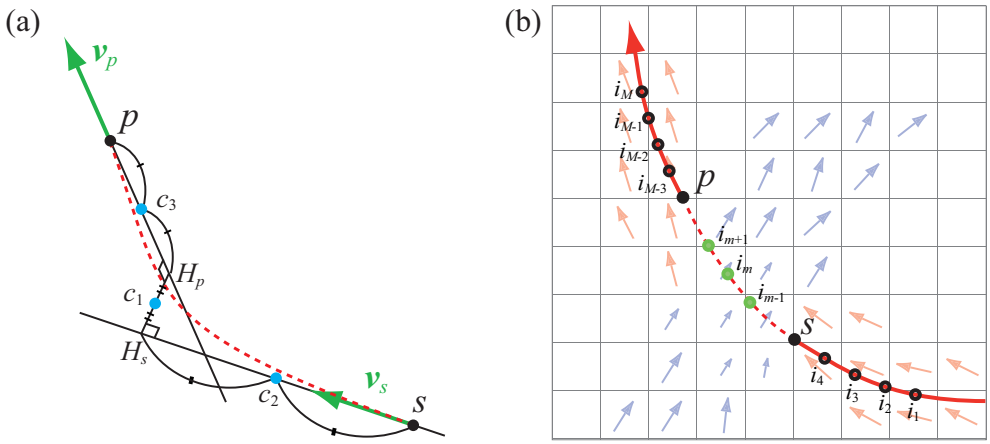

Figure 5.7: (a) The definition of three control points. (b) The stepping points on the interpolated curve and the trajectories before and after the interpolation.

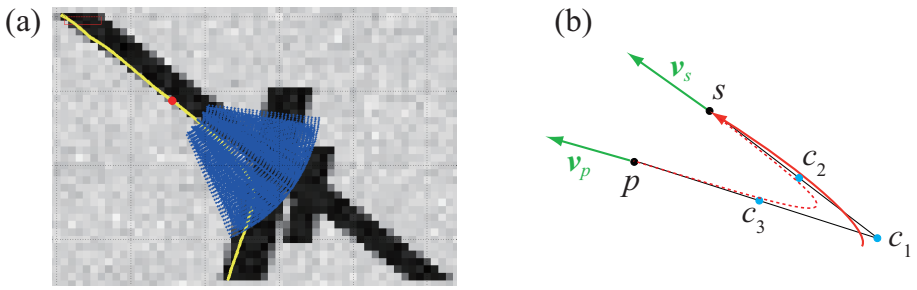

Figure 5.8: (a) The tractography in the simulation data with the straight shape in the case of failed interpolation. The tracking is performed from the upper left and propagated along the yellow line. The area for searching does not cover whole crossing area since the point s (red point) is far from the crossing area. (b) The schematic diagram of the interpolated trajectory when the interpolation is performed unsmoothly.

We determine three control points based on the locations of s and p, and direction vectors $\boldsymbol{v}_s$ and $\boldsymbol{v}_p$. We illustrate the definition of control points in Figure 5.7 (a). The first control point c_1 is the mid-way point between two points H_s and H_p which have a minimum distance on the straight lines, including the points s and p along the direction vector $\boldsymbol{v}_s$ and $\boldsymbol{v}_p$, respectively. The second control point c_2 is the intermediate point between s and H_s. The third control point c_3 is the midpoint between p and H_p. When the direction vector $\boldsymbol{v}_s$ and $\boldsymbol{v}_p$ are parallel to each other, the first control point is set at the mid-way point between s and p, and the second and third points are defined in the same way as above on the straight lines including s and p. The points s and p are the starting and ending points for the interpolation, respectively. The blue points in Figure 5.7 (a) are control points for the interpolation. We interpolate the streamline with a B-spline

curve from s to p using the five points; s, p, and the three control points. The red broken curve indicates the interpolated B-spline curve.

We divide the interpolated curve in the equal interval, which is the nearest length to the stepping width h of the ordinary tracking, and establish the stepping points such that they are evenly aligned on the interpolated streamline. The stepping points on the interpolated streamline are illustrated with green dots in Figure 5.7 (b). The stepping points from the point which is four steps before the point s to the point which is four steps after the point p are named as i_1, i_2, i_3, i_4, and $i_{M-3}, i_{M-2}, i_{M-1}, i_M$, respectively.

5.3.4 Selection of interpolated trajectory

The interpolation is performed to all resumption points, which have higher FA values than $\mathrm{FA_{sch}}$ and are established the fiber tracking for ten steps after the points. We characterize all interpolated trajectories by the shape of the line, and select the best trajectory, which is assumed that it connects the most smoothly before and after the interpolation. We calculate the curvature and the torsion of the trajectory as the characterizing values.

Before the searching based on the curvature and the torsion, we perform a 'pre-search'. If the searching is started far from the crossing area, the area to search the resumption points does not cover whole crossing region. In Figure 5.8 (a) the tracking is established on the yellow line. The search is started at the red point, and all resumption points are illustrated by blue points. The area does not reach the opposite side of the crossing area since the searching is started at the point far from the crossing area. In order to deal with this problem, we examine the similarity between $\boldsymbol{v}_s$ and the first eigenvector at pre-search points. The pre-search points are dispersed in the same way as Equations (5.8) - (5.13). The definition and range of l are different from the way to determine the searching area.

$$l = 2L - 1 \quad (1 \leq L \leq 10), \tag{5.14}$$

where L is an integer. That is closer to s than the locations of the resumption points. We calculate the FA value at the pre-search points, and count the number of points N_{FA} where the FA value is larger than the threshold value for the termination $\mathrm{FA_{ter}}$. In addition, we count the number of points N_{angle} in which the angle between the directions of $\boldsymbol{v}_s$ and the first eigenvector is less than 15° at the pre-search points that have large FA value. If the percentage of N_{angle} in N_{FA} is larger than 40 %, the present stepping point is judged as the point far from the crossing area, and the ordinary tracking is continued without searching.

In addition, if the interpolated trajectory corresponding to a resumption point p has a stepping point that does not satisfy the conditions $\boldsymbol{v}_i \cdot \boldsymbol{v}_s > 0$ or $\boldsymbol{v}_i \cdot \boldsymbol{v}_p > 0$, where $\boldsymbol{v}_i$ is the tangent vector of the B-spline curve at all stepping points on the interpolated streamline, the resumption point is excluded from a probable point as the point for the

likely interpolation. The tracking before s is propagated along a red line in Figure 5.8 (b). The control points are established behind the point s due to the positional relation of two vectors $\boldsymbol{v}_s$ and $\boldsymbol{v}_p$. In order to prevent this case that the interpolation in the crossing are is performed by the unsmooth shape related to the trajectories before and after the crossing area, we apply the criteria involved in the angle between the tangent vectors on the interpolated streamline and the direction vectors at the locations of s and p.

The interpolation should be performed only in the crossing area. It should not be performed around the crossing area, where bundles are not crossing actually. If interpolation is carried out in areas where the fibers are no longer crossing at the opposite side of the tracked streamline before the crossing area, the information of the interpolated trajectory is not reliable. In that area the ordinary fiber tracking should be performed without interpolation. Therefore, a trajectory created on the basis of a certain point p that has more than 5 stepping points that satisfy the following both of the two conditions is excluded. The FA value at a point on the interpolated trajectory is more than $\mathrm{FA}_{\mathrm{sch}}$. The angle between the first eigenvector at a stepping point and $\boldsymbol{v}_i$ is less than 15°.

The curvature is calculated by using two continuous direction vectors on all stepping points from i_1 to i_M, which are 4 points before s and after p. The direction vector is defined as the vector from a certain point to the next point. We determined the number of the stepping points included in the calculation through trial and error. The degree of torsion of the trajectory is calculated with the continuous three direction vectors. We calculate the curvature and torsion on the basis of Frenet Serret formula [67] as

$$\begin{pmatrix} \boldsymbol{e}_1' \\ \boldsymbol{e}_2' \\ \boldsymbol{e}_3' \end{pmatrix} = \begin{pmatrix} 0 & \kappa & 0 \\ -\kappa & 0 & \tau \\ 0 & -\tau & 0 \end{pmatrix} \begin{pmatrix} \boldsymbol{e}_1 \\ \boldsymbol{e}_2 \\ \boldsymbol{e}_3 \end{pmatrix}, \tag{5.15}$$

where $\boldsymbol{e}_1$ represents the tangent vector of a differentiable curve, and $\boldsymbol{e}_2$ and $\boldsymbol{e}_3$ are the orthogonal vectors to $\boldsymbol{e}_1$. Two vectors $\boldsymbol{e}_2$ and $\boldsymbol{e}_3$ are orthogonal to each other. The vectors of $\boldsymbol{e}_1'$, $\boldsymbol{e}_2'$, and $\boldsymbol{e}_3'$ are derivatives by the arc length on the curve of $\boldsymbol{e}_1$, $\boldsymbol{e}_2$, and $\boldsymbol{e}_3$. The values of κ and τ indicate the degree of the curvature and torsion, respectively.

Frenet Serret formula holds for a differentiable curve. However, the stepping points and the direction vectors on the trajectory are discrete. Then, we determine the orientations of the differentiated vectors as a variation from the present direction vector to the next vector. We establish the position vectors $\boldsymbol{i}_{m-3}, \boldsymbol{i}_{m-2}, \boldsymbol{i}_{m-1}, \boldsymbol{i}_m$ of four continuous stepping points shown in Figure 5.9 (a). The point i_m represents each stepping point from i_1 to i_M. The parameter h indicates the stepping width of the tracking. The unit vectors between of direction vectors are defined as

$$\begin{aligned} \boldsymbol{e}_{11} &= (\boldsymbol{i}_{m-2} - \boldsymbol{i}_{m-3})/|\boldsymbol{i}_{m-2} - \boldsymbol{i}_{m-3}| \\ \boldsymbol{e}_{21} &= (\boldsymbol{i}_{m-1} - \boldsymbol{i}_{m-2})/|\boldsymbol{i}_{m-1} - \boldsymbol{i}_{m-2}| \\ \boldsymbol{e}_{31} &= (\boldsymbol{i}_{m} - \boldsymbol{i}_{m-1})/|\boldsymbol{i}_{m} - \boldsymbol{i}_{m-1}|. \end{aligned} \tag{5.16}$$

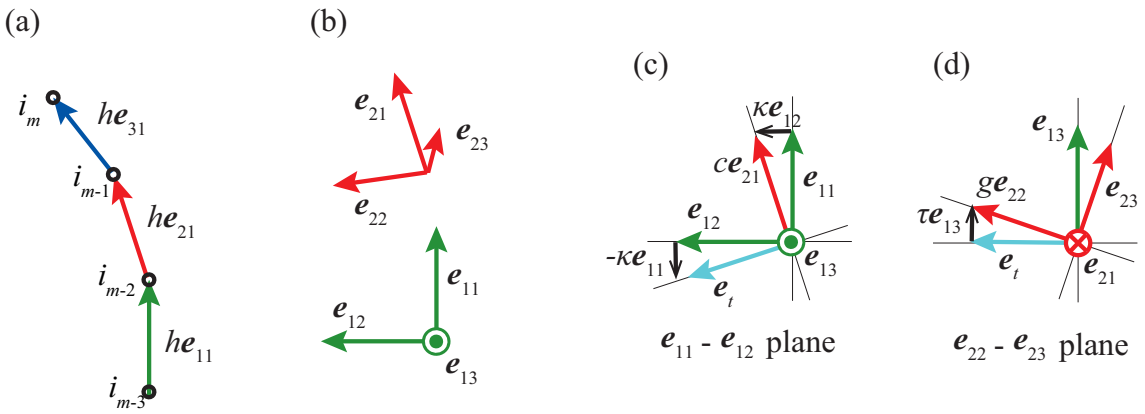

Figure 5.9: (a) The location of four continuous points and the direction vectors between each two points. (b) The orthogonal vectors of $\boldsymbol{e}_{11}$ and $\boldsymbol{e}_{21}$. (c) The definition of κ on the $\boldsymbol{e}_{11}$-$\boldsymbol{e}_{12}$ plane. (d) The definition of τ on the $\boldsymbol{e}_{22}$-$\boldsymbol{e}_{23}$ plane.

The orthogonal unit vectors of $\boldsymbol{e}_{j1}$ $(j = 1, 2)$ are $\boldsymbol{e}_{j2}$ and $\boldsymbol{e}_{j3}$ (Figure 5.9 (b)). We calculate the curvature κ and the degree of torsion τ from the unit vectors of three direction vectors as

$$
\begin{aligned}
\boldsymbol{e}_{11} \cdot \boldsymbol{e}_{12} &= 0 \\
\boldsymbol{e}_{12} &= a\boldsymbol{e}_{11} + b\boldsymbol{e}_{21} \\
\boldsymbol{e}_{13} &= \boldsymbol{e}_{11} \times \boldsymbol{e}_{12} \\
c\boldsymbol{e}_{21} &= \boldsymbol{e}_{11} + \kappa\boldsymbol{e}_{12} \\
\boldsymbol{e}_{21} \cdot \boldsymbol{e}_{22} &= 0 \\
\boldsymbol{e}_{22} &= d\boldsymbol{e}_{21} + f\boldsymbol{e}_{31} \\
\boldsymbol{e}_t &= (\boldsymbol{e}_{12} - \kappa\boldsymbol{e}_{11})/|\boldsymbol{e}_{12} - \kappa\boldsymbol{e}_{11}| \\
g\boldsymbol{e}_{22} &= \boldsymbol{e}_t + \tau\boldsymbol{e}_{13},
\end{aligned}
\tag{5.17}
$$

where a, b, c, d, f and g represent parameters during the calculation. In Figure 5.9 (c) and (d), we show the definition of vectors and parameters on the $\boldsymbol{e}_{11}$-$\boldsymbol{e}_{12}$ plane and the $\boldsymbol{e}_{22}$-$\boldsymbol{e}_{23}$ plane.

We set a threshold for τ calculated above on the stepping points from four points before s to four points after p including the trajectory during the interpolation, in order to exclude the twisting trajectory which is unlikely shape as the tracked fiber. Any resumption points which have a τ more than 4 on at least a single stepping point on the interpolated trajectory are ejected from the points to be candidates as the most likely resumption point. We determined this threshold value of τ through trial and error. The value of τ describes the rotation around the $\boldsymbol{e}_{21}$ vector on the $\boldsymbol{e}_{22}$-$\boldsymbol{e}_{23}$ plane in Figure 5.9 (d). When the τ value is 4, $\boldsymbol{e}_{22}$ rotates about 76° from the $\boldsymbol{e}_{11}$-$\boldsymbol{e}_{12}$ plane.

Then, we calculate the standard deviation of the curvature through all stepping points from i_1 to i_M in each streamline corresponding to each resumption point p. We select the resumption point p uniquely that has the minimum standard deviation of the values of the curvature as the most probable point $p_{\min}$. Finally, we assign the interpolated trajectory based on $p_{\min}$ as the tracked fiber connecting before and after the crossing area. The ordinary tracking is performed continuously until the conditions at the stepping point satisfy the terminal criteria after the interpolation in the crossing area. We restrict the interpolation to one time per a trajectory from a single seed point.

For comparison, we also carry out fiber tracking applying three previous methods with the same simulation MR-DTI data. The first method is the TEND method (Method I), the second one is a method based on a search for similarity among direction vectors (Method II). This method was developed by our team previously [37]. In this method, we set the condition in which the search begins as the case in which the FA value at the present stepping point is reduced to 20 % less than the mean FA value of 5 successive tracking points before the present point. The third one is a method based on a interpolation with Bezier curve with a single control point and a selection by only the minimum curvature (Method III) [68, 69]. The starting and ending areas and the terminal criteria for the ordinary tracking are determined in the same way as that used in the proposed method in this study.

5.4 Results

We show the tractographies obtained from the fiber tracking using the four types of the tracking methods in Figures 5.10 - 5.13. Figures 5.10 and 5.11 show the results with the straight model, and Figures 5.12 and 5.13 represent the results with the curved model. The tracking was started from the region of CC (A1, A3) in Figures 5.10 and 5.12 and from V5 (A2, A4) in Figures 5.11 and 5.13. In each figure the images of (a) - (d), (e) - (h), and (i) - (l) represent the tractographies of the simulation data sets with SNR of 300, 100, and 50, respectively. The red asterisk or circle in the images representing the results of our proposed method and Method III indicate the location of the point s to start the interpolation. The location of the point p where the fiber tracking resume the ordinary tracking is represented by the blue asterisk or circle. The background image in each figure shows the axial $b0$ image ($z = 14$) of the data set for the simulation.

We counted the number of tracked fibers from each starting area to the opposite terminal area successfully. The percentage of the successful tracking in all trajectories corresponding to all seed points is calculated in each case. The percentages are shown in Figure 5.14. With Method I, no fibers were tracked along Fiber 1 until the ending region in both models, from any starting region.

When we used Method II, the fibers in the ratio of 66.1 % (from CC) and 67.8 % (from V5) in the straight model, and 20.7 % (from CC) and 25.2 % (from V5) in the curved model were tracked until the ending region with the data sets of SNR = 300. The trajectories with the percentage of 56.4 % (from CC) and 57.0 % (from V5) in the straight model, and 7.4 % (from CC) and 18.5 % (from V5) in the curved model were tracked successfully in the data sets with SNR = 100. The percentage of the successful tracking was 28.5 % (from CC) and 46.7 % (from V5) in the straight model, and 5.2 % (from CC) and 23.0 % (from V5) in the curved model with SNR = 50.

In the case with Method III, the streamlines of 74.5 % (from CC) and 79.4 % (from V5) in the straight model, and 28.9 % (from CC) and 49.6 % (from V5) in the curved model with SNR = 300 reached to the terminal areas. In the case of the application of Method III for the data sets with SNR = 100, the trajectories of 18.1 % (from CC), 83.6 % (from V5) in the straight model, and 28.9 % (from CC), and 81.5 % (from V5) in the curved model, were tracked continuously until the terminal areas. The percentage of the successful tracking was 80.6 % (from CC) and 73.3 % (from V5) in the straight model, and 31.1 % (from CC) and 63.7 % (from V5) in the curved model with SNR = 50.

When we performed with the proposed method for the simulation data with SNR = 300, the trajectories of 18.2 % (from CC) and 27.9 % (from V5) in the straight model, and 74.1 % (from CC) and 91.1 % (from V5) in the curved model were tracked until the terminal areas. We illustrated that the trajectories of 53.9 % (from CC) and 60.0 % (from V5) in the straight model, and 67.4 % (from CC) and 74.1 % (from V5) in the curved model with SNR = 100 were connected between the areas to start the tracking and the areas to terminal the propagation. When we applied our proposed method to the data sets of simulation with SNR = 50, the trajectories of the ratio of 46.1 % (from CC) and 63.0 % (from V5) in the straight model, and 64.4 % (from CC) and 60.7 % (from V5) in the curved model reached the terminal areas by the interpolation in the crossing area of multiple fibers.

5.5 Discussion

Method I, TEND method, is known as a tracking method that can track fibers correctly even if the FA declines temporarily on the tracking streamline because the direction of tracking is not much deflected in areas where the FA value of the voxel on the streamline has a low value. The width of the crossing area along the targeted fiber of simulation images was 10 $\sim$ 12 mm in this study. Therefore, Method I could not track fibers completely in areas where the width of the crossing area was too wide.

Using Method II, some fibers could be interpolated in the fiber crossing area. However, many interpolated streamlines crossed one another and were not parallel to the actual

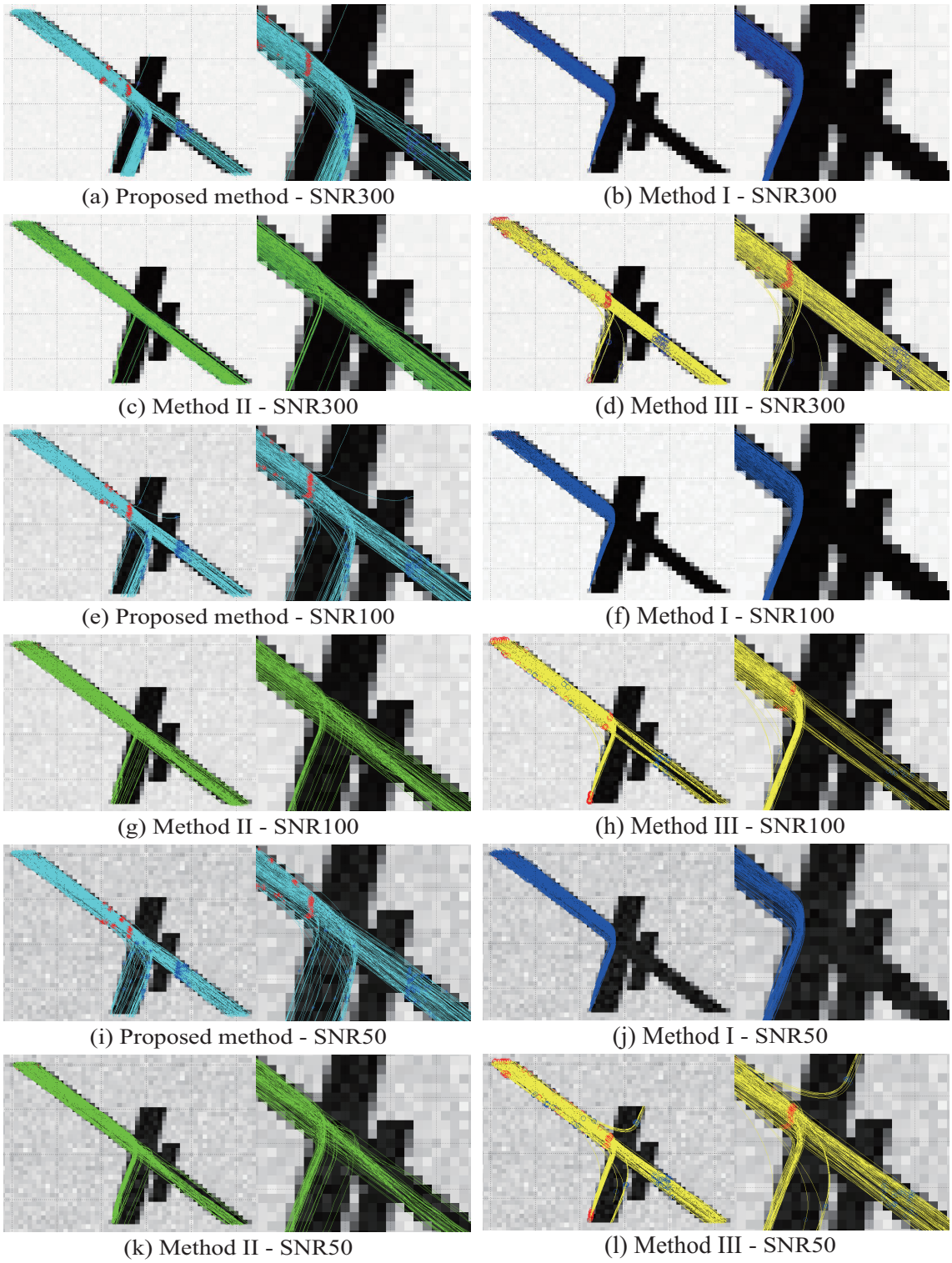

Figure 5.10: The tractographies started from CC area in the straight model for the simulation.

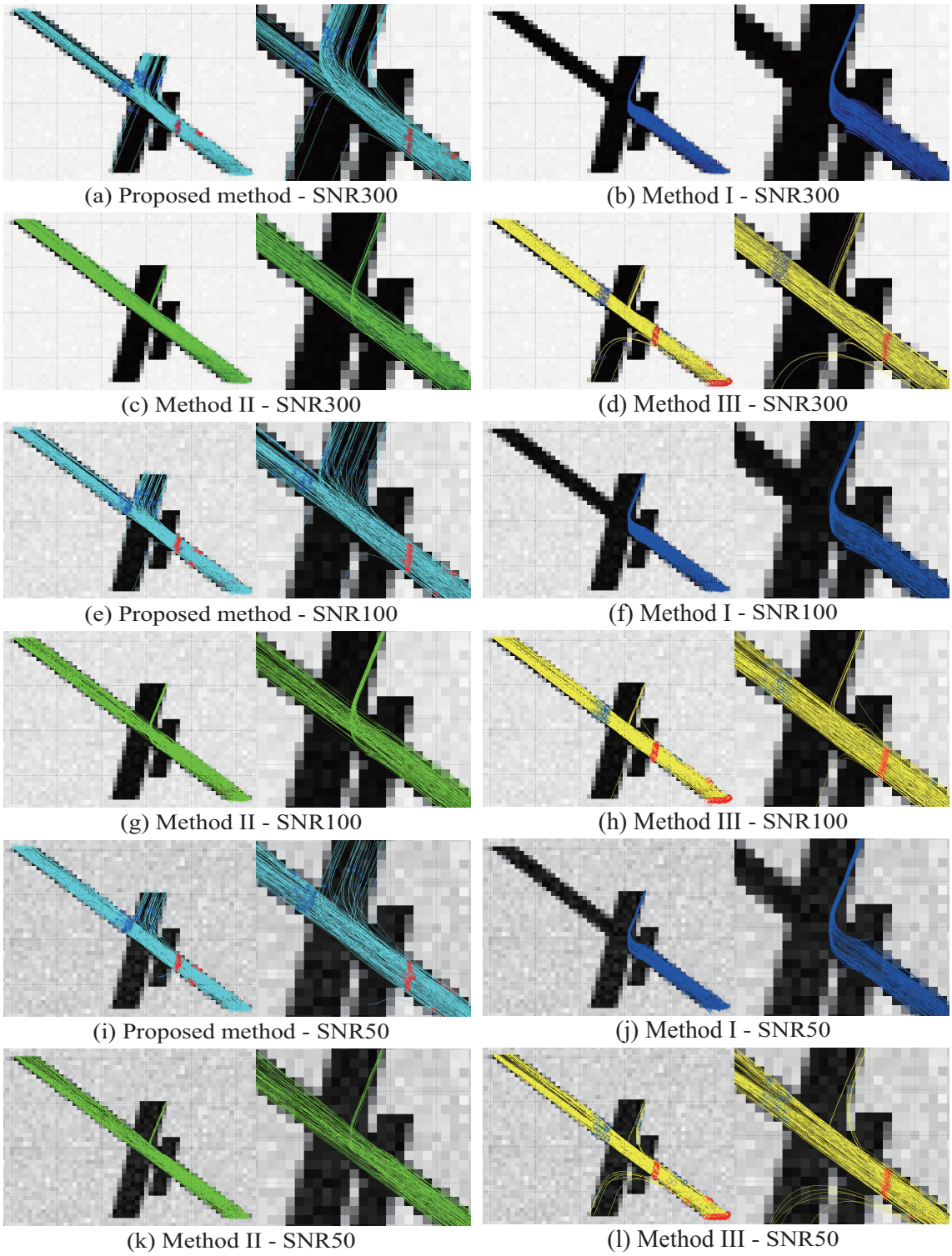

(a) Proposed method - SNR300 (b) Method I - SNR300
(c) Method II - SNR300 (d) Method III - SNR300
(e) Proposed method - SNR100 (f) Method I - SNR100
(g) Method II - SNR100 (h) Method III - SNR100
(i) Proposed method - SNR50 (j) Method I - SNR50
(k) Method II - SNR50 (l) Method III - SNR50

Figure 5.11: The tractographies started from V5 area in the straight model for the simulation.

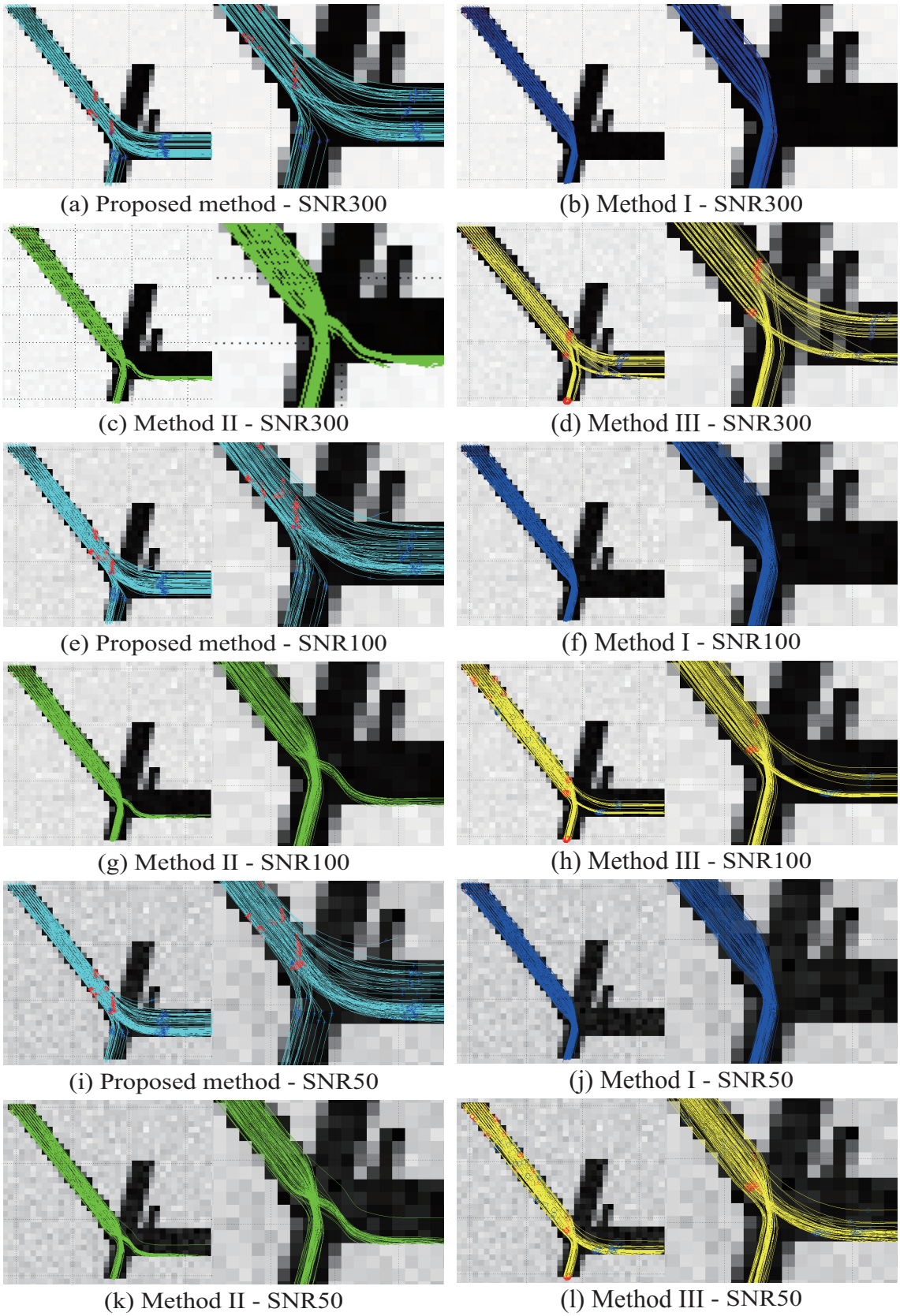

Figure 5.12: The tractographies started from CC area in the curved model for the simulation.

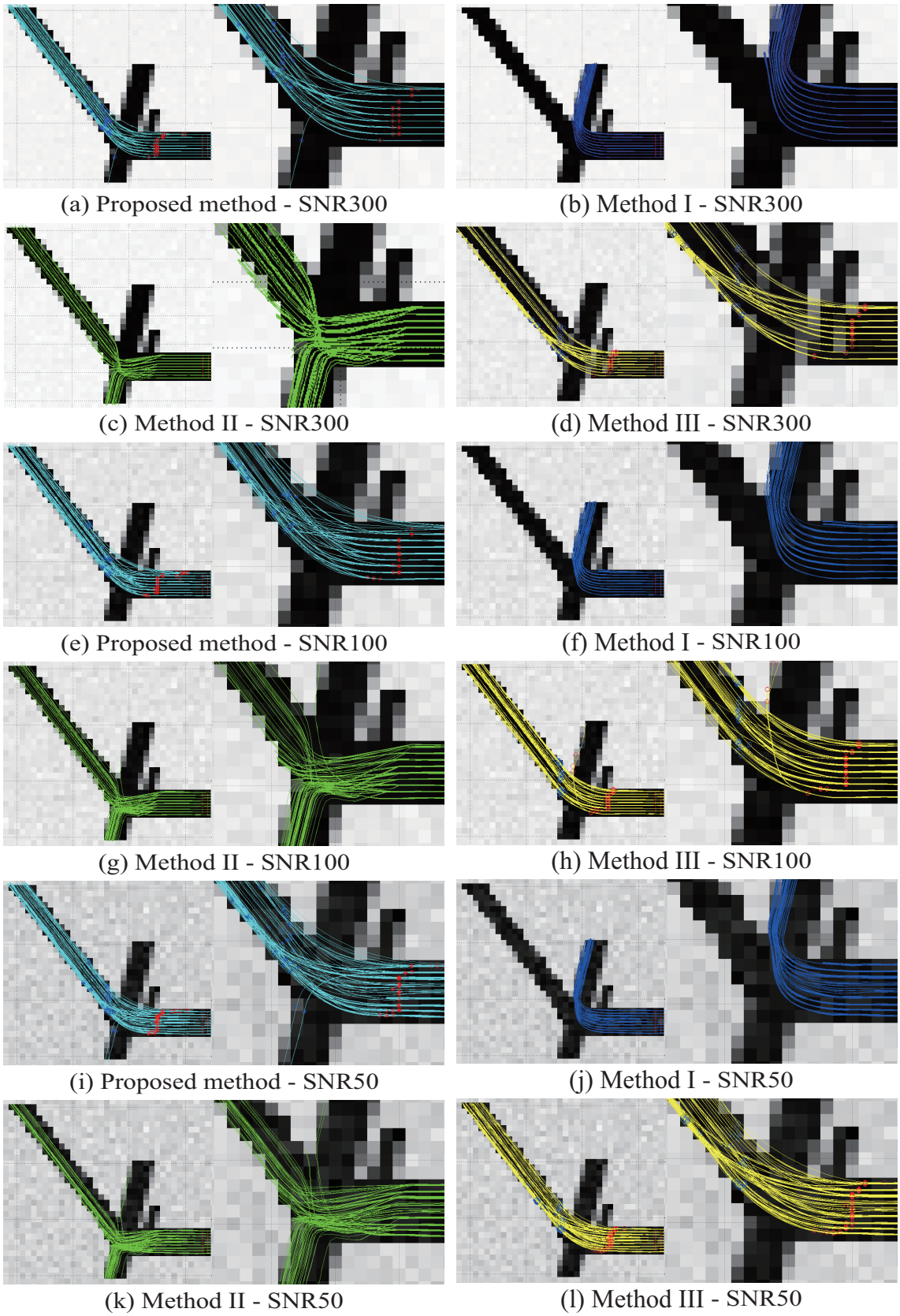

Figure 5.13: The tractographies started from V5 area in the curved model for the simulation.

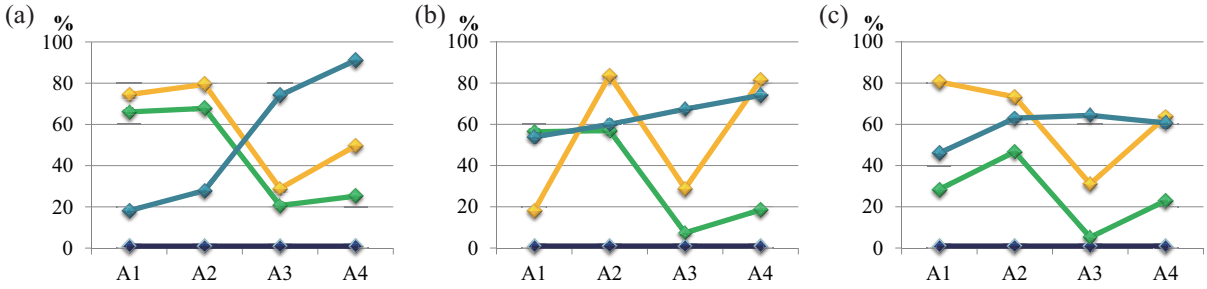

Figure 5.14: The percentage of the successful tracking. The light blue, dark blue, green, and yellow lines represent the results with the proposed method and Methods I, II, and III, respectively. The A1 - A4 indicate the starting region for the tracking shown in Figure 5.3. (a) SNR = 300. (b) SNR = 100. (c) SNR = 50.

shape of the targeted bundle in the crossing area of fiber bundles, which made it difficult to assert an accuracy of the interpolation. On the other hand, relatively few streamlines crossed in the fiber crossing area when we used Method III, which was our previous method. Some streamlines had a larger curvature than that of the actual simulation image with Method III.

When Method III was applied to the curved model, the percentage of successful tracking declined considerably, in particular the case when the tracking was started from the CC area, compared to the case of the straight model. It is considered that the interpolation by Method III is misled by the curved shape of the crossing area.

In contrast, the proposed method had few interpolation errors for the fiber tracking in the curved model. Although the proposed method did not show the robustness for the tracking in the data set of the straight model for the simulation, it exhibited several robustness for the fiber tracking with the curved model. In particular, the progress in the case of the tracking from CC area with the curved model was remarkable. In the simulation data sets with SNR = 300, which is the most similar image to the actual DTI image of the human brain, the rate of successful tracking by our proposed method was lower than that of the tracking by Methods II and III with the straight model, whereas the rate by our proposed method was higher than those by the other methods with the curved model in both cases with two starting areas. Our proposed method applied not only the curvature of the interpolated trajectory but also the degree of the torsion of the streamline to the searching criteria and interpolated the trajectory by B-spline curve. Therefore, the proposed method is considered to suit the interpolation for the nerve bundle with the curved or twisted shape, since the trajectory with the small degree of change in curvatures and the small magnitude of torsion is selected as the most probable trajectory to connect before and after the crossing area. On the other hand, Methods II and III are considered to be preferable to the interpolation of the crossing area with the multiple

bundles of the straight shapes. Since the actual nerve bundles are usually curved and twisted, the proposed method may be appropriate to the interpolation of the crossing areas during the fiber tracking in the actual image of the human brain.

In a previous method reported in [35], the ending region for the fiber tracking as well as the starting region is need to be defined before the tracking starts, and some manual operations are required during the tracking. The results of the tracking depend on the ending region configured manually. It suffers from the arbitrariness. Our present method performs the tracking after we set just the starting region for the fiber tracking. The tracking method does not have any information at where the propagation should arrive before the propagation starts. The stepping point propagates automatically after we determine the starting region without any manual operation. It was suggested that our method eliminated the arbitrariness as well as possible.

The estimation of the direction of the targeted fiber is performed in the area where the only two fibers cross each other in a method reported in [36]. It is not performed when more than three fibers cross. The detailed anatomical information is required for the setting of the region of interest since the number of fibers should be informed before the tracking. When the abnormality exists in the nerve fibers, the anatomical information may not have reliability. Our method does not depend on the number of fibers crossing each other. Although our method depends on the width of the crossing area, the length of the searching area along the direction of the tracking is considered to be long enough for the actual human brain.

A lot of directions of MPG are required in the acquisition of the diffusion tensor images for a method in [38]. We can obtain manifold diffusional information when a lot of directions of MPG are applied. However, it takes a long time for the acquisition. Since we aim our method at the usage for the clinical diagnosis saving time, the acquisition and calculation time should be short. Our method requires just six directions of MPG, which is the minimum number for the diffusion tensor imaging.

A previous method in [39] attempts to find the configuration of fibers that explains the obtained data. Although it well estimates the location of a fiber, it is extremely computer-intensive limiting the use in clinical situation. The amount of calculations in our method is remarkably small and the tracking takes only short time. Hence, it is reasonable to conclude that our method suits to the clinical usage.

Chapter 6

Conclusion

In this dissertation, we have proposed several novel methods to characterize the features of nerve tracts in the human brain by use of the fiber tracking and tractographic techniques with the magnetic resonance diffusion tensor imaging, in order to evaluate quantitatively the disruption of integrity for the nerve tracts of schizophrenic patients. It is desired to measure and evaluate the abnormalities in nerve fibers of the psychiatric disorder noninvasively for diagnosis. The numerical evaluation of the features along the fiber tracts have not been established in clinical occasions. Hence, it is considered that the efficient methods proposed in this dissertation are helpful for the future diagnosis.

In Chapter 1, we have introduced the basic structures of the human brain, fundamental facts about human higher brain functions, and circumstances to plan the works in this dissertation. In addition, we have summarized the previous works, clarified remaining problems, and described objectives in this study.

Chapter 2 has provided the background knowledge related to the principles of techniques, which we have employed to establish our works, the technical previous works, and the characteristics of the schizophrenia. From the principles, we have clarified the important features of the noninvasive imaging techniques, in particular the techniques involved in the magnetic resonance imaging. The magnetic resonance imaging obtains the contrast depending on the constituents of the brain tissues on the basis of the magnetic resonance phenomena of protons in vivo. The diffusion weighted imaging measures the diffusional phenomena of water molecules by using the technique of the magnetic resonance imaging. Three-dimensional movement of water molecules is defined with multiple diffusion-weighted images in the diffusion tensor imaging, which we used in this study. The fiber tracking based on the diffusion tensor imaging establishes the three-dimensional reconstruction of the nerve tracts and extract the features of the nerve fibers along the tracts. At the end of Chapter 2, we have described that the schizophrenia is the most debilitating disease of all adult psychiatric disorder in order to explain the reason why we have carried out this study.

Chapter 3 is devoted to the demonstration of the quantitative analyses along the nerve fibers to evaluate the abnormalities of the schizophrenia in comparison to the healthy subjects. We have performed fiber tracking in the superior longitudinal, inferior longitudinal, and fronto-occipital fasciculi with the regions of interest constructed through manual settings to suit the characterization of the tracts. Results obtained in this chapter have demonstrated the feasibility that several indices obtained from the fiber tracking in the proposed region of interest have been useful for the quantitative evaluation of the abnormality of the tracts in the patient brain.

Next, we have described a novel method to construct the region of interest automatically with the fiber tracking technique in Chapter 4. The construction method of the region of interest could reduce the quantity of works significantly and eliminated the arbitrariness during the performance of the fiber tracking. We have analyzed the structural abnormalities in the nerve tracts of the sagittal stratum, including the inferior longitudinal and inferior fronto-occipital fasciculi, and the superior longitudinal fasciculus in schizophrenic patients. From the analyses, we have found significant differences in several indices obtained from the fiber tracking with the automatic method for the region construction. The results for several indices obtained in the present analyses have been consistent with those in previous studies. The indices introduced in our present study could characterize the structures of the nerve tracts in detail. These results have demonstrated the feasibility that the proposed automatic construction method of the region of interest has suited to the evaluation of the abnormality in the targeted nerve tracts of schizophrenic patients.

In Chapter 5, we have proposed a method for interpolation in the fibers crossing area during fiber tracking. It is desirable to be enabled to evaluate the characteristics of the nerve fibers in the crossing area for detecting the abnormalities in the nerve fibers. In order to address the problem on the error during fiber tracking in areas where multiple tracts cross each other, we have proposed a tracking method for the interpolation based on the evaluation of accuracy that has employed the standard deviation of the curvature and the torsion as the threshold along the interpolated streamlines. The proposed method has been validated in two types of simulation data sets, which have been the straight and curved model, and the performance has compared to the three kinds of previous methods. By the experiments with simulations, we have shown the improved degree of robustness for the tracking obtained by the application of the proposed method. In particular, the development of the performance for the curved model was remarkable. The results of this chapter have demonstrated the efficiency of the proposed method in the crossing areas where the diffusional anisotropy of the water molecules has reduced.

In conclusion, we have proposed three methods related to the performance of the fiber tracking technique in this dissertation. We have demonstrated the feasibility that

we evaluate the abnormalities in nerve bundles of schizophrenic patients by use of several indices, which we have shown their significant effects on the disease with the fiber tracking described in Chapter 3. We may evaluate the schizophrenia quantitatively in an individual by an estimation based on criteria with combination of the indices.

The construction method of the region of interest has been developed in order to extract the characteristics of nerve fibers in the schizophrenic patients with efficiency provided in Chapter 4. The method for the construction of the region of interest may be effective to evaluate the abnormalities in nerve bundles of the other disorder involved in the higher brain function. Taken together, it is expected that the method reduces the time to process the subject's images and is useful for the numerical evaluation of the higher brain dysfunctions.

Although we targeted several parts of nerve bundles with relatively straight shape without crossing fibers in this study, more curved fibers with crossing areas might be targeted for the fiber tracking by use of our present method for the interpolation of the fibers crossing areas proposed in Chapter 5. The nerve fibers, which have been excluded from the fibers to be evaluate quantitatively with the conventional fiber tracking, might be employed as the considerable fibers to measure the abnormalities caused by disorders with our proposed tracking method. We expect that the early diagnosis and treatment of schizophrenia are supported by the applications of the proposed methods in the future.

Appendix A

Normalization of MR-DTI images by MRI Studio

In order to construct the ROI automatically, we normalize the subjects' images corresponding to the standard brain by MRI Studio including DTI Studio, ROI Editor, and Diffeo Map.

We can use these software for free without installation in Registry of a personal computer. The softwares contained in MRI Studio are initiated by opening '.exe' files. Since MRI Studio is a collection of the Microsoft Visual Studio applications, the Microsoft Visual Studio Redistribution package needs to be installed on the machine before the MRI Studio applications. After a registration of personal account on the homepage of MRI Studio, we download the software following the tutorial part in 'Workshop' page.

A.1 DTI Studio

First, we calculate the diffusion tensor, the first eigenvector and eigenvalue of the diffusion tensor, the FA value, and the trace using MR-DTI data in DICOM (digital imaging and communication in medicine) format by DTI Studio. In order to create the calculated images, we load the original DICOM images through 'DTI Mapping' for 'Siemens, GE or Philips DICOM'. We set the parameters for loading of images in the next screen (Figure A.1). Since the axial DICOM images collected slice by slice from the inferior side to the superior side of the brain, we select the slice orientation and the slice sequencing properly. We process all slices, which include 200 or 240 images by each subject with eight images in a single slice for 25 or 30 axial slices. We employ the b value of 1000 in the image acquisition. In the gradient table, the components of directions used for MPG are designated in the same order as that of the image acquisition. Note that the eighth image for each slice is not included for the processing. The gradient table in the lowest row is set as 100, in order to avoid including the eighth image. This way to setting of 100 is specific to this software. Then we select one of the DICOM images in a folder, which

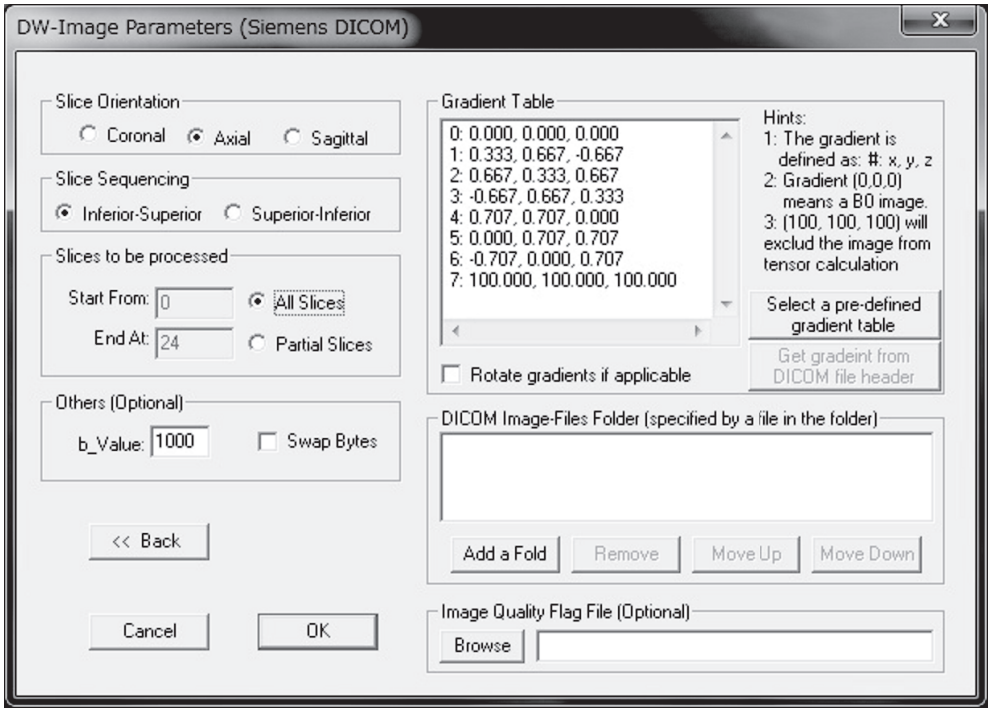

Figure A.1: The screen for the setting of parameters for loading of images. The parameters set in this screen shot are values employed in this study.

has all images to be processed, clicking over 'Add a Fold' icon. After we click 'OK', the DICOM images are loaded into DTI Studio, constructing the three dimensional images for each direction of MPG.

In the primary view of DTI Studio, the axial, sagittal, and coronal images are seen in separate windows (Figure A.2). We can rotate the three dimensional image at the upper left window by clicking and dragging operations. The slice numbers and the MPG number of the displayed image are checked in the right operation window. Note that the numbers start from 0 for the first slice although the number starts from 1 in MATLAB. We count the slice number from 1 corresponding to MATLAB when we show the number in this study. At the bottommost row in the primary view, a value of a intensity in a pointing voxel of the stored image is described.

Original diffusion weighted images are first processed in 'Automatic Image Registration' to remove the artifacts by brain motion corresponding to the $b0$ image. All images are added in the list for images to be registered. We employ 'Affine' for the linear transformation approach to deal with the rotation, translation, scaling and shear of images by 12 parameters. The method of 'Tri-Linear interpolation' is employed to interpolate values after the registration. Several examples of the images before and after the automatic image registration are shown in Figure A.3. The images in the upper row represent the

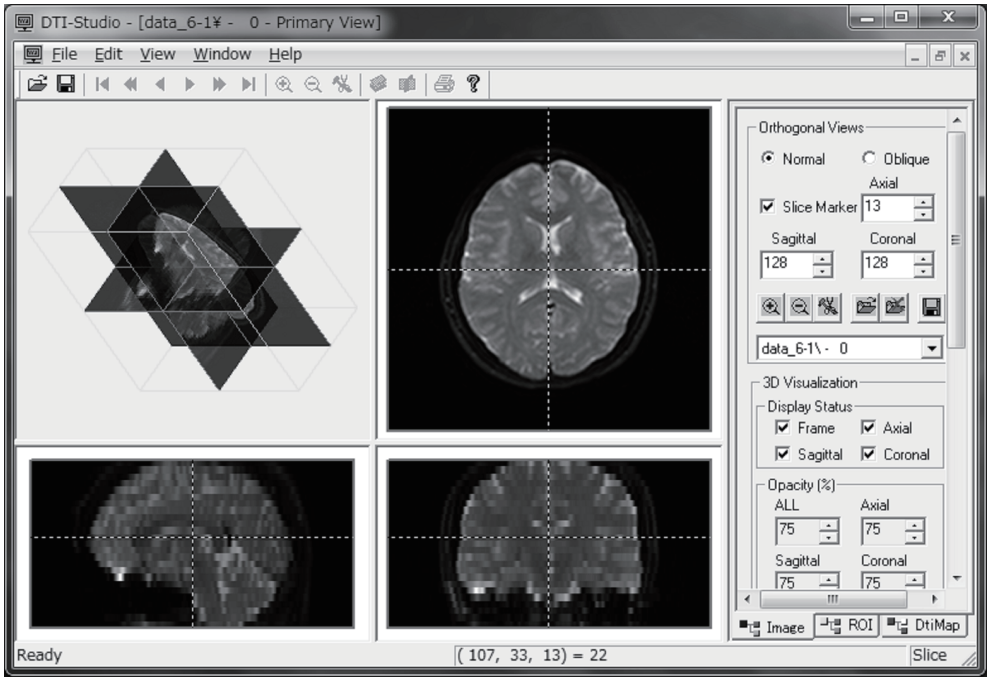

Figure A.2: The primary view of DTI Studio.

original images; (a) is a $b0$ image and (b)-(d) are diffusion weighted images for the three of all directions of MPG. The lower images indicate the registered images of the upper images.

The diffusion tensor, FA value, trace value, first eigenvector, and data for the color map are calculated in 'Tensor, Color Map etc.' included in the caption page named 'DtiMap'. We employ the method of 'Automatic outlier PIXEL rejection' to eliminate the bad pixel including a noise signal with optional parameters (Figure A.4); the threshold value for the 'minimum bad area' of 50 and the default values for the other parameters. In order to check the coordinates of bad pixels after the calculation, we save them by 'Binary Mask' in a text file. We select the trace image in 'Get More Results'. The calculation takes a few minutes.

In Figure A.5, we show the images representing the components of the diffusion tensor. The images indicate D_{xx} (a), D_{yy} (b), D_{zz} (c), D_{xy} (d), D_{xz} (e), and D_{yz} (f) in the same axial slice as those in Figure A.3. The values of D_{xx}, D_{yy}, and D_{zz} take numerical values in $10^{-4} \sim 10^{-3}$ order, and those of D_{xy}, D_{xz}, and D_{yz} have levels in $10^{-5} \sim 10^{-4}$ order. The images of D_{xy}, D_{xz}, and D_{yz} are more bright in comparison to the images of diagonal components; D_{xx}, D_{yy}, and D_{zz} since the images are displayed with scaling according to the range of each image. We save the data set of all components of the diffusion tensor together in a raw data format.

The calculated images in a single slice are described in Figure A.6. The first eigenvector

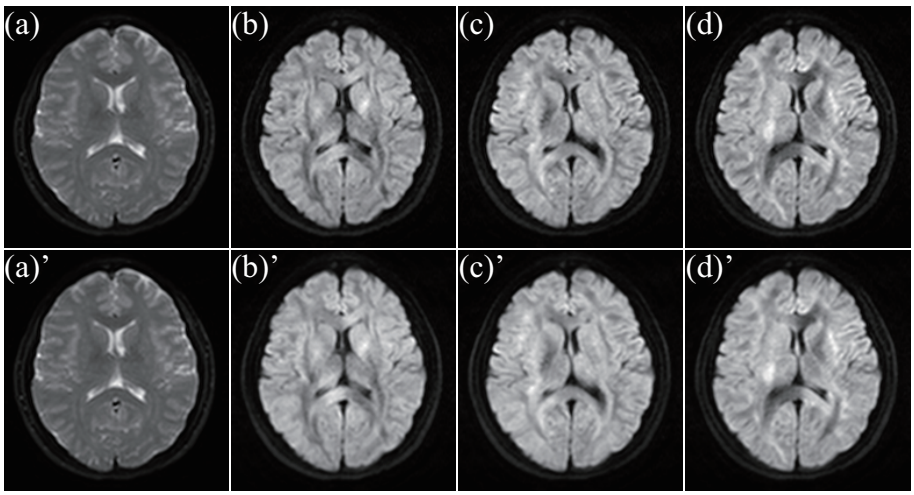

Figure A.3: The original $b0$ and diffusion weighted images are shown in the upper row (z = 14). The images in the lower column represent the registered images.

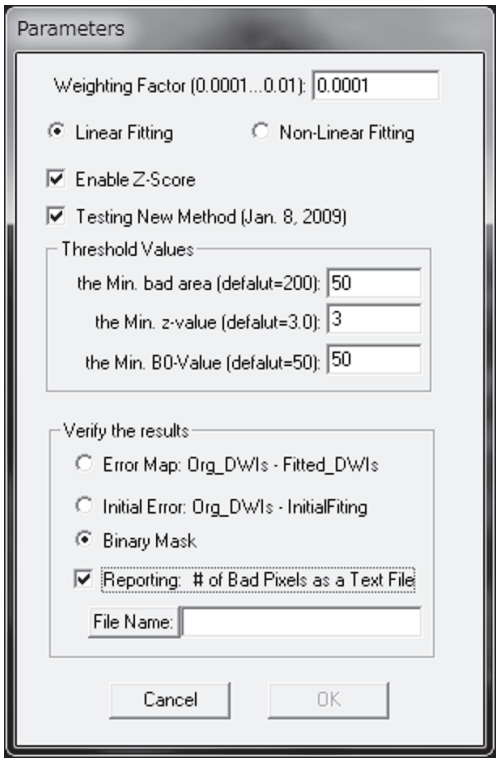

Figure A.4: The setting of parameters for the calculation of the diffusion tensor, FA value, trace value, first eigenvector and data for the color map.

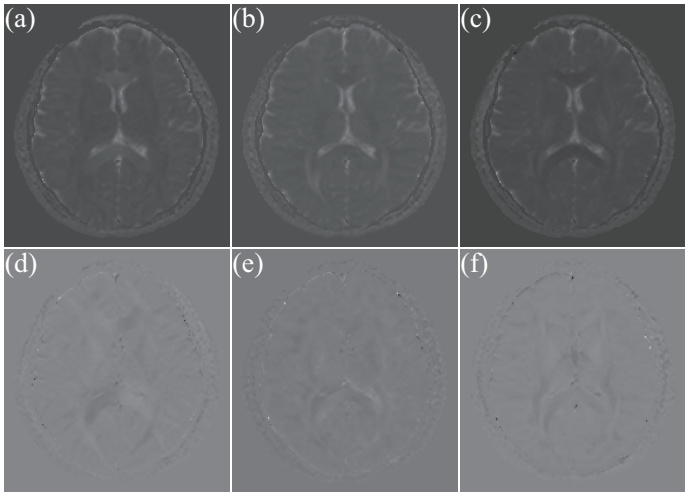

Figure A.5: The images representing components of the diffusion tensor ($z = 14$). (a) D_{xx}, (b) D_{yy}, (c) D_{zz}, (d) D_{xy}, (e) D_{xz}, and (f) D_{yz}.

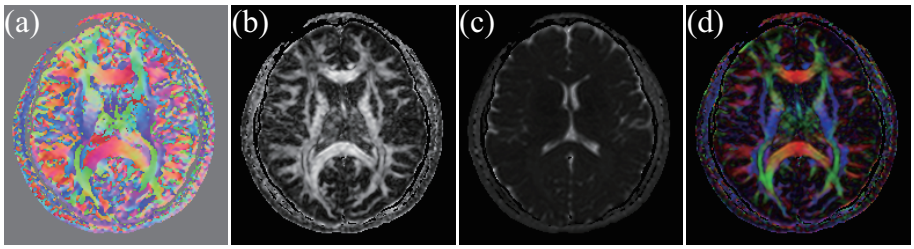

Figure A.6: (a) The image representing the first eigenvector. (b) The FA image. (c) The trace image. (d) The color map image ($z = 14$).

is shown in (a) as 'Vector' format. The x, y, and z components of the vector correspond to the red, green, and blue colors, respectively. It has four dimension data set including the three dimensional volumetric image for three axes. The images of (b) and (c) represent the FA and trace images. Although the trace image has three times of MD value in each voxel, the contrast is the same as the MD image since the image is scaled for a range of the image. The color map (d) represent the first eigenvector multiplied by the FA value for each component. In this image the value in each voxel is rescaled to the integer in the 256 grade system for each components of the red, green, and blue colors. We save all images separately as the data sets in the analyze format. The analyze format is commonly used in the medical imaging analysis, which holds information in a '.hdr' file about the image such as the matrix size, the size of field of view and the data format of values included in the image, as well as image data in a '.img' file. In addition, we save the $b0$ image in the analyze format to apply the skull stripping described in the following paragraph.

A.2 ROI Editor

ROI Editor is used to apply the skull stripping to the calculated data sets using the 3D constructed $b0$ images. The $b0$ image corresponding to T_2-weighted image indicates the diffusion weighted image without the motion proving gradient. In other words, the diffusion is not emphasized in the $b0$ image with the imaging sequence for the diffusion weighted image. We are easy to identify a border between the cerebral parenchyma and the cranial bone in the $b0$ image. The skull stripping converts the signal intensity to zero in voxels of the non-cerebral parenchyma such as the cranial bone and some noise signals outside the brain. We apply the skull stripping to normalize the subject's brain according to the standard brain accurately.

After loading the $b0$ image in ROI Editor, we process the image using some tools as shown in Figure A.7. The automatic skull stripping is performed by clicking on the skull stripping icon at the right end in 'TOOL' box. We employ different parameters from the default setting; 'W3' of 0.013 and 'W5' of 1.5 in 'Weight' part for 'Skull Stripping Target'. A value of 'W3' defines a degree of the roundness of the border. The value of 'W5' changes the depth for cutting down the non-cerebral parenchyma. The other parameters are kept in the default values.

We check the area for the skull stripping by applying the range of the threshold from 1 to 1 with 3D in 'Threshold' icon looked like up/down arrow placed in 'TOOL' box, after selecting the image named 'SkullStrippedMaskByte' (Figure A.8 (b)). A name of each icon can be checked by hovering a cursor over an icon. The $b0$ image with selection of the area for the skull stripping is shown in Figure A.8 (a), and the image cut off the outside of the area is as described in Figure A.8 (c). The red areas in Figure A.8 (a)-(c) represent the range selected to be included in the cerebral parenchyma. The mask is constructed by clicking over 'Add' icon looked like a cross mark in 'SELECTION' box. Then the selected area is added in the inside of the border. The lower images in Figure A.8 indicate the divided images with the border corresponding to each upper image. The border is constructed between voxels, and the voxels on the visible border line are contained in the mask.

Following the performance of automatic skull stripping, we adjusted the border visually on the image of Figure A.8 (a)', since the normalization is not performed adequately, if the mask for the skull stripping has irrelevant parts obviously. Using 'Draw ROI' icon looked like a pencil mark in 'TOOL' box, we coordinate the mask on all axial slices. The area painted by the red line with that tool is selected for the containing area. We add the painted area by clicking on 'Add' icon, after selecting some areas by a mouse pointer where would be included in the skull stripping mask. Particular caution is required in adding the part of thick blood vessels and the anterior parts of brain, and eliminating the

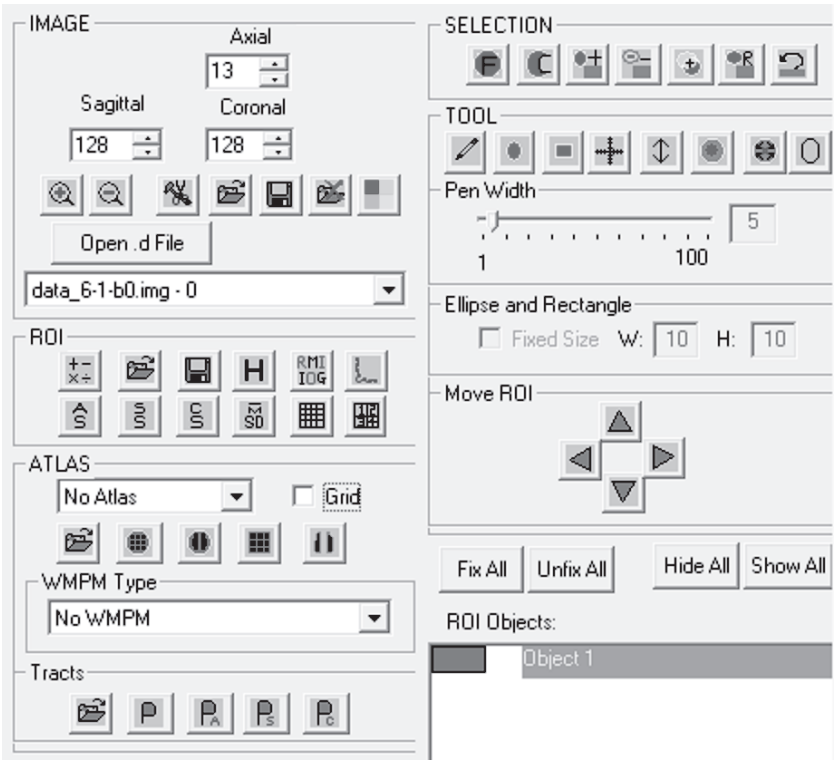

Figure A.7: The tool window of the primary view in ROI Editor.

noise part having significantly high luminance. We show the masked $b0$ image for eight slices in a single subject in Figure A.9. The images represent slices from the inferior side to the superior side in order. The image of (e) indicates the same slice as the images in Figure A.8.

In order to remove the signals of the image in the outside of the cerebral parenchyma, we apply the constructed mask to the $b0$ image, by clicking on 'Operation' icon in 'ROI' box. The name of an object constructed in the above performance is selected in the left window, and we assign a file name of the $b0$ image in the right window. The operation of 'Mask' is chosen in the pull-down menu. Then, the signal intensities in the outside area of the mask vanish. We also apply the mask to the FA image, the trace image, and the first eigenvector image, after loading the images from 'Load Image File' icon in 'IMAGE' box.

A.3 Diffeo Map

Subsequently, all images are resampled at a voxel size of $1 \times 1 \times 1$ mm^3 according to the standard brain in 'Atlas Sample Image' built in Diffeo Map, which has a $181 \times 217 \times 181$ matrix and a voxel size of $1 \times 1 \times 1$ mm^3. We use the single subject image on the

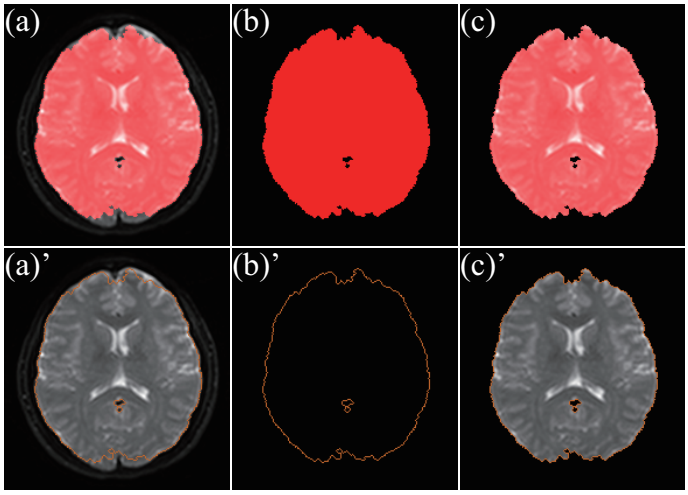

Figure A.8: The application of the automatic skull stripping tool. (a) The $b0$ image covered the selected area for the skull stripping, (b) The selecting area, and (c) The cut off image of the B0 image ($z = 14$). The lower images represent the images after the selected area is applied as the mask for the skull stripping.

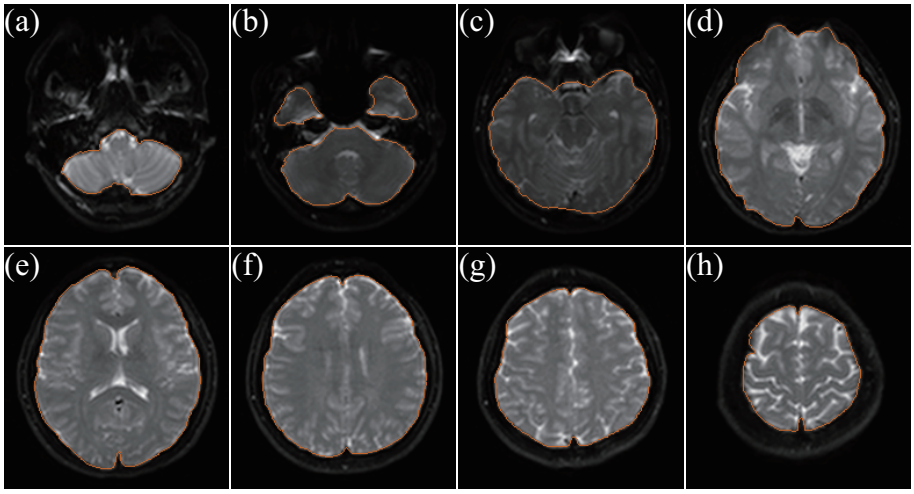

Figure A.9: The $b0$ images with the mask for the skull stripping in eight slices of a single subject. (a) $z = 2$, (b) $z = 5$, (c) $z = 8$, (d) $z = 11$, (e) $z = 14$, (f) $z = 17$, (g) $z = 20$, and (h) $z = 23$.

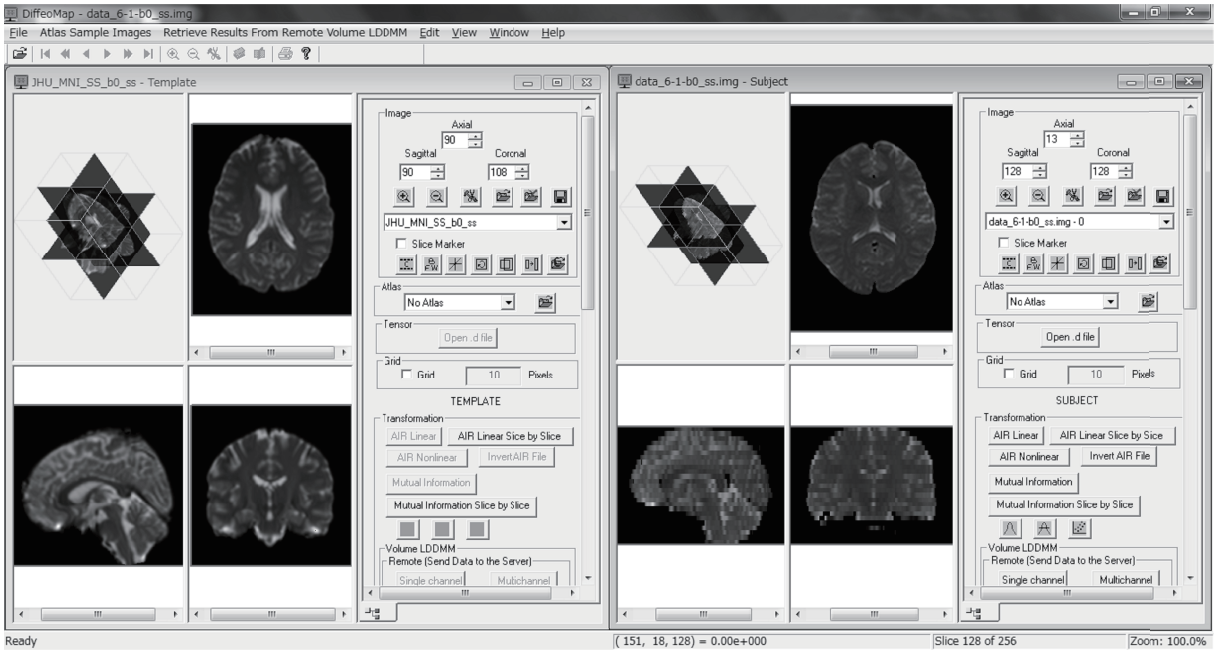

Figure A.10: The primary view of Diffeo Map. The image displayed in the left window represents the standard brain as the template for the transformation, and the right image indicates the subject's image.

MNI (Montréal Neurological Institute) coordinate for the standard brain. It is prepared in MRI Studio named 'JHU MNI SS' for 'Atlas Sample Image'. Figure A.10 describes the primary view of Diffeo Map. In Diffeo Map the first loaded image is designated as a template for transformations (the left window in Figure A.10), and the second loaded image in a different window in Diffeo Map is regarded as a subject, which is transformed to the normalized image in accordance with the template (the right window in Figure A.10). All of the subject's images skull stripped above are loaded from 'Load Image' icon in 'Image' box in the subject's window before we perform the resampling of images.

The resampling is applied from 'Resample Image' icon at the second from the right end in 'Image' box in the subject's window. The matrix size of the original image and that of the template image are represented in the left and right columns, respectively. We can resample all images simultaneously by ticking off 'Update all the loaded images'. We employed 'Trilinear' method for the interpolation. Figure A.11 shows the resampled images, for axial (a), sagittal (b), and coronal (c) slices, which represent comparable slices as those of the subject in the right window in Figure A.10).

The field of view does not match between the subject's original image and the image of the standard brain. The subject's original image has the field of view of 240 $\times$ 240 mm $\times$ 125. The standard brain has the field of view of 181 $\times$ 217 mm $\times$ 181. The directions perpendicular to the sagittal, coronal, and axial planes correspond to the x-axis, y-axis,

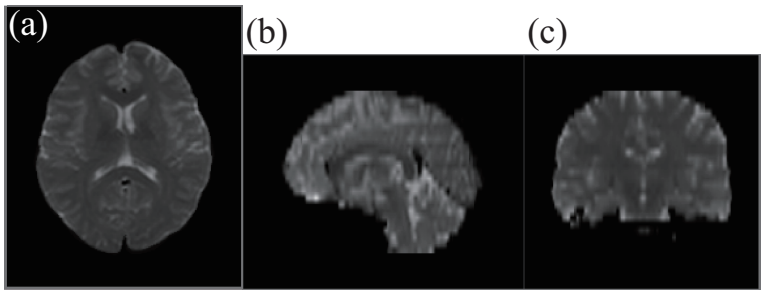

Figure A.11: The resampled subject's images corresponding to the matrix size and the field of view of the standard brain. (a) The axial image of $z = 95$. (b) The sagittal image of $x = 91$. (c) The coronal image of $y = 109$.

and z-axis, respectively. Any additional background is cut in the area, where the original size of the field of view is greater than the image of the standard brain at both ends of the x-axis and y-axis directions of the image (Figure A.11 (a)). On the other hand, extra background where the size of the original image is smaller than the standard brain at both ends of the z-axis direction of the image is added automatically (Figure A.11 (b) and (c)). We save the resampled images in the analyze format separately.

The normalization of the subject's brain corresponding to the standard brain is performed through both of the linear and the nonlinear transformations. The linear transformation matrix is made with Diffeo Map matching the $b0$ image of each subject to the standard brain. After we load the $b0$ image of the standard brain named 'JHU MNI SS b0' from 'Atlas Sample Images' for the template window, and the resampled $b0$ image of the subject brain for the subject window, the linear transformation is established with 'Traditional 9 parameter model' from 'AIR Linear' icon in 'Transformation' box in the subject window. 'Traditional 9 parameter model' represents the transformation including parallel shifts, scaling, and rotations along three rectangular axes. The transformation matrix is saved as '.air' file, which is the specified format for Diffeo Map.

We apply the matrix to all the resampled images, from 'Load Transformation Matrix' icon in 'Transformation' box in subject's window after loading the FA and trace images and the first eigenvector image in subject's window. The application is established by choosing 'AIR Linear Matrix (.air)' with 'Trilinear' and loading the '.air' file constructed above. Then all calculated images of the subject are transformed linearly according to the standard brain. We show the linearly transformed images in Figure A.12. The axial image (a) is selected for the comparable slice described in Figure A.11 (a) visually. The sagittal image (b) is the slice on the midline as well as the image in Figure A.11 (b).

We normalize the subject's images nonlinearly, using both of the FA and trace images. In order to distinguish contrast among tissues more accurately when the transform matrix

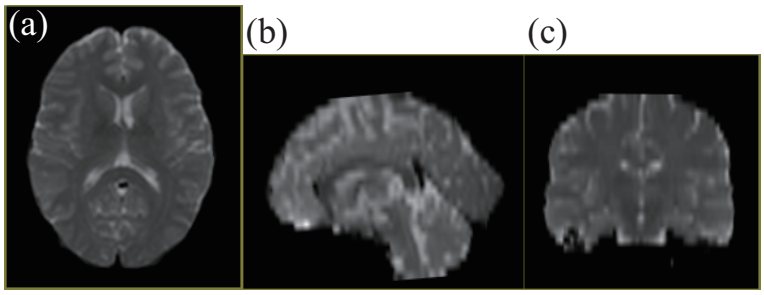

Figure A.12: The linearly transformed images of a single subject corresponding to the standard brain. (a) The axial image of $z = 83$. (b) The sagittal image of $x = 91$. (c) The coronal image of $y = 109$.

is constructed, the histograms of the intensity of subject's images are matched to those of images of the standard brain automatically for each of the FA and trace image. We perform the matching by clicking on 'Automatic Histogram Matching' icon, after loading each image for the standard brain and the subject brain in the template window and the subject's window. Since the matching of histograms is performed only for the 'byte' format in Diffeo Map, the data format of both images is changed from 'float' to 'byte' with 'Automatic Scaling' by 'Change Image Data Format' icon in 'Image' box for both of the template and the subject's images, before the matching of histograms.

In Figures A.13 and A.14, we show the FA and trace images of a single subject before and after the matching of histogram corresponding to those of the standard brain. Each image indicates the same slice as that in Figure A.12. The slices in the upper row represent the axial, sagittal, and coronal slices before the histogram matching in both of figures. They are already skull stripped, resampled, and transformed linearly for the normalization. In the lower row, the matched images in the same slices are described. We recognize that the contrast of images are emphasized after the histogram matching.

The nonlinear transformation matrix is constructed with Diffeo Map based on the large deformation diffeomorphic metric mapping (LDDMM) fitting to the standard brain. It is performed on the server of the developers for Diffeo Map from 'Multichannel' icon in 'Volume LDDMM' box in the subject's window. On the pop-up window (Figure A.15) to send data to the remote server, we assign some parameters and select the images of to be sent to the server for template images and subject images. We employ 'Number of Channels' of 2, which indicate two images of the FA image and the trace image, and 'Alpha' of 0.01 and 0.005, which controls a degree of the softness and aggressiveness for the deformation. The other parameters are kept as default setting. When the transmission of the data finishes successfully, some messages to inform the successful transmission arise in a pop-up window, and we receive two kinds of e-mails entitled 'ICM Multichannel

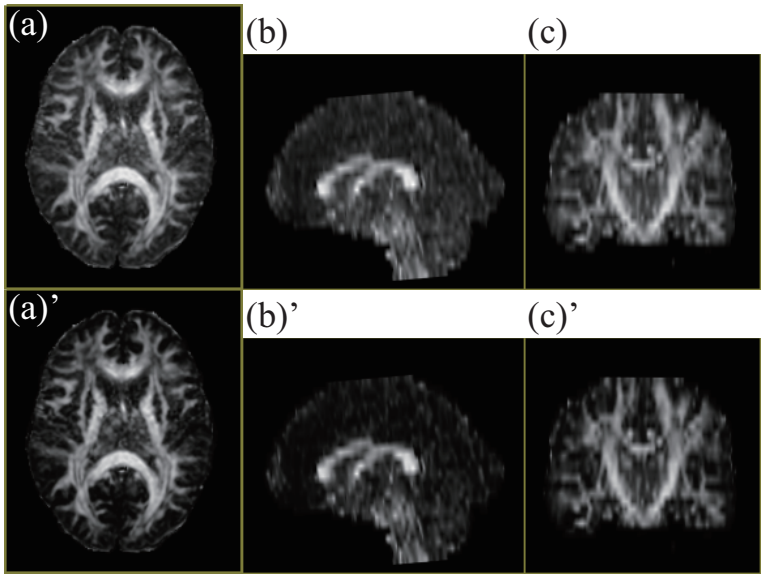

Figure A.13: The FA image of a single subject before (the upper row) and after (the lower row) the matching of histogram corresponding to the FA image of the standard brain.

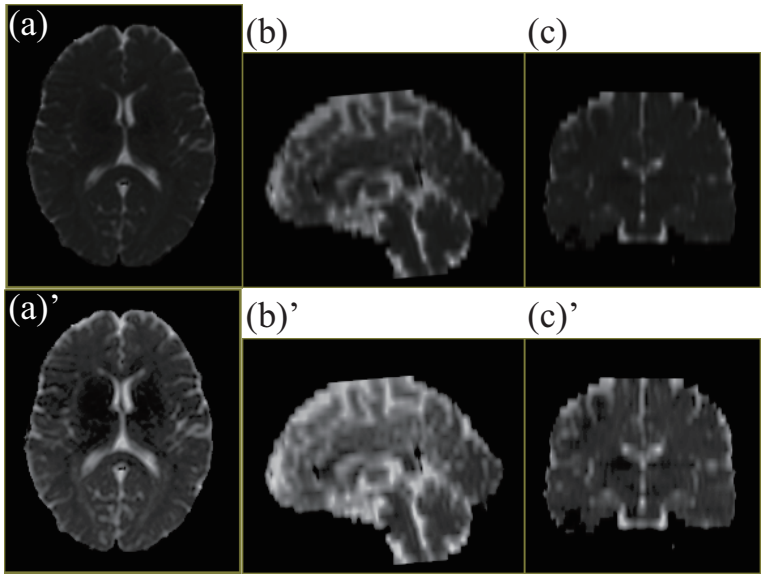

Figure A.14: The trace image of a single subject before (the upper row) and after (the lower row) the matching of histogram corresponding to the trace image of the standard brain.

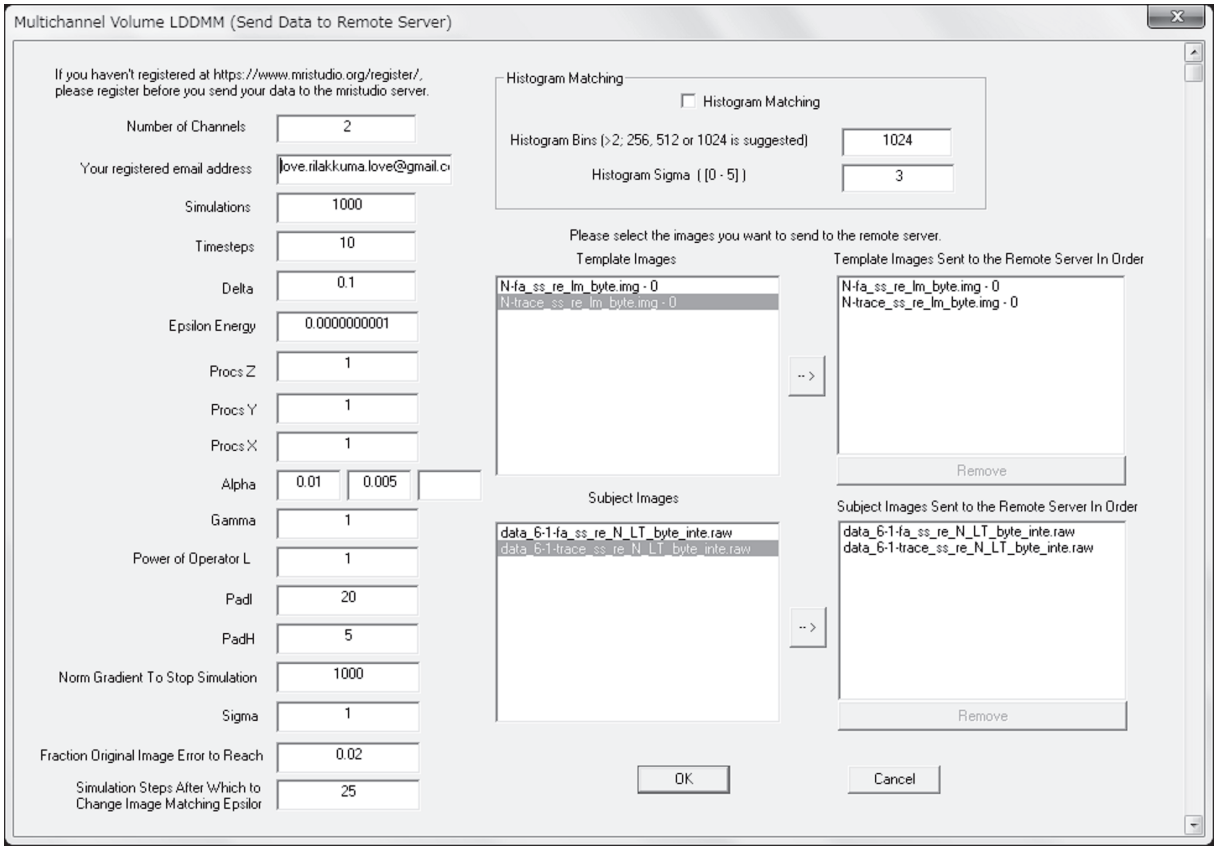

Figure A.15: The trace image of a single subject before (the upper row) and after (the lower row) the matching of histogram corresponding to the trace image of the standard brain.

Processing' to the registered e-mail address.

After the calculation for the nonlinearly transforming matrix is completed, we download the data set of the matrix from a URL linked to the output data on the received e-mail entitled 'Multichannel Process Complete'. The downloaded data set has 16 files, including 'Kimap.vtk' and 'Hmap.vtk'. Kimap is the transformation matrix to convert the subject's image corresponding to the template image. We apply Kimap to all linearly normalized images of the subject, and they are transformed nonlinearly for normalization corresponding to the standard brain. In contrast, Hmap is created for the transformation of the template image matching to the subject's image; i.e., Hmap indicates the inverse matrix of Kimap. The image classified the brain into parcels is prepared in MRI studio corresponding to the position of anatomical structures of the standard brain, which is the template image in this study. We call this image the parcellation map. Applying Hmap to the parcellation map for the standard brain, we can create the parcellation map corresponding to the anatomical structures of each subject, and analyze each segmented area in the original image of each subject. In this dissertation, we transform the subject's

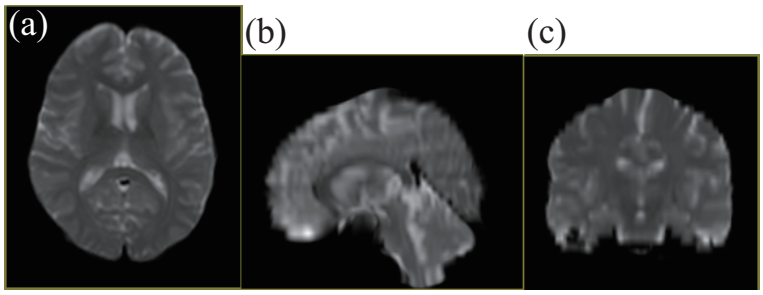

Figure A.16: The normalized $b0$ image linearly and nonlinearly corresponding to the image of the standard brain.

image with Kimap normalizing to the image for the standard brain.

The nonlinear transformation by Kimap is performed from 'Load Transformation Matrix' icon in 'Transformation' box in the subject' window after the $b0$ image of the standard brain is loaded in the template window, and the linearly transformed $b0$, FA, trace, and first eigenvector images are loaded in the subject's window in Diffeo Map. We transform images by 'LDDMM Matrix (VTK Format)' with the interpolation of 'Trilinear', selecting the 'Kimap.vtk' file. Then, all images of the subject are normalized using the nonlinear transformation matrix. We show the finally normalized $b0$ image in Figure A.16, which contains images in the same slices as images in Figure A.12.

In the actual performance of processing on and after the linear transformation in this study, we executed the processing with command-line prompt for the large portion of subjects, using some executable programs, which were divided into files for each function and provided by the developers of MRI Studio. Applying each function of the software on the command line, we can save time significantly.

References

[1] C.H. Judd. *Psychology General Introduction*. BiblioBazaar, 11 2009.

[2] S. Waxman. *Clinical Neuroanatomy*. McGraw-Hill Medical, 26th edition, 7 2009.

[3] C.M. Filley. *The Behavioral Neurology of White Matter*. Oxford University Press Inc., 2nd edition, 5 2012.

[4] V.K. Jirsa and A.R. Mcintosh. *Handbook of Brain Connectivity (Understanding Complex Systems)*. Springer, 1st edition, 7 2007.

[5] K.L. Davis, D.G. Stewart, J.I. Friedman, M. Buchsbaum, P.D. Harvey, P.R. Hof, J. Buxbaum, and V. Haroutunian. White matter changes in schizophrenia: Evidence for myelin-related dysfunction. *Archives of General Psychiatry*, 60(5):443–456, 2003.

[6] M. Hersen, S.M. Turner, and D.C. Beidel. *Adult Psychopathology and Diagnosis*. Wiley, Hoboken, 5th edition, 3 2007.

[7] P.V. Prasad. *Magnetic Resonance Imaging: Methods And Biologic Applications (Methods in Molecular Medicine)*. Humana Press, 11 2005.

[8] T. Moritani, S. Ekholm, and P.L. Westesson. *Diffusion-Weighted MR Imaging of the Brain*. Springer, 2nd edition, 6 2009.

[9] P.J. Basser, J. Mattiello, and D. LeBihan. MR diffusion tensor spectroscopy and imaging. *Biophysical Journal*, 66(1):259–267, 1994.

[10] M. Kubicki, R. McCarley, C.F. Westin, H.J. Park, S. Maier, R. Kikinis, F.A. Jolesz, and M.E. Shenton. A review of diffusion tensor imaging studies in schizophrenia. *Journal of Psychiatric Research*, 41(1-2):15–30, 2007.

[11] K. Oishi, A.V. Faria, P.C.M. van Zijl, and S. Mori. *MRI Atlas of Human White Matter*. Academic Press, London, 2nd edition, 11 2010.

[12] B. Kolb and I.Q. Whishaw. *Fundamentals of Human Neuropsychology*. Worth Publishers, New York, 6th edition, 2 2008.

[13] P.J. Basser and D.K. Jones. Diffusion-tensor MRI: theory, experimental design and data analysis - a technical review. *NMR in Biomedicine*, 15(7-8):456–467, 2002.

[14] S. Mori, B.J. Crain, V.P. Chacko, and P.C.M. Van Zijl. Three-dimensional tracking of axonal projections in the brain by magnetic resonance imaging. *Annals of Neurology*, 45(2):265–269, 1999.

[15] T.E. Conturo, N.F. Lori, T.S. Cull, E. Akbuda, A.Z. Snyder, J.S. Shimony, R.C. Mckinstry, H. Burton, and A.E. Raichle. Tracking neuronal fiber pathways in the living human brain. *Neurobiology*, 96:10422–10427, 1999.

[16] P.J. Basser, S. Pajevic, C. Pierpaoli, J. Duda, and A. Aldroubi. In vivo fiber tractography using DT-MRI data. *Magnetic Resonance in Medicine*, 44(4):625–632, 2000.

[17] S. Mori and P.C.M. van Zijl. Fiber tracking: principles and strategies - a technical review. *NMR in Biomedicine*, 15(7-8):468–480, 2002.

[18] M.S. Buchsbaum, C.Y. Tang, S. Peled, H. Gudbjartsson, D. Lu, E.A. Hazlett, J. Downhill, M. Haznedar, J.H. Fallon, and S.W. Atlas. MRI white matter diffusion anisotropy and PET metabolic rate in schizophrenia. *Neuroreport*, 9(3):425–430, 1998.

[19] K.O. Lim, M. Hedehus, M. Moseley, A. de Crespigny, E.V. Sullivan, and A. Pfefferbaum. Compromised white matter tract integrity in schizophrenia inferred from diffusion tensor imaging. *Archives of General Psychiatry*, 56(4):367–374, 1999.

[20] B.A. Ardekani, J. Nierenberg, M.J. Hoptman, D.C. Javitt, and K.O. Lim. MRI study of white matter diffusion anisotropy in schizophrenia. *Neuroreport*, 14(16):2025–2029, 2003.

[21] O.R. Phillips, K.H. Nuechterlein, K.A. Clark, L.S. Hamilton, R.F. Asarnow, N.S. Hageman, A.W. Toga, and K.L. Narr. Fiber tractography reveals disruption of temporal lobe white matter tracts in schizophrenia. *Schizophrenia Research*, 107(1):30–38, 2009.

[22] M.S. Buchsbaum, J. Friedman, B.R. Buchsbaum, K.W. Chu, E.A. Hazlett, R. Newmark, J.S. Schneiderman, Y. Torosjan, C. Tang, P.R. Hof, D. Stewart, K.L. Davis, and J. Gorman. Diffusion tensor imaging in schizophrenia. *Biological Psychiatry*, 60(11):1181–1187, 2006.

[23] H.J. Park, C.F. Westin, M. Kubicki, S.E. Maier, M. Niznikiewicz, A. Baer, M. Frumin, R. Kikinis, F.A. Jolesz, R.W. McCarley, and M.E. Shenton. White matter hemisphere asymmetries in healthy subjects and in schizophrenia: a diffusion tensor MRI study. *NeuroImage*, 23(1):213–223, 2004.

[24] J. Burns, D. Job, M.E. Bastin, H. Whalley, T. Macgillivray, E.C. Johnstone, and S.M. Lawrie. Structural disconnectivity in schizophrenia: a diffusion tensor magnetic resonance imaging study. *The British Journal of Psychiatry*, 182(5):439–443, 2003.

[25] M. Kubicki, C.F. Westin, P.G. Nestor, C.G. Wible, M. Frumin, S.E. Maier, R. Kikinis, F.A. Jolesz, R.W. McCarley, and M.E. Shenton. Cingulate fasciculus integrity

disruption in schizophrenia: a magnetic resonance diffusion tensor imaging study. *Biological Psychiatry*, 54(11):1171–1180, 2003.

[26] D.M. Carpenter, C.Y. Tang, J.I. Friedman, P.R. Hof, D.G. Stewart, M.S. Buchsbaum, P.D. Harvey, J.G. Gorman, and K.L. Davis. Temporal characteristics of tract-specific anisotropy abnormalities in schizophrenia. *Neuroreport*, 19(14):1369–1372, 9 2008.

[27] J.S. Oh, M. Kubicki, G. Rosenberger, S. Bouix, J.J. Levitt, R.W. McCarley, C.F. Westin, and M.E. Shenton. Thalamo-frontal white matter alterations in chronic schizophrenia. *Human Brain Mapping*, 30(11):3812–3825, 2009.

[28] K. Hua, J. Zhang, S. Wakana, H. Jiang, X. Li, D.S. Reich, P.A. Calabresi, J.J. Pekar, P.C.M. van Zijl, and S. Mori. Tract probability maps in stereotaxic spaces: Analyses of white matter anatomy and tract-specific quantification. *NeuroImage*, 39(1):336–347, 2008.

[29] L.R. Skelly, V. Calhoun, S.A. Meda, J. Kim, D.H. Mathalon, and G.D. Pearlson. Diffusion tensor imaging in schizophrenia: Relationship to symptoms. *Schizophrenia Research*, 98(1):157–162, 2008.

[30] L.M. Rowland, E.A. Spieker, A. Francis, P.B. Barker, W.T. Carpenter, and R.W. Buchanan. White matter alterations in deficit schizophrenia. *Neuropsychopharmacology*, 34:1514–1522, 2009.

[31] C. Knchel, V. Oertel-Knchel, R. Schnmeyer, A. Rotarska-Jagiela, V. van de Ven, D. Prvulovic, C. Haenschel, P. Uhlhaas, J. Pantel, H. Hampel, and D.E. Linden. Interhemispheric hypoconnectivity in schizophrenia: Fiber integrity and volume differences of the corpus callosum in patients and unaffected relatives. *NeuroImage*, 59(2):926–934, 2012.

[32] E.R. Kandel, J.H. Schwartz, and T.M. Jessell. *Principles of Neural Science*. McGraw-Hill, New York, 4th edition, 2000.

[33] M.R. Wiegell, H.B. Larsson, and V.J. Wedeen. Fiber crossing in human brain depicted with diffusion tensor MR imaging. *Radiology*, 217(3):897–903, 2000.

[34] A.L. Alexander, K.M. Hasan, M. Lazar, J.S. Tsuruda, and D.L. Parker. Analysis of partial volume effects in diffusion-tensor MRI. *Magnetic Resonance in Medicine*, 45(5):770–780, 2001.

[35] Y. Masutani, S. Aoki, O. Abe, and K. Ohtomo. A new fiber tracking method based on vector field reconstruction excepting fiber crossing area in MR diffusion tensor images (in Japanese). *Medical Imaging Technology*, 22(5):243–249, 2004.

[36] S. Peled, O. Friman, F. Jolesz, and C.F. Westin. Geometrically constrained two-tensor model for crossing tracts in DWI. *Magnetic Resonance Imaging*, 24(9):1263–1270, 2006.

[37] T. Oida, N. Imae, J. Jung, and T. Kobayashi. MR diffusion tensor tractography by searching similarity of direction vectors in the vicinity of fiber crossing areas (in Japanese). *IEICE Transactions on Information and Systems*, J91(7):1886–1894, 2008.

[38] F. Dell'Acqua, G. Rizzo, P. Scifo, R.A. Clarke, G. Scotti, and F. Fazio. A model-based deconvolution approach to solve fiber crossing in diffusion-weighted MR imaging. *IEEE Transactions on Biomedical Engineering*, 54(3):462–472, march 2007.

[39] B.W. Kreher, I. Mader, and V.G. Kiselev. Gibbs tracking: A novel approach for the reconstruction of neuronal pathways. *Magnetic Resonance in Medicine*, 60(4):953–963, 2008.

[40] R.H. Hashemi, W.G. Bradley, and C.J. Lisanti. *MRI: The Basics*. Lippincott Williams & Wilkins, Philadelphia, 3rd edition, 2010.

[41] D.G. Mitchell. *MRI Principles*. Saunders, 1 1999.

[42] E.L. Hahn. Spin echoes. *Physical Review*, 80:580–594, 11 1950.

[43] G.D. Fullerton. Magnetic resonance imaging signal concepts. *Radiographics*, 7(3):579–596, 1987.

[44] R.L. Dixon and K.E. Ekstrand. The physics of proton NMR. *Medical Physics*, 9(6):807–818, 1982.

[45] H.Y. Carr and E.M. Purcell. Effects of diffusion on free precession in nuclear magnetic resonance experiments. *Physical Review*, 94:630–638, 5 1954.

[46] S. Mori. *Introduction to Diffusion Tensor Imaging*. Elsevier Science, Kidlington, 1st edition, 5 2007.

[47] T. Araki. *Kakusan MRI - buraun undou, kakusan tensoru kara q kuukan he - (in Japanese)*. Shujunsha, Tokyo, 9 2006.

[48] T. Imae, M. Sekino, and H. Shinohara. *Kakusan MRI no kiso to ouyou (in Japanese)*. Iryou kagaku sya, 3 2011.

[49] M. Lazar, D.M. Weinstein, J.S. Tsuruda, K.M. Hasan, K. Arfanakis, M.E. Meyerand, B. Badie, H.A. Rowley, V. Haughton, A. Field, and A.L. Alexander. White matter tractography using diffusion tensor deflection. *Human Brain Mapping*, 18(4):306–321, 2003.

[50] E.W. Hsu, A.L. Muzikant, S.A. Matulevicius, R.C. Penland, and C.S. Henriquez. Magnetic resonance myocardial fiber-orientation mapping with direct histological correlation. *American Journal of Physiology - Heart and Circulatory Physiology*, 274(5):1627–1634, 1998.

[51] D.F. Scollan, A. Holmes, R. Winslow, and J. Forder. Histological validation of myocardial microstructure obtained from diffusion tensor magnetic resonance imaging. *American Journal of Physiology - Heart and Circulatory Physiology*, 275(6):2308–2318, 1998.

[52] C.F. Westin, S.E. Maier, B. Khidhir, P. Everett, F.A. Jolesz, and R. Kikinis. Image processing for diffusion tensor magnetic resonance imaging. In Chris Taylor and Alain Colchester, editors, *Medical Image Computing and Computer-Assisted Intervention*, volume 1679 of *Lecture Notes in Computer Science*, pages 441–452. Springer Berlin Heidelberg, 1999.

[53] D.M. Weinstein, G.L. Kindlmann, and E.C. Lundberg. Tensorlines: Advection-diffusion based propagation through diffusion tensor fields. In *Proceedings of the 10th IEEE Visualization 1999 Conference (VIS '99)*, VISUALIZATION '99, pages –, Washington, DC, USA, 1999. IEEE Computer Society.

[54] R. Xue, P.C.M. van Zijl, B.J. Crain, M. Solaiyappan, and S. Mori. In vivo three-dimensional reconstruction of rat brain axonal projections by diffusion tensor imaging. *Magnetic Resonance in Medicine*, 42(6):1123–1127, 1999.

[55] P.J. Basser and B.J. Roth. Stimulation of a myelinated nerve axon by electromagnetic induction. *Medical and Biological Engineering and Computing*, 29:261–268, 1991.

[56] P.J. Basser. New histological and physiological stains derived from diffusion-tensor MR images. *Annals of the New York Academy of Sciences*, 820(1):123–138, 1997.

[57] W.H. Press, B.P. Flannery, S.A. Teukolsky, and W.T. Vetterling. *Numerical Recipes in C: The Art of Scientific Computing*. Cambridge University Press, Cambridge, 2nd edition, 10 1992. pp.710–714.

[58] U. Yamamoto, T. Kobayashi, S. Kito, and Y. Koga. Analyses of disruption of cerebral white matter integrity in schizophrenia with MR diffusion tensor fiber tracking method (in Japanese). *IEEJ Transactions on Electronics, Information and Systems*, 130(5):799–806, 5 2010.

[59] N. Makris, D.N. Kennedy, S. McInerney, A.G. Sorensen, R. Wang, V.S. Caviness, and D.N. Pandya. Segmentation of subcomponents within the superior longitudinal fascicle in humans: A quantitative, in vivo, DT-MRI study. *Cerebral Cortex*, 15(6):854–869, 6 2005.

[60] K. Ichihara. *Bioscience no toukeigaku - tadashiku katuyou surutameno jissenriron (in Japanese)*. nankodo, 3 1990.

[61] H. Jiang, P.C.M. van Zijl, J. Kim, G.D. Pearlson, and S. Mori. DtiStudio: Resource program for diffusion tensor computation and fiber bundle tracking. *Computer Methods and Programs in Biomedicine*, 81(2):106–116, 2006.

[62] A.V. Faria, J. Zhang, K. Oishi, X. Li, H. Jiang, K. Akhter, L. Hermoye, S.K. Lee, A. Hoon, E. Stashinko, M.I. Miller, P.C.M. van Zijl, and S. Mori. Atlas-based analysis of neurodevelopment from infancy to adulthood using diffusion tensor imaging and applications for automated abnormality detection. *NeuroImage*, 52(2):415–428, 2010.

[63] Y. Cao, M.I. Miller, R.L. Winslow, and L. Younes. Large deformation diffeomorphic metric mapping of vector fields. *IEEE Transactions on Medical Imaging*, 24(9):1216–1230, 2005.

[64] K. Oishi, A.V. Faria, H. Jiang, X. Li, K. Akhter, J. Zhang, J.T. Hsu, M.I. Miller, P.C.M. van Zijl, M. Albert, C.G. Lyketsos, R. Woods, A.W. Toga, G.B. Pike, P. Rosa-Neto, A. Evans, J. Mazziotta, and S. Mori. Atlas-based whole brain white matter analysis using large deformation diffeomorphic metric mapping: Application to normal elderly and alzheimerfs disease participants. *NeuroImage*, 46(2):486–499, 6 2009.

[65] A.V. Faria, A. Hoon, E. Stashinko, X. Li, H. Jiang, A. Mashayekh, K. Akhter, J. Hsu, K. Oishi, J. Zhang, M.I. Miller, P.C.M. van Zijl, and S. Mori. Quantitative analysis of brain pathology based on MRI and brain atlases - applications for cerebral palsy. *NeuroImage*, 54(3):1854–1861, 2 2011.

[66] S. Kito, J. Jung, T. Kobayashi, and Y. Koga. Fiber tracking of white matter integrity connecting the mediodorsal nucleus of the thalamus and the prefrontal cortex in schizophrenia: A diffusion tensor imaging study. *European Psychiatry*, 24(5):269–274, 2009.

[67] M. Spiegel and S. Lipschutz. *Schaum's Outline of Vector Analysis (Schaum's Outline Series)*. McGraw-Hill, 2nd edition, 4 2009.

[68] U. Yamamoto, Y. Sakagami, T. Oida, and T. Kobayashi. A curvature deviation minimization searching method for MR diffusion tensor tractography (in Japanese). *Seitaiikougaku*, 49(1):139–147, 2 2011.

[69] U. Yamamoto, Y. Sakagami, T. Oida, and T. Kobayashi. Magnetic resonance diffusion tensor tractography by searching for minimum curvature deviation near fiber crossing area. *Proceedings of the 2012 ICME*, 1:588–592, 7 2012.

Publication List

Full papers

1. Utako Yamamoto, Tetsuo Kobayashi, Shinsuke Kito and Yoshihiko Koga, Analyses of Disruption of Cerebral White Matter Integrity in Schizophrenia with MR Diffusion Tensor Fiber Tracking Method (in Japanese). *The Institute of Electrical Engineers of Japan Transactions on Electronics, Information and Systems*, 130(5):799–806, 2010

2. Utako Yamamoto, Yoshihide Sakagami, Takenori Oida and Tetsuo Kobayashi, A Curvature Deviation Minimization Searching Method for MR Diffusion Tensor Tractography (in Japanese). *Transactions of Japanese Society for Medical and Biological Engineering*, 49(1):139–147, 2011

3. Utako Yamamoto, Akifumi Hisada, Tetsuo Kobayashi, Shinsuke Kito and Yoshihiko Koga, Analyses of the Disruption of White Matter Integrity in Schizophrenia using Diffusion Tensor Fiber Tracking with Automatic Construction of Region of Interest. *Advanced Biomedical Engineering*, accepted for publication in January, 2013

Proceedings (International conference)

1. Utako Yamamoto, Tetsuo Kobayashi, Shinsuke Kito and Yoshihiko Koga, An MR Diffusion Tensor Imaging Study on the Disruption of Cerebral White Matter Integrity in Schizophrenia: Fiber Tracking of the Superior Longitudinal Fasciculus. *Proceedings of 18th International Congress on Brain Electromagnetic Topography*, 219–222, 2009

2. Utako Yamamoto, Yoshiaki Kono, Tetsuo Kobayashi, Shinsuke Kito and Yoshihiko Koga, Study on the Disruption of Cerebral White Matter Integrity in Schizophrenia with MR-DTI Tractography. *Proceedings of 5th European Conference of the International Federation for Medical and Biological Engineering*, 37:618–621, 2012

3. Utako Yamamoto, Yoshihide Sakagami, Takenori Oida and Tetsuo Kobayashi, Magnetic Resonance Diffusion Tensor Tractography by Searching for Minimum Curvature Deviation near Fiber Crossing Area. *Proceedings of the 2012 International Conference on Complex Medical Engineering*, CFP12CME-CDR:588–592, 2012

Proceedings (Domestic conference)

1. Utako Yamamoto, Tetsuo Kobayashi, Shinsuke Kito and Yoshihiko Koga, On Disruption of Cerebral White Matter Integrity in Schizophrenia with MR Diffusion Tensor Imaging: Fiber Tracking of the Superior Longitudinal Fasciculus (in Japanese). *The Technical Report of The Proceeding of The Institute of Electronics, Information and Communication Engineers*, 109:57–62, 2009

2. Utako Yamamoto, Akifumi Hisada and Tetsuo Kobayashi, A Novel Fiber Tracking Method with MR-DTI Based on Curvature and Torsion for Crossing Area of Multiple Nerve Bundles (in Japanese). *The Technical Report of The Proceeding of The Institute of Electronics, Information and Communication Engineers*, in press, 2013

Awards

1. IFMBE Young Investigator Award, Study on the Disruption of Cerebral White Matter Integrity in Schizophrenia with MR-DTI Tractography, 5th European Conference of the International Federation for Medical and Biological Engineering, September 18, 2011